12-2013

OFFSHORE WIND ENERGY STUDY AND ITS IMPACT ON SOUTH CAROLINA TRANSMISSION SYSTEM

Tingting Wang
Clemson University, twang@g.clemson.edu

Recommended Citation

Wang, Tingting, "OFFSHORE WIND ENERGY STUDY AND ITS IMPACT ON SOUTH CAROLINA TRANSMISSION SYSTEM" (2013). *All Dissertations*. 1216.
https://tigerprints.clemson.edu/all_dissertations/1216

OFFSHORE WIND ENERGY STUDY AND ITS IMPACT ON SOUTH CAROLINA TRANSMISSION SYSTEM

A Dissertation
Presented to
the Graduate School of
Clemson University

In Partial Fulfillment
of the Requirements for the Degree
Doctor of Philosophy
Electrical Engineering

---

by
Tingting Wang
December 2013

Accepted by:
Dr. Elham B. Makram, Committee Chair
Dr. Ian Walker
Dr. Hyesuk Lee
Dr. Keith Corzine

ABSTRACT

As one of the renewable resources, wind energy is developing dramatically in last ten years. Offshore wind energy, with more stable speed and less environmental impact than onshore wind, will be the direction of large scale wind industry. Large scale wind farm penetration affects power system operation, planning and control. Studies concerning type III turbine based wind farm integration problems such as wind intermittency, harmonics, low voltage ride through capability have made great progress. However, there are few investigations concerning switching transient impacts of large scale type III turbine based offshore wind farm in transmission systems. This topic will gain more attention as type III wind generator based offshore wind farm capacity is increasing, and most of these large scale offshore wind farms are injected into transmission system. As expected to take one third of the whole wind energy by 2030, the large offshore wind energy need to be thoroughly studied before its integration particularly the switching transient impacts of offshore wind farms.

In this dissertation, steady state impact of large scale offshore wind farms on South Carolina transmission system is studied using PSSE software for the first time. At the same time, the offshore wind farm configuration is designed; SC transmission system thermal and voltage limitation are studied with different amount of wind energy injection. The best recommendation is given for the location of wind power injection buses.

Switching transient also impacts is also studied in using actual South Carolina transmission system. The equivalent wind farm model for switching transient is developed in PSCAD software and different level of wind farm penetration evaluates the transient performance of the system.

A new mathematical method is developed to determine switching transient impact of offshore wind farm into system with less calculation time. This method is based on the frequency domain impedance model. Both machine part and control part are included in this model which makes this representation unique. The new method is compared with a well-established PSCAD method for steady state and transient responses. With this method, the DFIG impact on system transients can be studied without using time-domain simulations, which gives a better understanding of the transient behaviors and parameters involved in them.

Additionally, for large scale offshore wind energy, a critical problem is how to transmit large offshore wind energy from the ocean efficiently and ecumenically. The evaluation of different offshore wind farm transmission system such as HVAC and HVDC is investigated in the last chapter.

DEDICATION

This dissertation is dedicated to my parents, *Ouguang Wang* & *Qizhen Luo*, and my fiancé *Xufeng Xu*.

ACKNOWLEDGMENTS

I would like to express my sincerest gratitude to my advisor and mentor Dr. Elham B. Makram not only for her guidance, caring, encouragement and patience throughout my research, but also always willing to help and give her best suggestions for my life.

I would like to thank Dr. Adly. A. Girgis, who is an example of industrious, righteous, conscientious professor. Without Dr.Makram and him, I would have no chance to continue my study in the United State. Dr.Markam and Dr. Girgis are like my family in Clemson.

I would like to thank Dr. Ian D. Walker, Dr. Hyesuk Lee and Dr.Keith Corzine for help about my research and being my committee members.

I would like to thank Dr. Ramtin Hadidi for his guidance and help about my research. I would like to thank Laura B Kratochvill for her help to review my dissertation, and Drenda Whittiker Stutts for her help and friendship.

I would like to thank all my colleagues in the power group for their friendship.

I would like to thank my fiancé Xufeng Xu, without whom this cannot be possible.

Finally I would like to thank my parents for their patience and their emotional and financial support throughout my life.

TABLE OF CONTENTS

Page

CHAPTER

Table of Contents (Continued)

Page

Table of Contents (Continued)

Page

Table of Contents (Continued)

Page

LIST OF TABLES

Table Page

LIST OF FIGURES

Figure Page

List of Figures (Continued)

CHAPTER ONE

INTRODUCTION

1.1 Motivation

Large scale offshore wind farms affect the integrated system transient by changing the grid configuration. Wind farms based on Type III wind turbines have a large number of energy storage devices including induction generators, converters, and transformers as well as submarine cables. The integration of such complicated network into system motivates the analysis of the transient impact of the wind farm as switching operations, for example load switching, capacitor bank switching, and small fault, and frequently occur. The Transient over Voltage (TOV), inrush current, and high frequency transient components are used to determine the insulation and protection coordination [1]. Failure to provide accurate information for those settings in a power system can cause overheating or damage, protection malfunction or loss of system stability after a fault [2]. Thus, it is critical to analysis the impact of the offshore wind farm impact on system switching transient.

Due to the development of digital computers, system transient studies requiring a device detailed model are able to be conducted using an appropriate discrete time program. However, it is difficult to simulate wind farm integrated systems, given their number of electrical storage devices connected in complicated configuration Thus, such as study needs an appropriate equivalent model. This problem is addressed in Chapter 2 of this dissertation.

Additional issues from the perspective of a wind farm project protection engineer involve the accessibility of the system data and decisions concerning the TOV or high frequency impact can be decided for protection devices installed on the system side.

This dissertation focuses on answering those questions in relation to the impact of offshore wind farm penetration impact on transmission system, including steady state impact and switching transient impact.

1.2 Research Background

Before explaining the goals of this dissertation, the status of wind energy development and its future are discussed. The wind industry is currently experiencing record growth. Table 1.1 shows the offshore wind farm capacity installed in different countries in the world by the end of 2011. The worldwide wind energy installation capacity reaches 296.255 Giga Watt (GW) by the end of June 2013, adding 13.98GW in the first six month of that year [3]. In the second half of 2013, an additional 22GW is expected to be constructed. Offshore wind saw it best growth in 2013, adding 1.08GW accounting for 7.1GW of the world's total energy capacity. After the erection of the world's first offshore wind farm, the Vindeby Farm in Denmak with a capacity of 4.95MW installation capacity-built, other countries began developing similar structures [4]. Expanding since 2006, 4,600 Mega Watts (MW) of offshore wind farms were operating worldwide by mid-2012, the majority of the offshore wind farms online in Europe. Though a small amount compared with the onshore wind, offshore wind shows great promise, with projections suggesting it will be responsible for one third of the world's wind energy by 2030[3].

Table 1.1 Offshore wind capacity by Nation- December 2011

Nation	Consented (MW)	Construction (MW)	Operational (MW)	Total (MW)
United Kingdom	1,257	2,239	1,341	4,837
Denmark	436	0	856	1,292
Belgium	529	148	195	872
Netherlands	3,037	0	228	3,265
Sweden	1,531	0	161	1,692
Germany	7,909	600	121	8,630
Finland	768	0	30	798
Ireland	1,100	0	25	1,125
Norway	407	0	2	409
Estonia	700	0	0	700
France	108	0	0	108
Total	17,782	2,987	2,959	23,728

Data from 4COffshore, industry press

The offshore wind industry in the US has not seen the dramatic growth as the rest of the world has [5]. The projects in the United States under development are mainly in the North Atlantic Ocean and on the Great Lake [6]. Even though the National Renewable Energy Laboratory (NREL) estimates that U.S. offshore winds have a gross potential generating capacity four times greater than the nation's present electric capacity, at present there is no operating offshore wind farm in the United States[7]. The obstacles for offshore wind development are not only geographical and technological but also financial, regulatory and supplying chain as well. The most advanced proposed offshore wind projects in the US are listed in the Table 1.2.

Table 1.2 Offshore wind farm projects in the United States

Offshore Wind Farm	Location	Nameplate Capacity
Cape Wind	Massachusetts	468MW
Coastal Point Energy Galveston	Texas	150MW
Blue water Wind	Delaware	450MW
Deepwater Wind	Rhode Island	415MW
Garden State Offshore Energy	New Jersey	350MW

Before integration, the generated wind power or voltage has to meet requirements such as power reliability standards, and flicker emission standards because of switching operations and voltage reduction during faults [4]. Since the regulations vary across countries, it is important to beware of the specific ones for the interconnected power system under consideration. Table 1.3 illustrates some wind farm integration regulations [4].

Table 1.3 Offshore wind farm integration regulations

Regulations
IEEE Standard 1001
MEASNET guide line
IEC 61400-21

1.3 Steady State Impact

South Carolina possesses potential offshore wind energy more than twice the amount of its consumption [8]. In 2009, Santee Cooper, a local South Carolina (SC) utility, proposed an offshore wind farm project along the SC coastal line to the

Department of Energy (DOE). This proposed project aims to exploit the green energy from the Atlantic Ocean along South Carolina the coastal line as shown in Figure 1.1. The two wind farms proposed are at North Myrtle Beach and Winyah Bay. The project is composed of three phases. For Phase I, 80 MW wind energy from state waters will be injected at two locations near the shore of South Carolina by 2013. For Phase II, an additional 1GW of wind energy from federal waters will be injected by 2020, while Phase III proposed to add another 2 GW of wind energy is to be added to the system by 2030.

The Clemson University Electric Power Research Associate (CUEPRA) has been funded to investigate the steady state impact of different amounts offshore wind energy on the SC transmission system [9], the issue addressed in Chapter 2 of this dissertation. The steady state technical report completed in 2011 by CUEPRA included three sections, each focusing on a different amount of wind injection. Results from this study are the initial points for further investigating the switching transient impact of SC offshore wind farms.

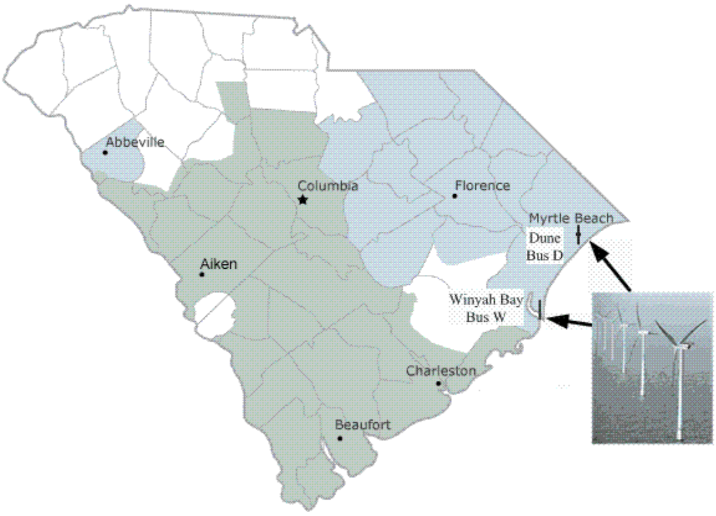

Figure 1.1 Map of South Carolina with wind penetration

1.4 Switching Transient Modeling and Solver

The power system is a complicated dynamic one, interconnected through numerous coupled energy storage components; it has to secure the qualified economic electrical energy to be delivered from the generator side to the load side at all the time. At the same time it has to sustain synchronization under persistent random disturbances [10][11].

When the system is subjected to a disturbance such as a fault, excessive currents or voltage variations result. The period time after the power system experiences a disturbance is defined as a transient [2][12]. If it is a small disturbance, such as load shedding or restoring, the system can adjust itself, while large disturbances such as a short-circuit on a transmission line, loss of a large generator or load, or loss of a tie between two subsystems, cause system responses such as a new state of operating equilibrium or a large excursion of generator rotor angle which might degrade the synchronization [13][14]. The ability of a power system to remain in operating equilibrium or regain a stable equilibrium is defined as power system stability. The loss of system stability can cause significant economic loss or some other disaster in a few seconds [15]. The prediction of such issues, which is the main objective of any power system transient study, is essential in the design of power systems, specifically for deriving the component ratings and optimizing controller and protection settings.

An effective way to analyze system transient is to categorize various models by their corresponding time scales. In light of the transient period involved, the power system study can be categorized as electromagnetic transient or electromechanical transient. Electromechanical transients refer to interactions between the electrical energy stored in the system, while electromagnetic transient is defined by the interaction between the electrical field of capacitance and the magnetic field of inductances in the power system. As shown in the Figure 1.2, transient process usually lasts within one second and can be categorized

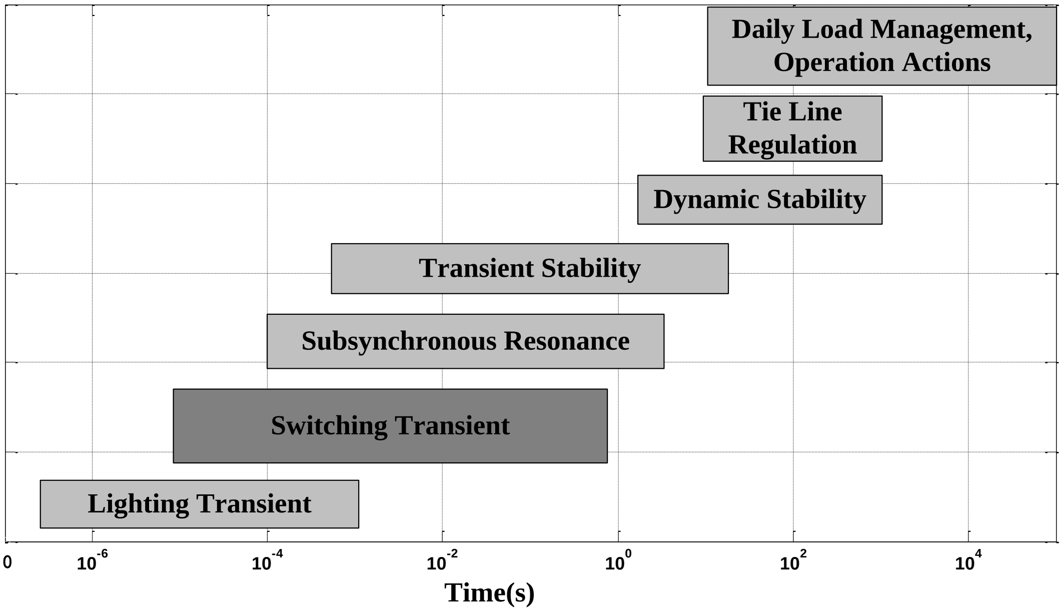

Figure 1.2 Power system study time frame

Switching transient is usually caused by the operations in a power system such as capacitor bank switching, load switching, or different types of fault or its clearance [2].Also, energizing various devices in a power system such as transformer energizing or cable energizing are very common triggers for this type of transients. The concerns resulting from a switching transient include high magnitude transient voltage or inrush current with frequency components arranging from the fundamental frequency up to 20 kHz [2]. These can cause stress on system insulation, affect protection settings in relays, influence the power quality, the damage equipment in the system or violate stability in the worst case.

An electromagnetic transient study is critical for in a power system in the area of insulation coordination, overvoltage studies caused by very fast transients, surge arrestor ratings, sub-synchronous resonance and Ferro resonance, relay coordination, transformer saturation effects studies, electrical filter design, control system design etc.

The research reported in this dissertation focuses on switching transient analysis, part of which is the electromagnetic transient study; the time length of a switching transient ranges from 1 ms to less than 1 sec [2]. However, transient stability is not included in this research.

The modeling of the system must be appropriate for the scope of the study. It is critical to categorize the phenomena by the time scale under consideration [2]. For example, steady state power flow problems can be formulated as a set of nonlinear algebraic equations based on current and voltage phasor in a frequency domain. The solutions usually include Gauss-Seidel iterations, the Newton Raphson method, and a decoupled power flow.

A switching transient study, due to power system's composition of hundreds and thousands of nonlinear devices such as generators and transformers, can be described by n^{th} first order linear differential equations [12]. The study of a power system transient primarily involves solving those equations in the frequency domain and time domain. The analysis of an electromagnetic transient solves a set of Kirchhoff's laws based on first order differential equations. There are different methods to solve differential equations.

There are several methods for solving differential equations. The Laplace transform system is suitable for a frequency-focused study, but the calculations dramatically increase as the system size changes. Transient network analysis (TNA) and the HVDC simulator use an analogue computer to simulate the transient. This dissertation focuses on the solution of electromagnetic transient problems in an offshore wind farm penetrated power system. In addition, in second part of this research, which focuses on the switching transient impact, uses PSCAD.

For the time domain algorithm the treat iterations is required, while numerical algorithm, such as the Runge-Kutta method, involve a numerical stability problem [16]. The development of the digital computer has led to more accurate and general solutions provided by computer-aided programs. Software like PSCAD/EMTDC or EMTP can provide the time domain solutions applicable for an electromagnetic transient study.

EMTDC (PSCAD) and other EMTP-type programs are based on the principles outlined in the classic 1969 paper by Hermann Dommel [17]. In this dissertation, the time domain simulation is implemented in PSCAD. EMTDC then converts the system into Norton equivalents, using numerical integration substitution to calculate transient phenomena [17][18].

1.5 Offshore Wind Farm Switching Transient

The switching operations related to an offshore wind farms integrated system could either be inside or outside the wind farm at the system side [19][20]. These operations include starting up wind generators, energizing the transformers or submarine cables and switching on or off the wind generators from the system. These operations impact the power delivery from the wind farms to the system and the power quality of the wind farm. Since the switching operations in a wind farm connected system may be caused by the system devices, switching operations such as capacitor bank switching may also influence the operation of the offshore wind farm.

Wind farm related research has focused on two primary areas, windmill modeling and wind farm integration impact research. Based on wind generator modeling, as it is known, today's wind generators can be classified into four types in today's market [4]. This research in this dissertation concentrates on the Type III, the Doubly Fed Induction Generator (DFIG). Based on past investigations, wind generators can be modeled as steady-state-oriented models [21], transient-stability-oriented models, or switching-transient-oriented models. The papers discussing wind turbines modeling include [18][22][23][24]. The type of wind turbine used in this research, the DFIG, has different types of control schemes such as direct torque control as discussed in [25], current control based on the reference quantities used [26] and the converter used[27][28]. As part of offshore wind farms, devices such as breakers and submarine cables are required to be modeled for specific research purpose. Papers discussing the modeling of those devices include [29], while those investigating the wind farms configuration [30]-[34] focus on the reliability [21] [35] and economic aspects of wind farm projects.

For research investigating the impact of the offshore wind farm impact on system side, the equivalent model has to be modeled; papers discussing aggregation modeling include [22][23][24][35][29]. For switching transient research, the paper [19][37][38] discuss the modeling methodology and validation as well as the simulation cases that have been most recently researched. However, since little detailed research on the impact of offshore wind farms on the system with switching operations has been conducted, this dissertation investigated the modeling and simulation results as well as the theoretical basis of this situation.

1.6 Frequency Domain Impedance Matrix

As seen in Fig.1.3 shows, the system transient bus voltage and bus injection current at the frequency domain are related by the frequency domain impedance matrix based on Equations (1-1). Self-impedance $Z_{ii}(s)$ is defined in (1-2) by the ratio between the voltage response at bus i and the injected current at bus *i*, while keeping the rest buses in the system open circuit. Mutual impedance $Z_{ij}(s)$ is defined in (1-3) by the ratio between the voltage response at bus *j* and the injected current at bus *i*, while keeping the rest buses in the system open circuit.

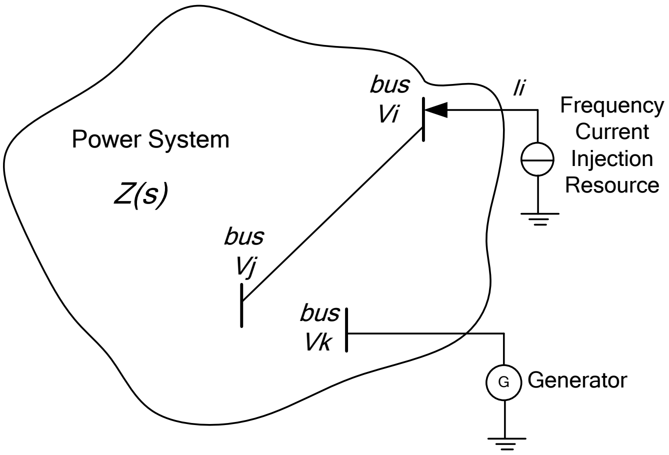

Figure 1.3 Power system impedance matrix

$$\begin{bmatrix} V_1(s) \\ V_2(s) \\ \dots \\ V_N(s) \end{bmatrix} = \begin{bmatrix} Z_{11}(s) & Z_{12}(s) & \dots & Z_{1N}(s) \\ Z_{21}(s) & Z_{22}(s) & \dots & Z_{2N}(s) \\ \dots & \dots & \dots & \dots \\ Z_{N1}(s) & Z_{N2}(s) & \dots & Z_{NN}(s) \end{bmatrix} \begin{bmatrix} I_1(s) \\ I_2(s) \\ \dots \\ I_N(s) \end{bmatrix} \quad \cdots\cdots\cdots\cdots\cdots\cdots (1\text{-}1)$$

$$Z_{ii}(s) = \left.\frac{V_i(s)}{I_i(s)}\right|_{I_j(s)=0} \quad \cdots\cdots (1\text{-}2)$$

$$Z_{ij}(s) = \left.\frac{V_j(s)}{I_i(s)}\right|_{I_j(s)=0} \quad \cdots\cdots (1\text{-}3)$$

$Z_{bus}(s)$ is suitable for fault analysis as the bus admittance matrix is for power flow calculation. Connecting a generator to the system can be indicated by adding a line between interface bus *k* and the reference through the generator transfer function. Since the system frequency impedance elementary can be derived using Equation (1-1), the fault current during transient can be calculated after the derivation of the DFIG frequency impedance model. This method is less time-consuming than the digital simulation for a large system whose detailed data are hard to obtain.

1.7 Offshore Wind farm HVAC and HVDC Transmission System

High Voltage Alternative Current (HVAC) and High Voltage Direct Current (HVDC) are two popular technologies for bulk energy transmission in a power system. By improving the transmission voltage leads to a corresponding decrease in the current, reducing the power loss as the square of the transmission current.

$$P_{loss} = I^2 R \quad \cdots\cdots (1\text{-}4)$$

Since the development of large power electronic devices such as Insulated-Gate Bipolar Transistor (IGBT) and thyristor, HVDC has received much attention for offshore wind farm transmission systems. For long-distance bulk energy transmission, HVDC is more economical because of the reduction in the transmission loss and the submarine cable cost [40][41][42][43][39]. Even though the price for the converter is higher than the substation used in an HVAC transmission system, an HVDC transmission system has more advantages. For example, it allows two interconnected systems to operate without synchronization, reducing the transient interaction between them, thereby improving the system transient stability significantly.

For offshore wind farms, HVAC is the standard for today’s windmill transmission systems. With more mature technology and simple connections, it is the first choice for most small size and middle size (less than 500MW) offshore wind farms in Europe. But due to its transmission distance limitation (the high voltage submarine cables), the HVDC transmission system is now receiving more attention in offshore wind farms. There is a much discussion about the HVDC transmission on the research level, most of it would be the directed toward large-scale, long-distance offshore wind farm transmission systems.

1.8 Research Objectives, Contributions and Structures

The research in this dissertation is aimed at investigating the penetration impact of OWFs on the South Carolina transmission system switching transient; its primary contributions and their corresponding chapters are listed below.

Chapter 2: This chapter discusses the offshore wind farms steady state impact on the South Carolina transmission system. As the basis for the research for remaining chapters, it investigated the performance of South Carolina’s power system performance after offshore wind energy is injected at different stages. In addition, wind farm configuration, the best locations for injecting the offshore wind farms in the system, and the system limitations for the wind energy penetration, as well as the solutions to faults resulting from this penetration are provided in this study, findings which are essential for determining the impact on the South Carolina power system.

Chapter 3 and Chapter 4: The impact of offshore wind farm switching impact on the South Carolina transmission system is investigated in these two chapters including system modeling and simulation case study. In these two chapters, the offshore wind farm equivalent system for switching transient study modeling is determined. Based on an equivalent wind farm model already established, the offshore wind farm such as energizing the cable and switching on/off the DFIGs are studied. And the South Carolina power system is studied before the wind farm model is connected. The wind farm impact of the system switching transient on the first South Carolina reduced system is not apparent due to the low penetration level of 3.87%. In order to better investigate the impact of the offshore wind farm switching transient, this research then creates island systems around the OWF’s connecting points to reduce the system size, subsequently analyzing such switching cases as load switching, capacitor bank switching, and three-phase faults based on the modeling.

Chapter 5: The impact of the offshore wind farm switching transient impact on system frequency domain analysis is studied in this chapter. In order to find a mathematical method for determine the switching transient impact of the offshore wind farm on the system, a frequency domain impedance matrix is developed and verified with other software models. The derivation details are presented in this chapter. The model simulation results are compared with the PSCAD time domain calculation results.

Chapter 6: An economic evaluation of the HVAC and HVDC offshore wind farms are discussed in this chapter. For large scale offshore wind energy, the critical problem is energy transmission. The HVDC transmission system is attaching attentions for use in offshore wind farm. In this chapter, the costs of the various components in the offshore wind farm are investigated. The losses for both HVAC and HVDC transmission system configurations are studied. Finally, the PSCAD steady state performance of the two systems is simulated.

CHAPTER TWO

OFFSHORE WIND FARMS STEADY STATE IMPACT ON SOUTH CAROLINA TRANSMISSION SYSTEM

In this chapter, the South Carolina power transmission system steady state behavior after the penetration of large scale offshore wind energy is studied. It is divided in three phases of incremental wind energy production.

2.1 Steady State Analysis Phase I

2.1.1 Description of Offshore Wind Project

South Carolina is supplied by three utilities: Santee Cooper, South Carolina Electrical & Gas (SCE&G) and Duke Power. 80 MW offshore wind energy is expected to be delivered in state water at the first stage [9]. This research is to design two offshore wind farms which are located in North Myrtle Beach and Winyah Bay, as shown in Figure 2.1. The transmission power system of Santee Cooper and SCEG are studied to analyze the wind energy penetration impact on the South Carolina power system.

Figure 2.1 Locations of wind farms in South Carolina

The strength of the grid at Point of Common Coupling (PCC) is critical for the penetration of wind farm [44]. This strength can be illustrated as the short-circuit power and grid impedance angle. On the other hand, connecting offshore wind farms to the grid on shore requires new transmission lines and submarine cables between offshore substation and onshore substations. Thus, it is more economical considering the distance of the substation to offshore the windmill. As seen in Figure 2.2 and Figure 2.3, there are five alternative PCCs at North Myrtle Beach and only one interface in the Winyah Bay area. Based on those PCC, selected considering the economic aspect, the different grid performance after offshore wind farm penetration is compared to determine the optimal interface buses. In Table 2.1 the available 115kV transmission buses along South Carolina coastal line are listed in the table.

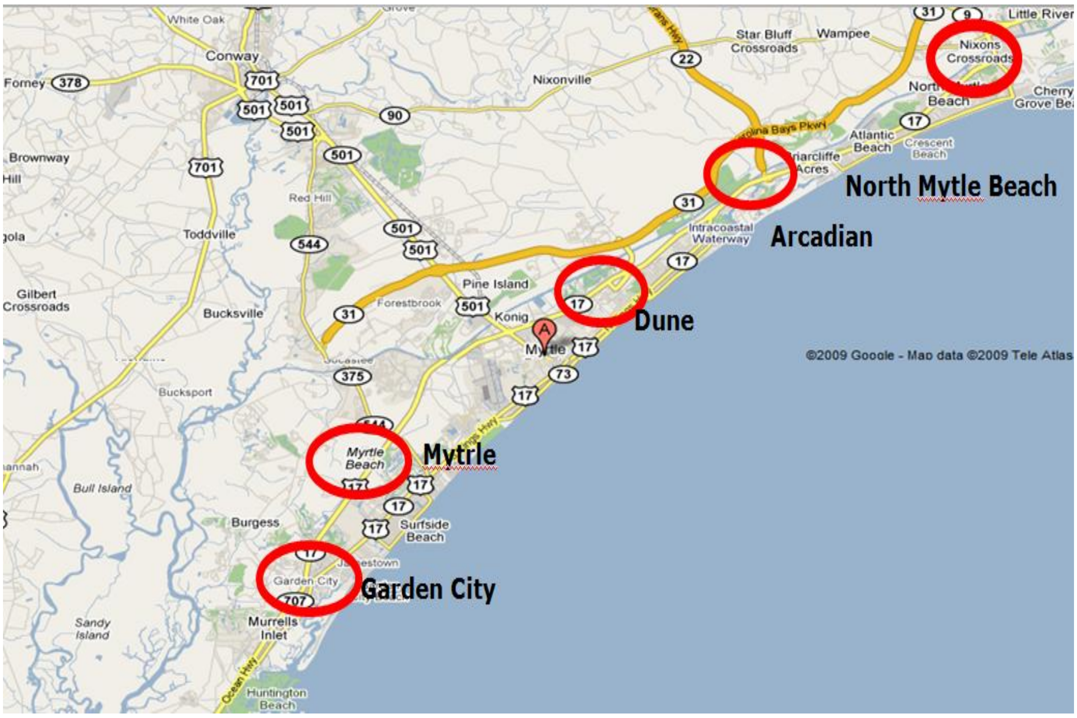

Figure 2.2 Possible locations of the North Myrtle Beach wind farm

Figure 2.3 Possible location of the wind farm in Winyah Bay

Table 2.1 List of coastal 115 kV buses

Bus No.	Bus Name	Bus location
312811	'3NIX XRD'	Nixons Crossroads
312764	'3DUNES'	Dunes
312807	'3MYRT BC'	Myrtle Beach
311322	'3ARCADI'	Arcadia
312766	'3GRDN C'	Garden City
312845	'3WINYAH'	Winyah 115 kV

2.1.2 Offshore Wind Farm Configuration

For the first stage 80MW, it is assumed that the wind energy generated by these two wind farms is evenly distributed from these two offshore wind farms which are expected to supply 40 MW power to the system.

In the research of this dissertation, GE 3.6 MW Doubly Fed Induction Generator (DFIG) is selected as the typical type III wind generator and its parameters are listed in the Appendix B. Each wind farm consists of 12 wind turbines which are parallel connected in a column as shown in Figure 2.4. DFIGs are connected to a common bus through their own step up transformer which increases wind generator output voltage to medium voltage. Before wind power can be delivered to the onshore transmission substation, it needs to be upgraded to high voltage by another step transformer (34.5/115KV). This big capacity transformer on the sea requires an offshore substation. The submarine power transmission cable has to be determined according to the expanse [45] [46][47]. Parameters of the selected transformers are listed in Appendix A.

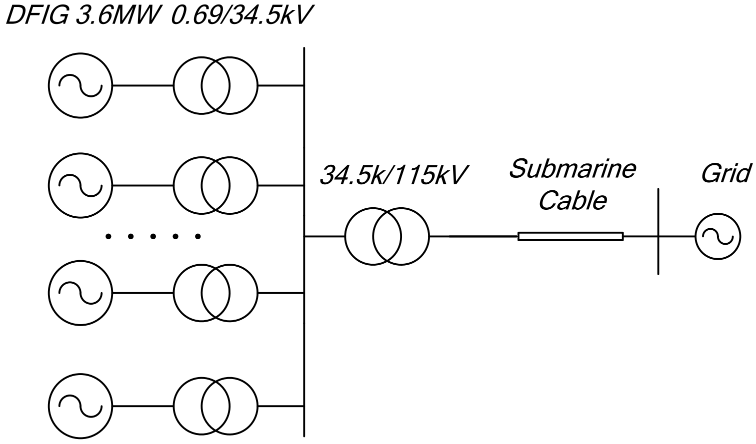

Figure 2.4 Wind farm connection for Phase I

2.1.3 Generation Reduction

One of challenges regarding the wind farm integration relates to the balancing between wind power and system generation. Any imbalance can cause mismatch in the system and influence the power system operation condition [48]. In order to match the offshore wind energy and the generation, the generation reduction priority rules are followed: (1) Reduce steam plants, coal plants before hydro plant; (2) Shut down or reduce generations by ascendant order of plant sizes.

At the wind farm side, the power peak, which is defined as the maximum active power output of the wind turbine over a specific time during continuous operation, is assumed for each wind farm in this part of research. The generation within Santee Cooper is orderly reduced, and the reduction list for this part of the research is Myrtle Beach and Hilton Head, second Rainey and finally the Grainger power station.

2.1.4 Wind Farm Integration Requirement

(1) For the system around PCC, the steady state voltage change caused by wind farm penetration is one of the limiting factors for grid connection.

(2) The SC grid regulation requires the voltage violation to be within ±5% of rated value for steady state at light load operation condition. On the local level, the connection of wind farm with type III wind generators which can control output voltage and the power factor with the inverter system, actually contributes to the voltage stability and violations.

(3) Additionally, the overloaded transmission lines should not exceed ±10% of their capacity at peak loading operation mode. The transformers of the SC grid are allowed to be overloaded ±10% over peak loading operation mode.

(4) The SC power system requirements such as voltage violation and the overloaded transmission lines and transformer will be verified with offshore wind farms connected.

2.1.5 The Simulation and Results Analysis

Based on the wind farm device parameters and configuration design, the offshore wind farm is modeled in PSSE. Five combinations for different interface buses at Myrtle Beach with the one at Winyah Bay to delivery 80MW offshore wind energy into SC power system are assembled. Power flows for the different system operation mode including heavy load condition (summer 2010, summer 2014, and summer 2019) with offshore wind farm are analyzed. Table 2.2 illustrate the list of possible interface buses for the wind farm per location.

Table 2.2 Case list used for each of the three base case power flow

Case list	Interface Bus#	
	North Myrtle Beach	Winyah Bay
Case 1	312811	312845
Case 2	312764	312845
Case 3	312807	312845
Case 4	311322	312845
Case 5	312766	312845

Based on the analysis of the results for all five cases, there’s no voltage violation and overloaded transmission lines or transformer caused by the injection of 80 MW of wind energy in SC power system. This means the SC grid is capable of reaching the first stage of this project. However, it can be seen that case 2 is recommended based on the voltage profile and the branch power flow. In Table 2.3, the recommended 115kV interface buses for South Carolina offshore wind projects are listed.

Table 2.3 Recommend 115 kV interface buses

Bus No.	Bus Name	Bus location
312764	'3DUNES'	Dunes
312845	'3WINYAH'	Winyah 115 kV

2.2 Steady State Analysis Phase II

Phase II extends 1 GW offshore wind farm from the state coastal line to the federal water, which has a promising and attractive potential for wind power generation. Figure 2.5 show that the federal water has a higher wind speed beyond the state water in the Southeast Pacific Ocean. The additional 1 GW of wind energy is injected into the Santee Cooper power system at the same two locations as in Phase I in North Myrtle Beach and Winyah Bay; i.e. with 500 MW at each location into 115 kV voltage transmission grids as shown in Figure 2.6.

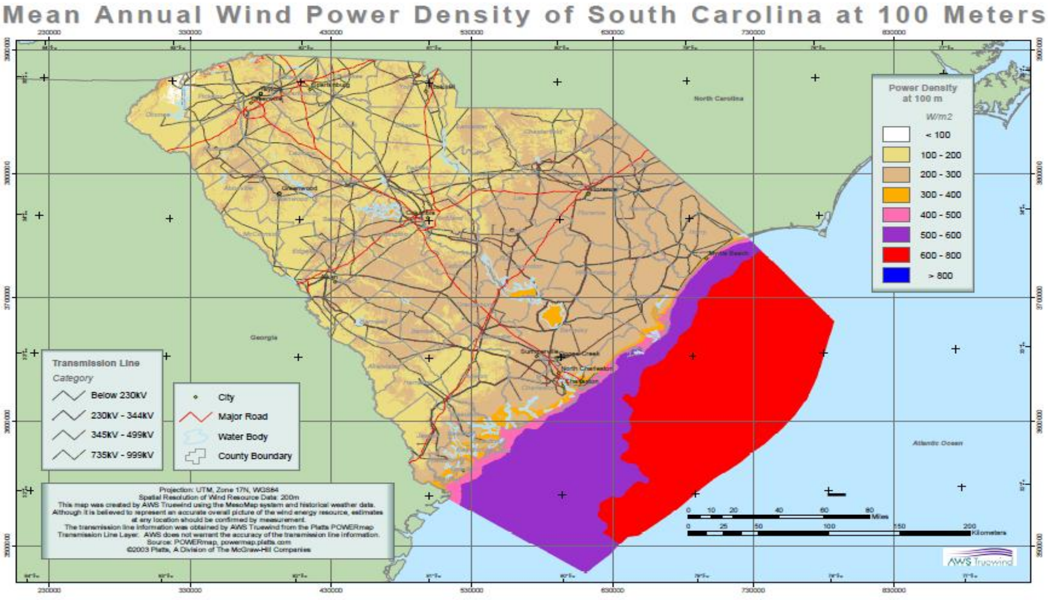

Figure 2.5 Wind power density of South Carolina

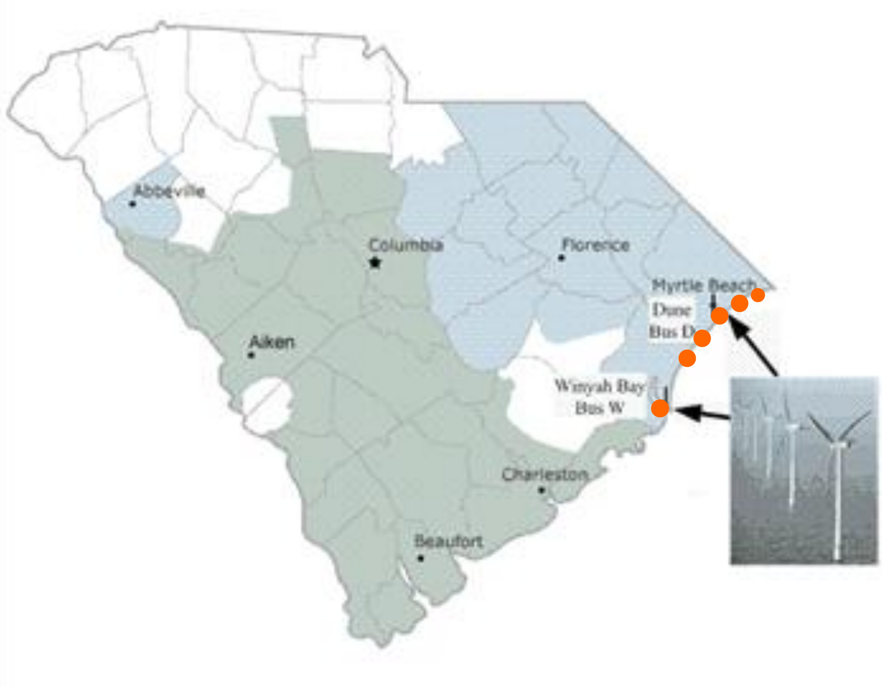

Figure 2.6 Illustrations of offshore wind farm locations

The offshore wind farm configuration for this stage is illustrated in Figure 2.7. The turbines are connected in parallel to the collector bus through a step up transformer to medium voltage. The collector bus is connected to the power system at the interface bus through offshore substation of voltage rating 34.5/115 KV. Similar to Phase I, the GE 3.6 MW wind turbine is used for the simulations. Table 4 in Appendix C presents the parameter for the wind farm transformer rated 34.5/115 KV, which has a higher rating than the one used in Phase I.

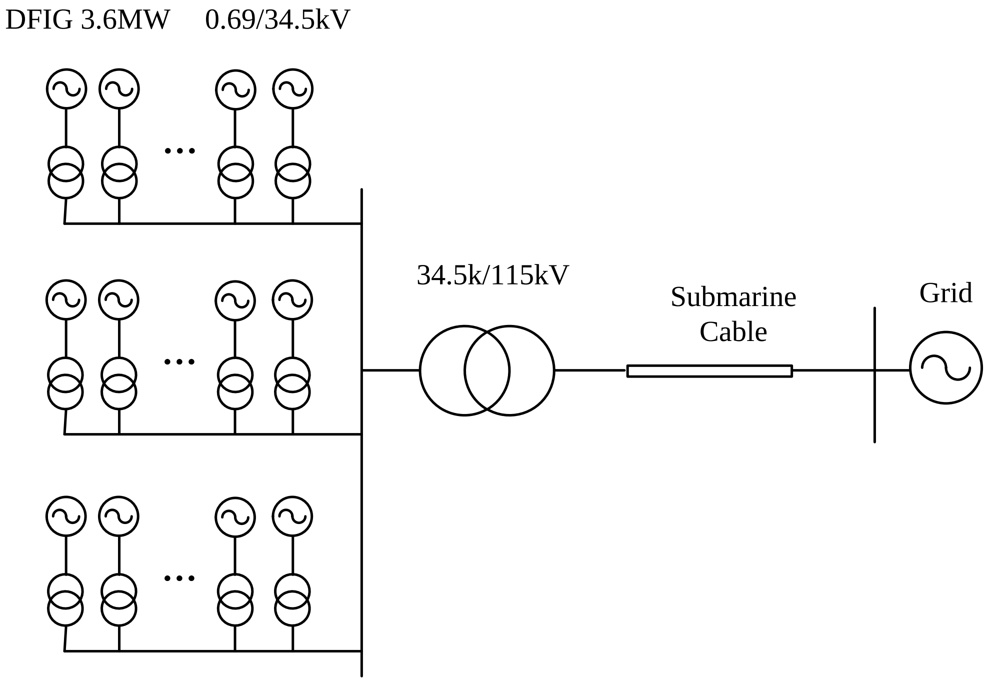

Figure 2.7 Wind farm connection diagram

In this scenario, wind energy is distributed within four electric utilities around the SC power system (Duke Power, Progress Energy, Santee Cooper and SCE&G) and is based on the load ratio of 2009 summer. The energy distribution is as follows: 46% for Duke, 30% for Progress Energy, 12% for Santee Cooper and 12% for SCE&G as shown in Table 2.4. In order to keep the power balance in system, the same amount of generation in the four utilities need to be reduced accordingly to their load ratios presented in Table 2.4. However, there is no specific guideline to reduce the generation in the four companies except Santee Cooper.

Table 2.4 Wind energy distribution ratio

Area Name	P Load (MW)	Load ratio	Load Ratio in (%)
SCEG	4673.967	0.1158	12%
Santee Cooper	4774.263	0.1183	12%
Progress	11961.915	0.2964	30%
DUKE	18948.089	0.4695	46%
Total	**40358.234**	**1**	**100%**

2.2.1 Analysis of Simulation Results

Different cases are studied with the consideration of voltage violation and transmission line loading conditions along with recommendations and supplementary suggestions made with the intention of diversifying the choices in this part. The power grid connection point has different characters [49].

(1) Even distribution of 1080 MW between the two wind farms for 115KV buses

In this scheme, 540 MW is supposed to be generated by each wind farm (North Myrtle Beach and Winyah Bay). In Case 3 the mitigation by adding a capacitor bank of 30 MVAR on bus 312779 or by increasing the existing capacitor bank on bus #312766 by about 50 MVAR (from 30 MVAR to about 80 MVAR) can be applied to alleviate the overloaded transmission lines after the wind farm integrated. Case 1, Case 2, Case 4 and Case 5 could not be solved under this condition.

(2) Uneven distribution of 1080 MW between the two wind farms for 115KV buses

In this scheme, the wind farm located at Winyah Bay has a higher wind power penetration capacity than the North Myrtle Beach location. By adjusting the amount of wind power penetrated at each location, Case 2 and Case 3 do not yield any overloaded transmission lines. The Table 2.5 illustrates the recommended cases ranked from the best based on the voltage violation and branch power flow.

Table 2.5 Recommended interface buses

Ranking (High to Low)	Recommended cases	Interface bus information			Injection amount		
						Phase II	
		Bus #	Bus Name	Bus location	Phase I	Even distribution	Uneven distribution
1	Case 3	312807	'3MYRT BC'	Garden City	40 MVA	500 MVA	449.6 MVA
		312845	'3WINYAH'	Winyah	40 MVA	500 MVA	550.4MVA
2	Case 2	312764	'3DUNES'	Dunes	40 MVA	N/A	460.4 MVA
		312845	'3WINYAH'	Winyah	40 MVA	N/A	539.6 MVA

2.2.2 Suggestion for Second Stage

The suggestion of the wind energy penetration for the second stage is made in this part based on the result analysis above. Even though the cost of these suggestions may be more than the simulation cases above, these schemes are alternatives and consider because of the system reliability.

(1) Using Three 115 KV Interface Buses

The first suggestion uses three 115 KV interface buses instead of two interface buses, which reduces maximum transmission line loading to 96%. There is no doubt that the related cost will increase dramatically. However, considering the reliability of the system when the wind farm is connected to it, this would be an alternative for the SC grid. In this scenario, 1080 MW wind farm penetrates into Santee Cooper electrical network at three different 115 KV interface buses. Two of the latter interface buses are located in North Myrtle beach and the last one in Winyah Bay. Table 2.6 show a case using three interface buses that has all branches loaded below 96% of their rating in the system.

Table 2.6 Suggested case using three 115kV interface buses

Interface Bus	Bus Location
312845	Winyah Bay
312764	Dunes
312807	Myrtle Beach

(2) Using Two 230 KV Interface Buses

The second suggestion uses two 230 kV interfaces buses to bring down the maximum branch loading to 97.7%. In this situation, the 1080 MW wind energy enters the Santee Cooper electrical system at two 230 kV interface buses which also aim to reduce transmission line maximum loading conditions. The result of the power flow using two 230 kV buses to inject the wind energy into the grid (the two interface buses are “312717” and “312719”) is presented in the South Carolina Offshore Wind farm impact report. Another advantage of using the 230 kV is that the 230 kV interface buses have a better capacity to absorb more resources and are less likely to have congested lines; thus less constraints on location of generation reduction within the four utilities. A total of 16 cases have been successfully tested without any overloaded lines. In other words, the energy injection at the 230 kV network can improve the power flow result significantly by reducing lines flow.

2.3 Steady State Analysis Phase III

For the Phase III third scenario, an additional 2 GW of wind farm is expected to be installed in federal water by the year 2030 after the second stage. The extra wind power is distributed between five electric utilities: Southern Company, Duke Power Energy, Progress Energy, Santee Cooper and SCE&G. This is based on the ratio of their loads based on the summer 2009 power flow. Accordingly, the wind energy distribution for Phase III (2.08GW) is the following as shown in Table 2.7: 22% for Duke, 14% for Progress Energy, 5% for Santee Cooper, 6% for SCE&G and 53% for Southern Company. After reducing the existing generations in the five utilities accordingly to their load ratios, both 115kV and 230kV transmission systems are considered to deliver this amount of wind energy.

Different cases are tested using either one voltage rating or a combination of both voltage ratings for wind energy transmission system. In case penetrating the whole 2 GW cannot meet the SC system requirement, the limitation of wind energy can be injected into the SC power system with or without considering the load distribution ratio. In addition, the recommendations for improving the transmission network are provide to deliver more offshore wind energy.

Table 2.7 Wind energy distribution ratio

Company	Percent of 3GW	The Wind power(MW)
SCE&G	6%	180
Santee Cooper	5%	150+80
PROGRESS	14%	420
DUKE	22%	660
SOUTHERN	53%	1590

2.3.1 Analysis of Simulation Results

The results of the voltage violations (V<0.94 p.u. or V>1.06 p.u.) and the transmission lines overloading are discussed below. The orange color represents the 115 kV buses zone and the green color the 230 kV. The simulation cases are divided where the distribution ratio is followed. The SC 115 kV transmission system is not able to consume the whole extra 2 GW wind. In order to identify the amount of the 115 kV system wind energy penetration capability, the incremental amount of wind power injection in the system is tested. It is found that the SC power system maximum wind energy penetration capacity is about 1191.6 MW for 2009 summer case, which is accomplished by 442.8 MW at Winyah and 748.8 MW at Dune. Table 2.8 shows the rest interface bus limitation.

Table 2.8 System injection limitation

Number of buses in a set	2 buses	3 buses	4 buses	5 buses
Injection capacity of the original system	1192 MW	1280 MW	1280 MW	1280 MW

Based on two 115 kV buses for Phase I and II (80 + 1000 MW), the third stage wind injection is using two 230 kV for Phase III (2 GW). For the 230 kV transmission systems, the results show it has a maximum penetration case with capacity of 2001.6 MW which is accomplished by 720 MW in Santee Cooper network at Perry R bus and 1281.6 MW at Winyah Bay bus. This case doesn't have any overloaded transmission lines for the whole 3080MW wind penetration. Table 2.9 shows the rest 230kV interface buses for offshore wind farm injection. However, the other injection cases require three new transmission lines (new line# 1, 2 and 3 of Table 18) for the system to handle the whole 3.08 GW without any overloaded branch.

Table 2.9 List of Santa Cooper's 230 kV coastal buses

Bus Name	Bus location
6WINYAH	Winyah
6MYRTLE	Myrtle Beach
6PERRY R	Georgetown
6CAMPFLD	Camp Field
6CHARITY	Georgetown
6REDBLUF	Myrtle Beach

The specific interface buses and the amount of energy consumed at each bus are listed on Table 2.10.

Table 2.10 Distribution of wind power between interface buses

Bus Name	Bus Location	Area	Wind Turbine	Wind Injection
6Perry R	Myrtle Beach	Santee Cooper	266	957.6MW
6Winyah	Winyah Bay	Santee Cooper	295	1062 MW
Dune	Myrtle Beach	Santee Cooper	121	435.6 MW
Winyah	Winyah Bay	Santee Cooper	151	534.6 MW
Dune	Myrtle Beach	Santee Cooper	12	43.2 MW
Winyah	Winyah Bay	Santee Cooper	11	39.6 MW
			Total	3080 MW

2.3.2 Suggestion for the Third Stage

(1) Wind Energy Distribution with Reduction Criteria not observed

The idea is not to follow the generation reduction based on the load ratio (the wind energy distribution criteria). The absorption capacity of the SC power system can be greatly improved if most of the generators reduction is done within the Santee Cooper network, specifically at the Winyah Bay generation. In other words, if a large portion of the wind energy can be consumed by Santee Cooper locally instead of changing the power flow of a remote area, it will improve the SC system steady stage performance with the wind farm connection. To successfully implement this idea, the generation at the power plants in Santee Cooper area should be reduced to their minimum value primarily. By not following the wind energy distribution criteria, about 2361.6 MW extra wind energy can enter the Santee Cooper network at two 230 kV without a branch overload which is accomplished by 720 MW at 6Perry and 1641.6 MW at Winyah Bay. With this concept, the power system can absorb the whole 3080 MW without any upgrade for the scenario that utilizes concurrently two 115 kV (1080 MW) and two 230 KV (2 GW) as interface buses. Table 2.11 shows the critical generators for solving congestion at Winyah Bay when wind energy penetration.

Table 2.11 Critical generators for congestion at Winyah Bay area

Bus name	P_g	$P_{\max}$	$P_{\min}$	Q_g	$Q_{\max}$	$Q_{\min}$	S_{base}	X
1WINY2 21.000	285	285	100	73.96	130	-175	350	0.21
1WINY3 21.000	285	285	100	73.96	130	-175	350	0.21
1WINY4 21.000	285	285	100	73.96	157	-184	350	0.2513
1PEEDEE 21.000	609	682	200	237.1	250	-155	750	0.18

(2) Adding New Transmission Lines (Distribution Criteria follows)

In case the distribution criteria according to load ratio is required among these five utilities, the improvement of the power system by adding new transmission lines is mandatory to accommodate the 3080 MW wind energy into the SC power system. Depending on the interface bus combinations, the number of the new transmission line required varies. The suggested new transmission lines are listed in Table 2.12. The study is done by voltage ratings: 115 kV, 230 kV, and a combination of both.

Table 2.12 Suggested new transmission lines

Line #	New transmission line information								
	From	To	Circuit#	$R_{p.u.}$	$X_{Lp.u.}$	$X_{c\,p.u.}$	Lim A MVA	Lim B MVA	Lim C MVA
1	311650	312729	2	0.00171	0.02274	0.08939	797	797	1100
2	304632	304654	2	0.03251	0.08671	0.0106	97	97	97
3	312845	312770	10	0.0035	0.0309	0.0043	239	275	275

For SC 115 kV transmission network, adding new transmission lines to the power system doesn’t improve its injection capability unless more than four interface buses are put into use. By doubling the capacity of the transmission line connecting 6Peedee to 6Marion (Line# 1 on Table 2.12), the injection limit of the system is increased to 2080 MW (see Table 2.13 below for more details).

Table 2.13 System injection limit using different set of 115 kV buses

System	3 interface buses	4 interface buses	5 interface buses
Original + 1 New Line	1280 MW	2080 MW	2080 MW

For 230 kV SC transmission system injection, the total amount of 3080 MW wind energy can enter the Santa Cooper grid at two 230 kV buses without any overloaded transmission line if the new line 1 and 2 of Table 2.12 are added to the network. Even though there are three transformers that are loaded at about 105% of their rating, this is an acceptable loading condition for transformer. However, this scheme generates under voltage violation at system buses, but it can be fixed by shunt capacitors. The results of the power system with adding new transmission lines and using two 230 kV buses interface buses in Santa Cooper is included in the SC wind farm report.

Table 2.14 Cases with new transmission lines

Case #	Bus voltage rating			
	115 KV bus Number		230 KV Bus Number	
1	312845	312807	312719	312717
2	312845	312807	312719	312726

2.3.3 Testing of 2009 Light Load Base Case

Since the only light load base case power flow available is for 2009, 3.08 GW of wind energy is injected into the power grid to check its penetration capability during off peak hours. However, the result of the simulation shows that the system can only take about 2150 MW without overloading any branch. The presence of wind energy in the power network improves tremendously over the overvoltage aspect of the 2009 light load case by reducing the number of bus overvoltage violations to the third of its original values. Table 2.15 displays the specific information related to the voltage violations in the original and the system with wind energy, which uses two 230 kV interface buses.

Table 2.15 Voltage violations at light load

System	# of buses with voltage below 0.94 p.u.	# of buses with voltage above 1.06 p.u.	# of buses with voltage above 1.08 p.u.	Lowest voltage (p.u.)	Highest voltage (p.u.)
Original system (2009 Light Load) only	11 buses	262 buses	18 buses	0.916086	1.15422
Original system with 2150 MW of wind energy	11 buses	76 buses	9 buses	0.916777	1.13879

The evaluation of the results shows that if the wind energy distribution criteria based on load ratios is followed, the power system cannot handle the whole 3.08 GW. At 115 kV voltage rating, the power grid has an injection limit of about 1190 MW and 2000 MW at 230 kV (using two buses at a time). To improve the injection capacity of the network to accommodate the 3.08 GW, two approaches are taken. The first one is not to follow the wind energy distribution criteria, i.e. a large amount of the energy are consumed by Santee Cooper’s load. However, this solution may not be feasible. A successful case to use two 115 kV buses and two 230 kV buses for interfacing the wind farms is presented in Table 2.16. The second method adds new lines to increase the transmission capability of the power system. There are two scenarios in which the power grid can successfully absorb the 3.08 GW with a minimum number of new lines. The first scenario, which requires 2 new lines (lines 1 and 2 on Table 2.16), uses two 230 kV buses as wind energy interface buses. The second scenario, which requires 3 new lines (all the new lines on Table 2.16), use two 115 kV and two 230 kV buses as interfaces. In conclusion, the study of the 2009 Light Load base case shows that the wind energy reduces the voltage violation.

Table 2.16 Recommended interface buses for injecting 3080 M

Interface bus voltage rating	Interface bus#	Bus Name	Original power system	Power system with improved Transmission capability	
				Scenario I	scenario II
115 kV	312764	Dune	435.6 + 43.2 MW	N/A	N/A
	312807	3MYRT BC	N/A	540 MW	N/A
	312845	Winyah	534.6 + 39.6 MW	540 MW	N/A
230 kV	312717	6Perry R	957.6 MW	N/A	N/A
	312719	6Winyah	1062 MW	1000 MW	1540 MW
	312726	6REDBLUF	N/A	1000 MW	1540 MW
New transmission lines	Line 1: 6PEEDEE to 6Mariom		N/A	Yes	Yes
	Line 2: 3MARION1 to 3DILLN T		N/A	Yes	Yes
	Line 3: 3WINYAH to 3GTWN s		N/A	Yes	No
Wind energy distributed based on the 5 utilities load ratio			No	Yes	Yes
Total wind energy injection			3080 MW	3080 MW	3080 MW

CHAPTER THREE

OFFSHORE WIND FARM SWITCHING TRANSIENT STUDY

The next chapters focus on the impact of the switching transient of the offshore wind farm on the SC power system. Recently, a switching transient or fault associated with wind farm failures has been reported [18]. The transient overvoltage and inrush current may damage equipment and disturb power delivery as well as affect voltage stability [50]. The resulting equipment maintenance and repair cost are higher for offshore wind farm than for onshore ones. Thus, researchers have investigated in electromagnetic transient in offshore wind farms, with relevant studies have been carried out on such wind farms such as, which is based on fixed speed induction generators. A switching transient impact study requires a detailed model of wind farms. However, it is difficult to model each generator because of simulation time constraints. Using wind farms consisting of large numbers of relatively small, identical generating units makes comparison possible. One of the most frequently used equivalent models for wind farms is based on aggregation of the wind generator units. This chapter presents a DFIG based wind farm equivalent model is presented for switching transient operation analysis. After the equivalent model results are verified with a detailed model, several switching operations are designed to investigate their impact on the system.

3.1 The Equivalent Wind Farm Model

3.1.1 Offshore Wind Farm Collecting Grid for Transient Study

Generalized offshore wind farm grids consist of a large number of identical wind generators, step-up transformers, submarine cables and offshore substations as shown in Figure 3.1. The DFIG model used in this chapter is available at PSCAD's website [36] with the machine parameters listed in Table 1. Each DFIG's capacity is 0.9MW with an output voltage of 0.69kV. This model uses a Synchronized Pulse-Width Modulation (SPWM) converter at the grid side to ensure the constant direct voltage resource for the rotor side converter, which is a Current Reference Pulse-Width Modulation (CRPWM) converter. The stator Flux Oriented Reference Control (FOC) decouples the rotor current to control the DFIG output power and frequency [51]. For the step-up transformer, the DFIG output voltage is raised from 0.69kV to 34.5kV. Saturation is considered, but winding losses and copper losses are neglected in the simulation. All units are connected in parallel to the collecting bus. Wind power would then be transmitted to the offshore substation, which steps up the voltage from 34.5kV to a 115kV transmission system level before its connection to the interface bus onshore. The submarine cables are simulated as pi-section in this model.

3.1.2 Concept Equivalent Modeling for Transient Study

The identical wind generators are connected in parallel in each column, and all columns are connected to the offshore substation. The concept of the equivalent wind generator and its step-up transformer are represented in Equation (3-1) and Equation (3-2).

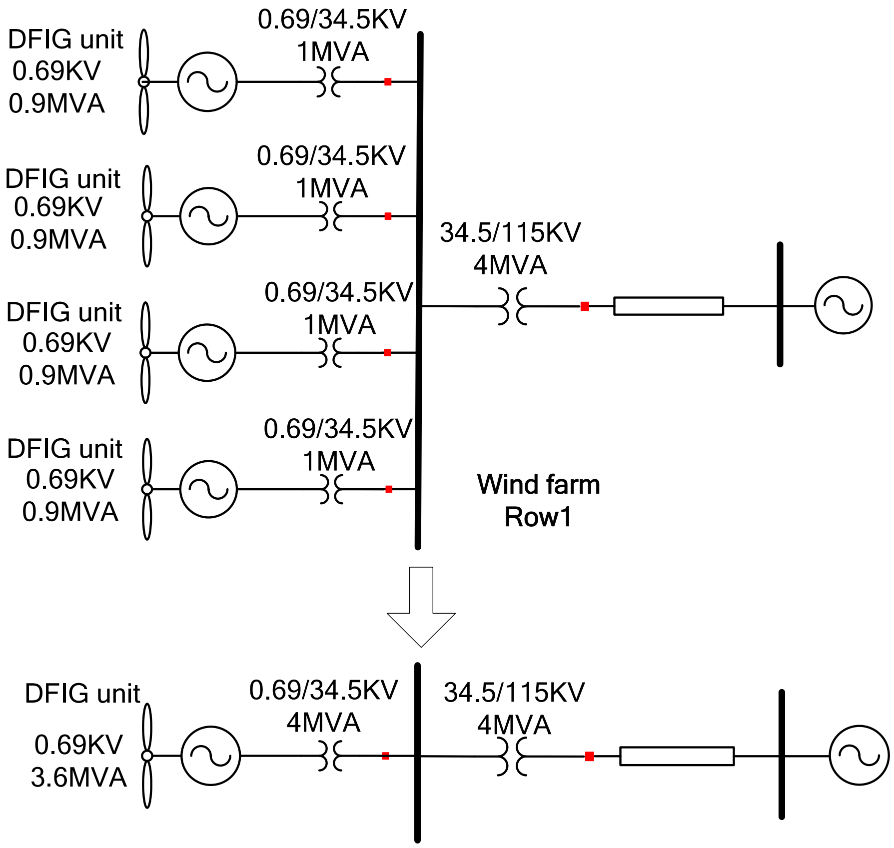

Figure 3.1 Wind farm configuration and aggregation

$$X_{g\_real\_e} + X_{T\_real\_e} = \frac{1}{n} \times \left(X_{g\_real\_d} + X_{T\_real\_d} \right) \cdots\cdots\cdots\cdots\cdots\cdots\cdots (3\text{-}1)$$

$$\frac{1}{n}\left(X_{g\_pu\_e} + X_{T\_pu\_e} \right) \times \frac{V_{base}}{S_{base}} = \frac{1}{n} \times \frac{V_{base}}{S_{base}} \times \left(X_{g\_pu\_d} + X_{T\_pu\_d} \right) \cdots\cdots (3\text{-}2)$$

where,

$X_{g\_real\_e}$, and $X_{T\_real\_e}$ represent the real values of the equivalent wind generator impedance and the transformer impedance, respectively.

$X_{g\_real\_d}$, and $X_{T\_real\_d}$ represent the real values of detailed wind generator impedance and detailed the transformer impedance, respectively;

$X_{g\_pu\_e}$, and $X_{T\_pu\_e}$ represent the per unit values of equivalent wind generators and transformers, respectively;

$X_{g\_pu\_d}$, and $X_{T\_pu\_d}$ represent the per unit values of detailed wind generators and transformers, respectively;

V_{base} represents the rated voltages of individual DFIG.

S_{base} represents the rated capacity of individual DFIG.

The equivalence of the *n* paralleled generator units has the same machine per unit as an individual one, but the capacity base increases by *n* times, as shown in Table 3.1. The machine converter configuration of the equivalent model is the same as the individual model. However, the control parameters need to be changed, this procedure is detailed in the next section.

Table 3.1 DFIG detailed model and equivalent model

Parameter (p.u.)	**Equivalent**	**One DFIG**
MVA	$n \times 0.9$	0.9
V_{stator}	0.69	0.69
R_{stator}	0.0054	0.0054
L_{ls}	0.1	0.1
R_{rotor}	0.00607	0.00607
L_{lr}	0.11	0.11
L_m	4.5	4.5
v_{wind}	12	12

3.1.3 Equivalent Procedure

Based on the equivalent concept, the wind generator and its step-up transformer equivalent modeling is accomplished through the following steps:

Step 1 Using individual DFIG machine parameters (the rotor and stator resistance and the reactance) for the equivalent model;

Step 2 Increasing the rating of the individual DFIG by *n* times for the equivalent model;

Step 3 Calculating the equivalent machine steady state values based on the given machine parameters using the equations (3-3)-(3-9) and using them as reference value for the rotor side control.

Step 4 Adjusting the capacitor and its charging resource to provide smooth DC voltage for the converter on the rotor side as shown in Figure 3.2;

Step 5 Selecting the appropriate rating for the transformer on the grid side converter based on the rotor voltage calculated;

Step 6 Tuning the PI controller’s parameter for both the rotor side current loop and grid side voltage loop for optimal transient study.

$$I_s = \frac{P_s}{3 \times V_s \cos\varphi_s} \tag{3-3}$$

$$I_r = \frac{\Phi_r - L_{lm} I_S}{L_r} \tag{3-4}$$

$$I_s \times R_s - V_s = -j\omega_1 \Phi_s \tag{3-5}$$

$$I_r \times R_r - V_r = -j\omega_1 s \Phi_r = E_r^{'} \tag{3-6}$$

$$I_s \left(R_s + j\omega_1 L_s\right) - V_s = -j\omega_1 L_{lm} I_r = E_p^{'} \tag{3-7}$$

$$-R_r \frac{L_m}{L_r} I_s + \left(\frac{R_r}{L_r} + js\omega_1 \right) \Phi_r = V_r \quad \cdots\cdots (3\text{-}8)$$

$$I_s \left(R_s + j\omega_1 L_{sc} \right) + j\omega_1 \frac{L_r}{L_m} \varphi_r = V_s \quad \cdots\cdots (3\text{-}9)$$

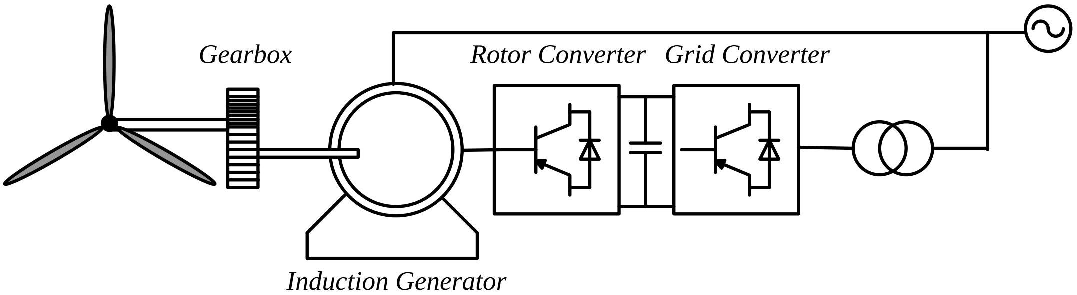

Figure 3.2 Control blocks for DFIG

3.1.4 Equivalent Model Verification

Because of the limitation of the PSCAD, the maximum four DFIG detailed models (0.9 MW each) can be run to verify the results obtained from the equivalent model (3.6 MW) results as shown in Figure 3.3 - Figure 3.5. The generators start from speed control until *t*=0.5 sec when the torque control is engaged. The active output power of the two models is shown in Figure 3.3. The steady state results from 0 sec to 3 sec exhibit negligible differences between the two models. The load is switched on at the system interface bus for both models when *t*=3 sec phase A voltage achieves zero crossing. When the load is switched on, the overshoot of output power is followed by a distortion, the transient of which lasts for 2 sec before arriving at a new steady state. The maximum error between the two models at active power is 8.3% as shown in Table 3.2. This model is suitable for studying switching transients, but it will require further refinement if a stability analysis is involved.

Table 3.2 Comparison of two models

—	Voltage	Current	Active Power
Max Error %	0.29%	8.71%	8.3%

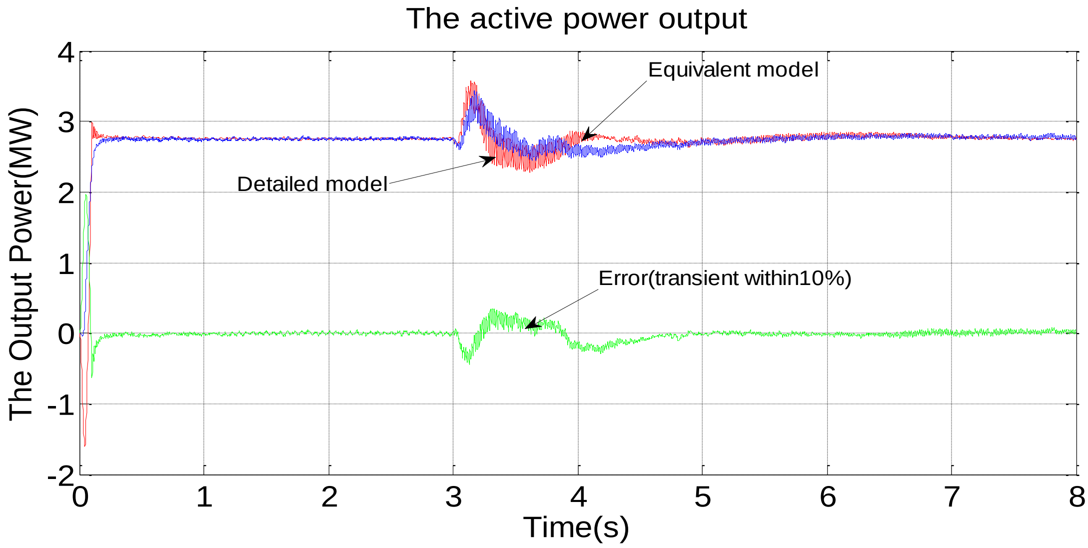

Figure 3.3 The comparison of active power outputs between two models

The phase to phase voltage at the wind farm collection bus during load switching has a very small transient as shown in Figure 3.4. The error between the two models, which is shown in green, is less than 0.29% as shown in Table 3.2.

The current of wind farm experiences overshoot before arriving to steady state as shown in Figure 3.5 and the maximum error between the two models is 8.71% as illustrated in Table 3.2.

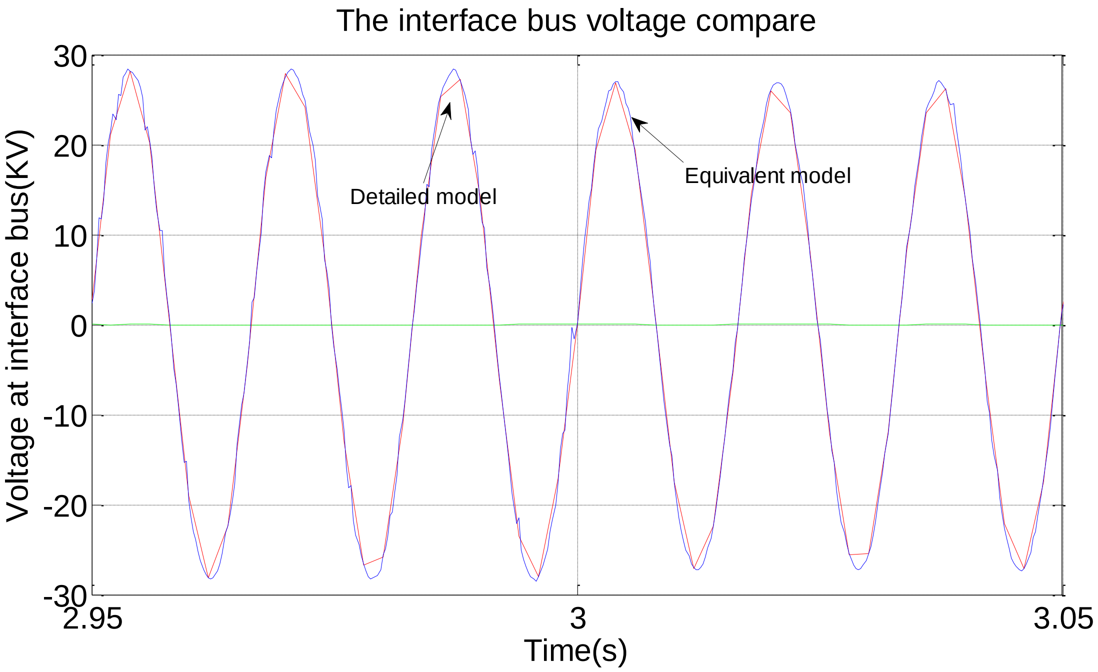

Figure 3.4 Interface bus voltage comparison

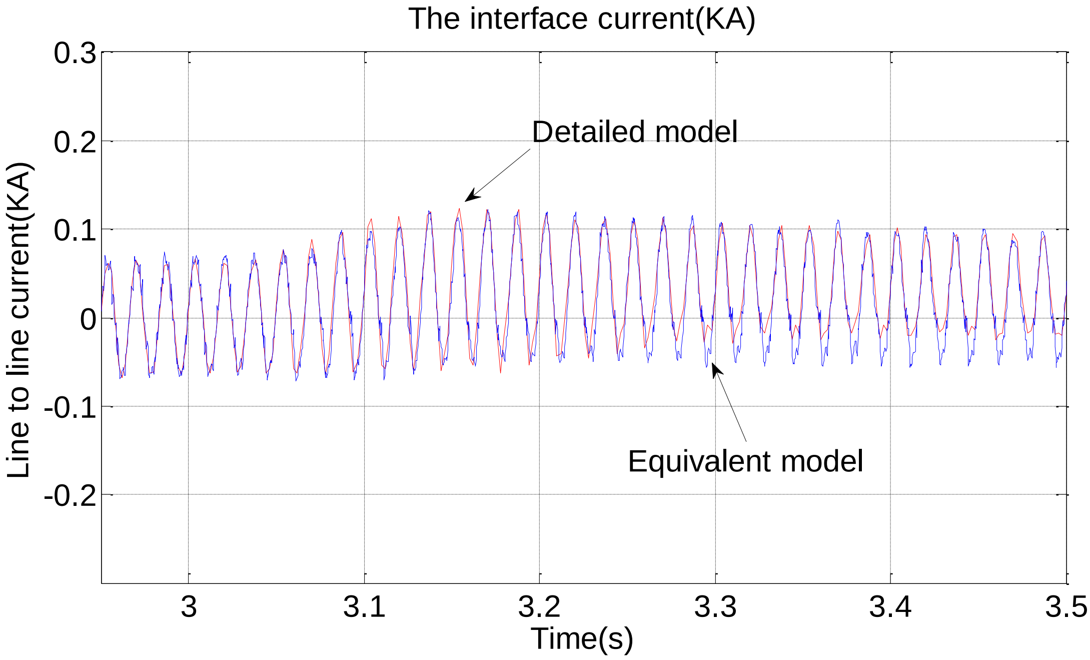

Figure 3.5 Interface bus current comparison

3.2 Wind Farm Switching Transient Impact on Power System

3.2.1 40MW Wind Farm Integrated SC System Units

Using the method detailed in the previous section, a 40MW equivalent wind farm is established and connected to South Carolina Thevenin's equivalent impedance. Wind power is generated and delivered to the offshore substation before its integration into the system as shown in Figure 3.6.

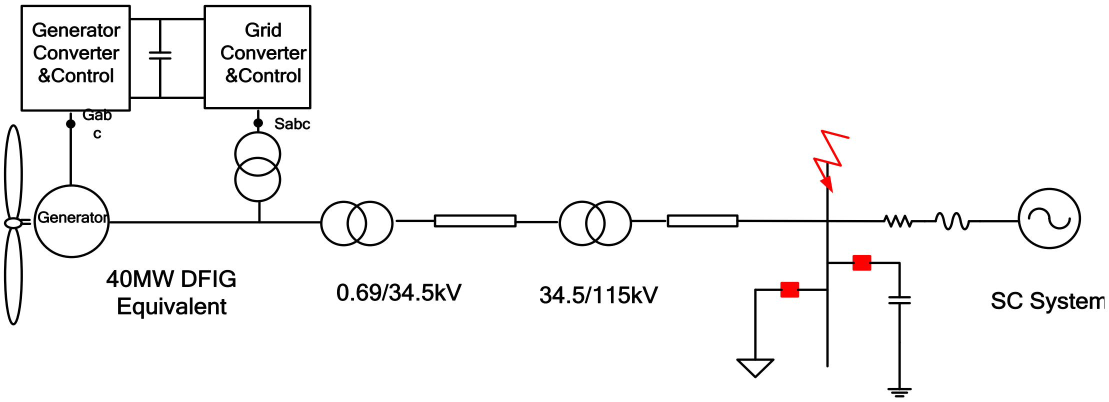

Figure 3.6 40MW equivalent wind farm integration

The steady state voltage and current at wind farm output bus are shown in Figure 3.7 and Figure 3.8.

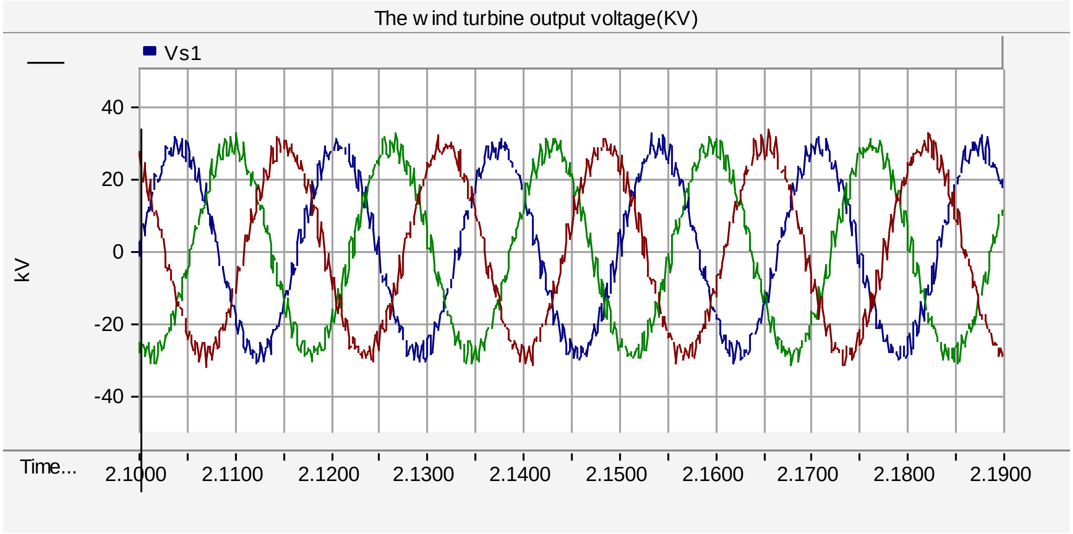

Figure 3.7 40MW equivalent wind farm output voltage

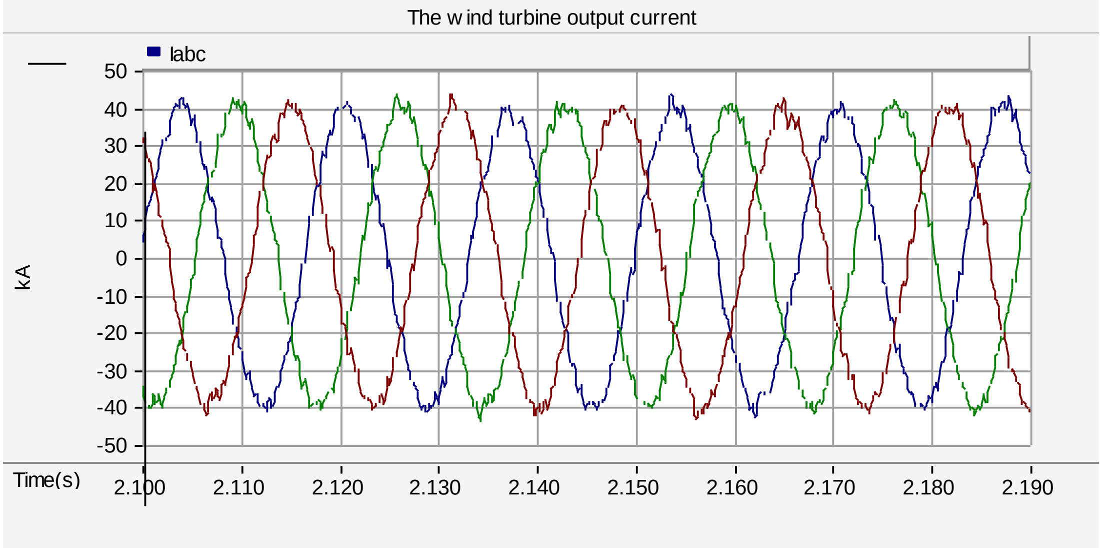

Figure 3.8 Current output of 40MW equivalent wind farm

The DFIG converter distortion can be observed in the wind farm output voltage and current. The current output of the equivalent machine is analyzed using FFT. It can be observed that 5th, 7th, and 11th harmonics are present with their Total Harmonic Distortion (THD) being 0.794%, which is less than 1% of the fundamental frequency as shown in Table 3.3.

Table 3.3 Harmonic components in the wind farm current

	Harmonic 5th	Harmonic 7th	Harmonic 11th
$\frac{I_h}{I_{base}}$	0.3%	0.6%	0.425%

The power output of the equivalent wind farm with a unity power factor is shown in Figure 3.9. The output power of the DFIG can be adjusted through the wind speed and the slip of each generator.

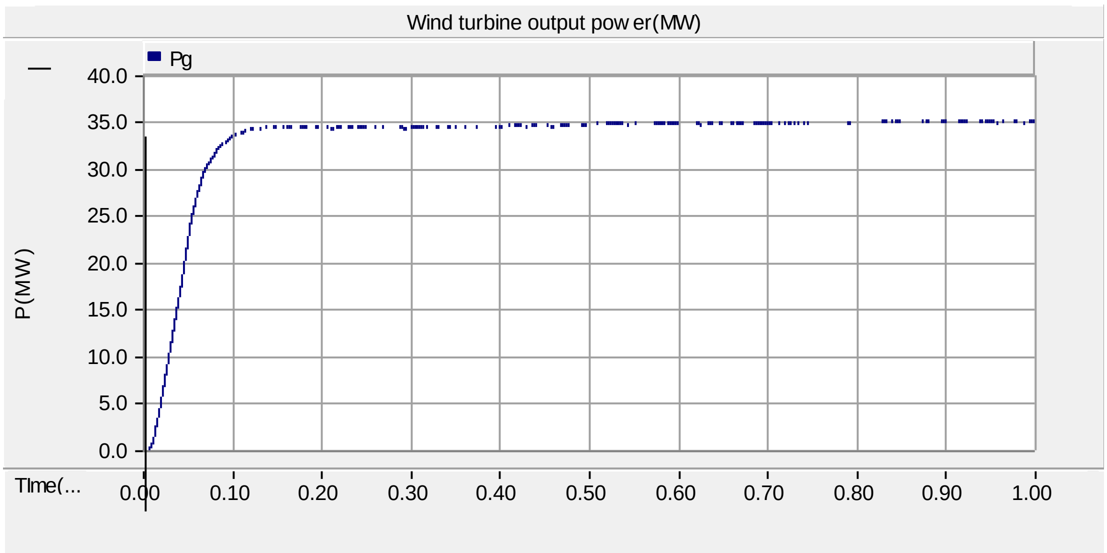

Figure 3.9 Power output of 40MW equivalent wind farm

3.2.2 Cable Energizing in Wind Farm Equivalent

Cable energizing is frequently operated inside wind farms. After the DFIGs are started and synchronized, they are then switched to the system and wind power is generated after the cable is charged. As seen in Figure 3.10, the cable is switched at *t*=3sec. at which time the offshore substation bus voltage of phase A experiences a voltage dip when the cable is switched on, as shown in Figure 3.11. The simulation results indicated that the more paralleled cables that are switched on, the larger the voltage decrease at the substation bus.

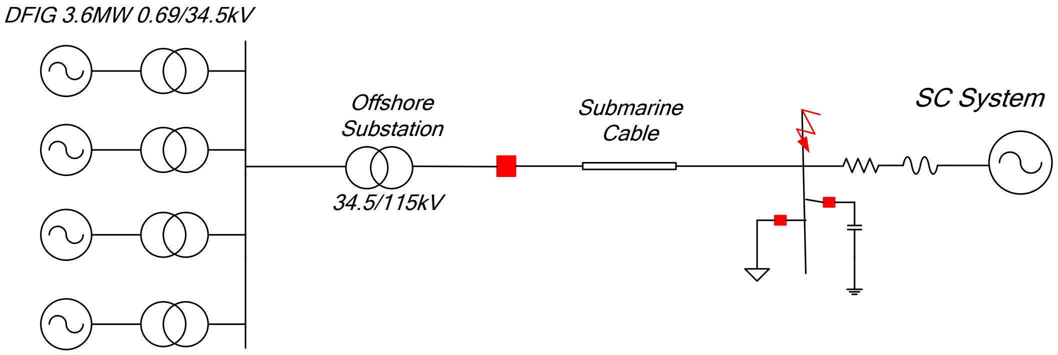

Figure 3.10 Cable energizing wind farm

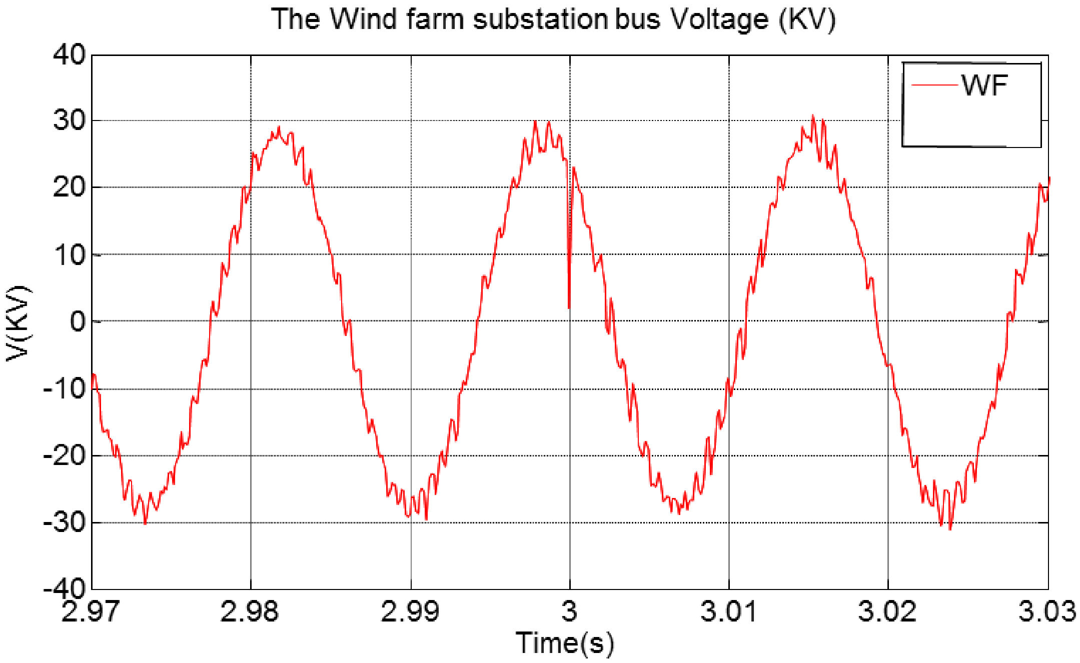

Figure 3.11 Voltage at the substation at cable switching

3.2.3 Three-Phase Fault at Different Locations in a Wind Farm

The three-phase fault at various locations in wind farm has different impacts on the system. In this section, it is assumed that the three-phase fault occurs at the DFIG unit output bus (location A), the substation bus (location B), and the system interface bus (location C) as shown in Figure 3.12. All the faults occur at *t*=3sec, lasting for 0.15s before being cleared.

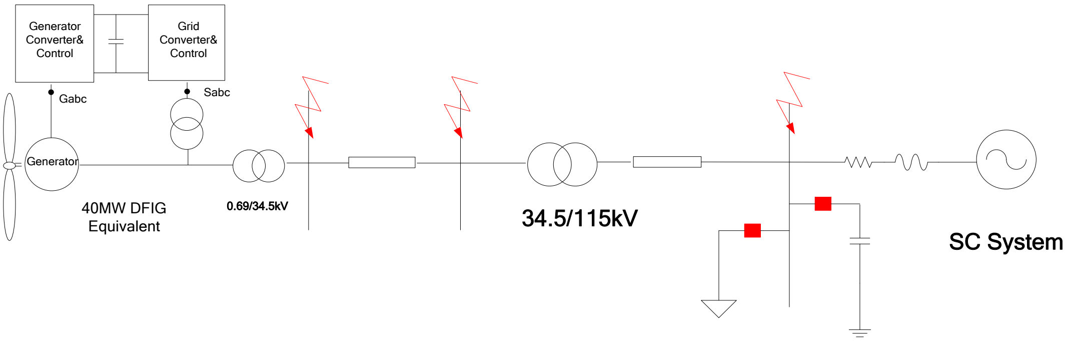

Figure 3.12 The three-phase fault in a wind farm

The fault current at the various locations are shown in Table 3.4. The maximum fault current occurs at the interface bus, where the value reaches 68 kA. The minimum fault current, which occurs at DFIG bus, is 14.5 kA.

Table 3.4 Comparison of three-phase fault at different locations

Fault	I_{fmax} (kA)	P_{max} (MW) /Overshoot	V_{max} (RMS) /Overshoot
Location A	14.5	45.2/31.03%	0.98/-2%
Location B	19	64.5/86.96%	1.01/1%
Location C	68	71.25/106.52%	1.07/7%

The fault current injected by the wind farm reaches approximately 2.5 times of rated value when the three-phase fault occurs. When the fault is cleared, the largest recovery current injected from the wind farm reaches approximately 4 times the rated value as shown in Figure 3.13.

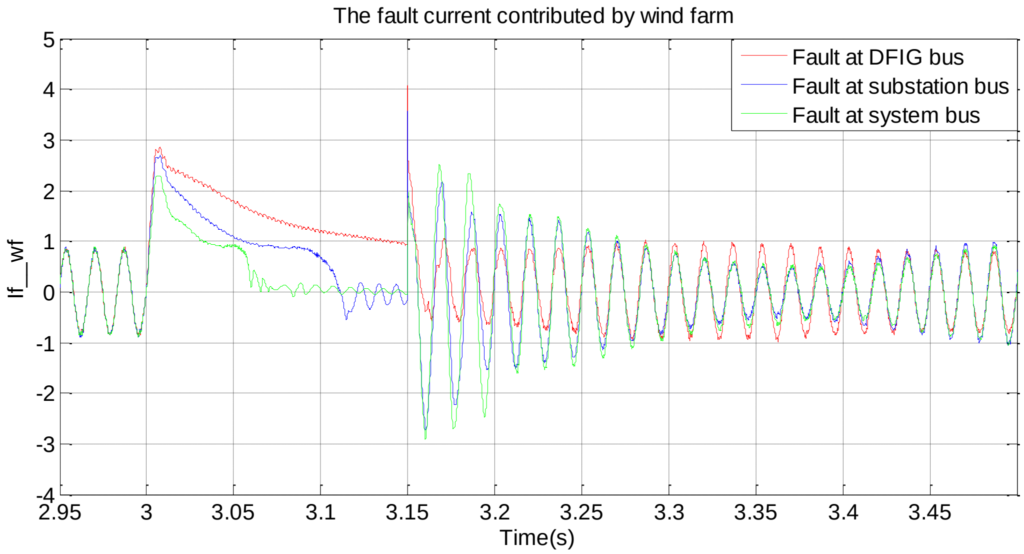

Figure 3.13 Three-phase fault currents at different locations

The fault currents injected by the wind generators are small compared to the one from grid as shown in Figure 3.14.

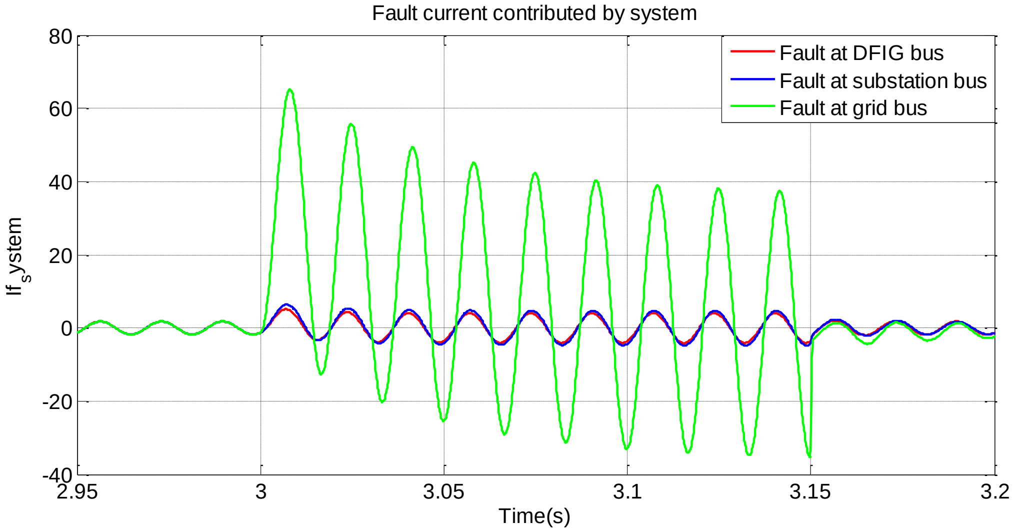

Figure 3.14 Wind farm injected fault current at different location fault

The wind farm output power disturbance due to the fault at various locations is shown in Figure 3.15. The power is interrupted during faults, and generators experience fluctuation before the power reaches its steady state value. The maximum power output fluctuation of the wind farm occurs when a fault is located at the system interface bus, the overshoot of which reaches 71.25 MW. The minimum power output fluctuation occurs when a fault is located at the DFIG output bus.

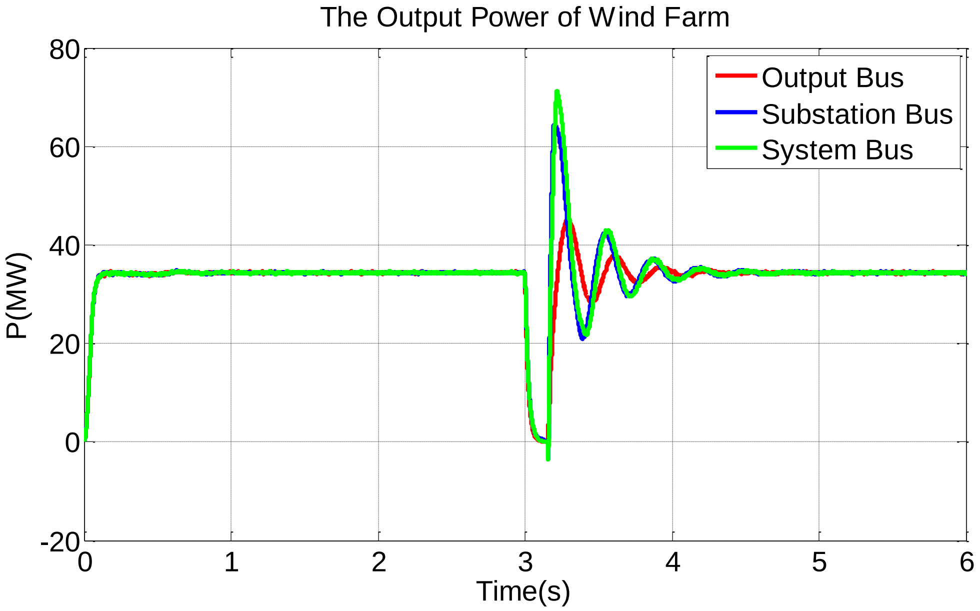

Figure 3.15 Three-phase fault power at different locations

The voltage drop due to a fault at different locations in the wind farm is shown in Figure 3.16, a voltage dip during a fault can be affected by the capacitor bank in the DFIG converter. After the fault is cleared, the voltage reaches its steady state. The maximum overvoltage of 7% occurs when a fault is located at the system interface bus while the minimum happens when a fault is located at the DFIG output bus.

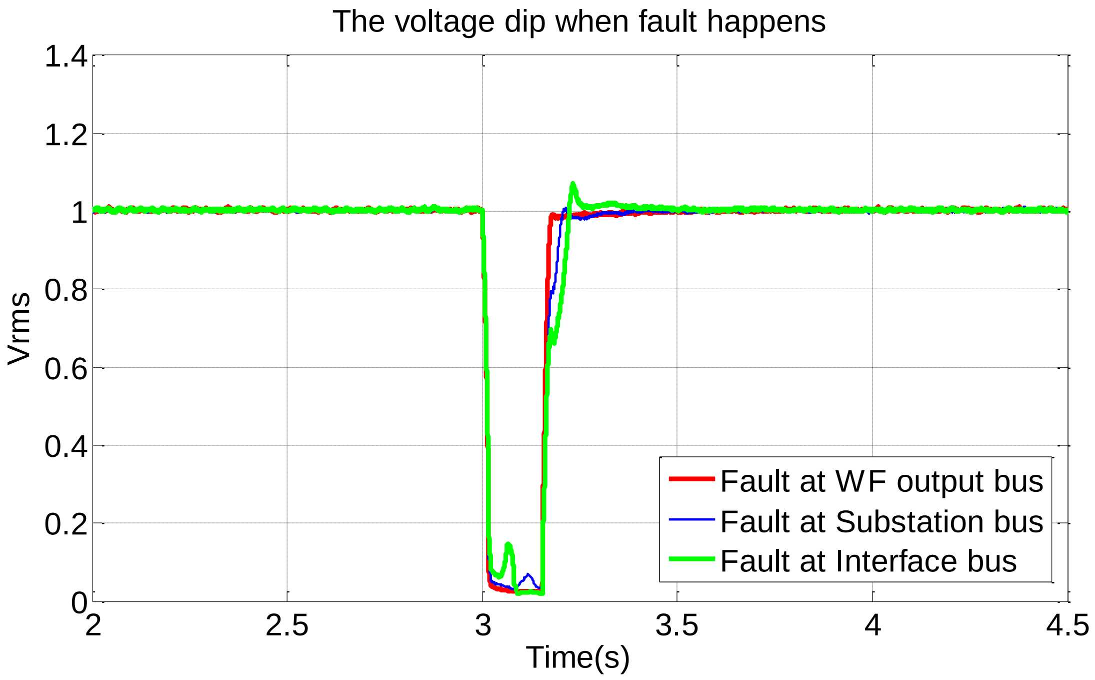

Figure 3.16 Three-phase fault voltage RMS at different locations

Figure 3.17 illustrates the recovery voltage at the offshore substation bus when fault is cleared at *t*=3.15sec at three locations. The max transient recovery voltage distortion occurs when a fault is located at the system interface bus while the minimum transient happens when a fault is at the DFIG output bus.

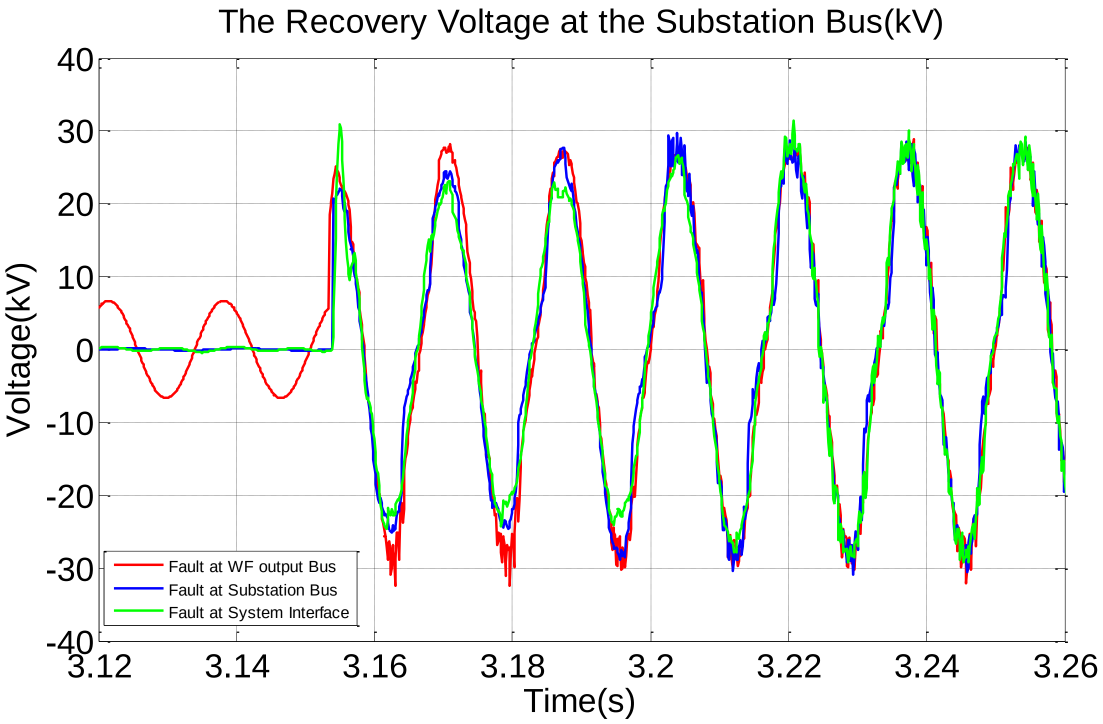

Figure 3.17 Recovery voltage after the faults have cleared

3.3 Conclusions

An offshore wind farm switching transient would impacts the injection system. The simulation of this switching transient requires appropriate models of wind farm equipment. The one used here indicated that load switching in the connected system causes a dynamic power fluctuation in wind farms. In addition, cable energizing causes a voltage dip in the connected bus: the more paralleled cables charged at the same time, the greater this voltage dip. Different fault locations in wind farm cause disturbances in the system.

CHAPTER FOUR

SWITCHING TRANSIENT IMPACT OF OFFSHORE WIND FARM ON POWER SYSTEM

Given their frequency in a system, switching operations can be a source of transient overvoltage or inrush current, both of which cause stress on the insulation material of the equipment, malfunction of the protection, shedding of the load, or damage to the equipment, resulting in the instability in the system [52]. They also affect wind farm operation because of the switching transient. Thus, the impact of this switching transient on power systems with offshore wind farms is important to investigate. Large power system electromagnetic transient studies require detailed modeling of specific parts, and the remaining parts of the system have to be reduced as equivalent impedance [53].

Research focusing on the switching transient impact of an offshore wind farm on the system is shown in [54]. The first consideration needing to be addressed for a study of the effect of a transmission system switching transient for a large scale offshore wind farm is whether to use appropriate equivalent models for each component in the power system [55][56][57][58]. As shown in Figure 4.1, a configuration and aggregation of an offshore wind farm consists of identical DFIGs; this type of aggregation DFIG model should be available before studying the transient impact.

After modeling, the switching transient analysis determines the solutions for ordinary differential equations under switching operating conditions. They can be solved either using an analogue or a digital simulator [52]. Analogue simulation is appropriate for simple systems. For electrical power system whose variables are continuous, suitable methods have to be chosen to solve the differential equations at discrete points. As mentioned in Chapter One, numerical integration and difference equations are two methods for converting a continuous system into a discrete one to solve differential equations. Software based on the discrete algorithm includes EMTP, EMTDC/PSCAD, among others.

The research reported in this chapter continues the investigation of the influence of switching transient offshore wind farms on the SC power system. In this chapter, both offshore wind farms (OWF) and the SC power systems are modeled in detail and implemented. In addition, various different system modeling are studied to investigate the switching transient impact of OWF connected power systems. After establishing the system model, different scenarios including capacitor bank switching, the three-phase fault and its clearance are examined. In order to better observe the switching transient impact of offshore wind farms on the SC power system, the results are compared with those obtained from system supplied by a comparable conventional generator. The transient frequency is analyzed in frequency domain.

4.1 System Description

4.1.1 Offshore Wind Farm Equivalent Model

Since offshore wind farms consist of large numbers of relatively small, identical generating units, a GE 3.6 MW wind turbine for example, it is possible to build equivalent models without losing accuracy. One of the ways to establish equivalent models for wind farms is by aggregating wind generator units. This section adopts the OWFs equivalent model developed and verified using a 3.6MW model in previous chapter, meaning a 40MW DFIG based wind farm equivalent model is used here for switching transient operation analysis. Several switching operations are considered to investigate their impact on the system.

4.1.2 South Carolina Reduced System

The first system to be simulated focuses on the surrounding area of two OWFs surrounding areas with the remaining connected as Thevenin equivalent impedance and infinite voltage sources. The OWFs are injected into the system through selected interface buses Dunes as (D) and Winyah Bay as (W) based on the previous study as shown in Figure 4.2. This reduced South Carolina power system is composed of approximately 61 buses and 21 plants with a total capacity of 2064.7MW.

Table 4.1 SC reduced system data

System Information	Numbers
System Generation	2064.7MW/1773.5MVar
Constant Load	1903.9MW/569.5MVar
Bus Number	61
Plants Number	21
Fixed Shunt	16
Switched Shunt	10
Load Number	37
Branch Number	86
Transformer Number	31

The system data are listed in Table 4.1, and the wind farm penetration level is:

$$\frac{80\,\mathrm{MW}}{2064.7\,\mathrm{MW}} \times 100\% = 3.87\% \quad \cdots\cdots \quad (4\text{-}1)$$

4.1.3 South Carolina intentional islanded power system

Intentional islanding [59][60] is the purposeful separation of the utility system during a specific operation mode to create power "islands". Previously, due to the large capacity of the connected system compared to the OWF, the penetration level was 3.87%, and the transient could not be observed clearly. In order to better investigate the impact of an offshore wind farm switching transient, an intentional islanded system is created around OWFs connecting points to reduce the system size further. The system is assumed to operate under a light loading condition in which large generators are operating at minimum capacity and the large loads are disconnected from the system. The system size reduced using PSSE based on the previous section is listed in Table 4. 2. The intentional islanded system size was decreased to 46 buses with the capacity of 602MW. The system data are listed in Table 4.2.

Table 4.2 Intentional islanded system data

System Information	**Numbers**
System Generation	602.1MW
Constant Load	595.6MW
Bus Number	46
Plants Number	10
Fixed Shunt	16
Switched Shunt	10
Load Number	8
Branch Number	70
Transformer Number	19

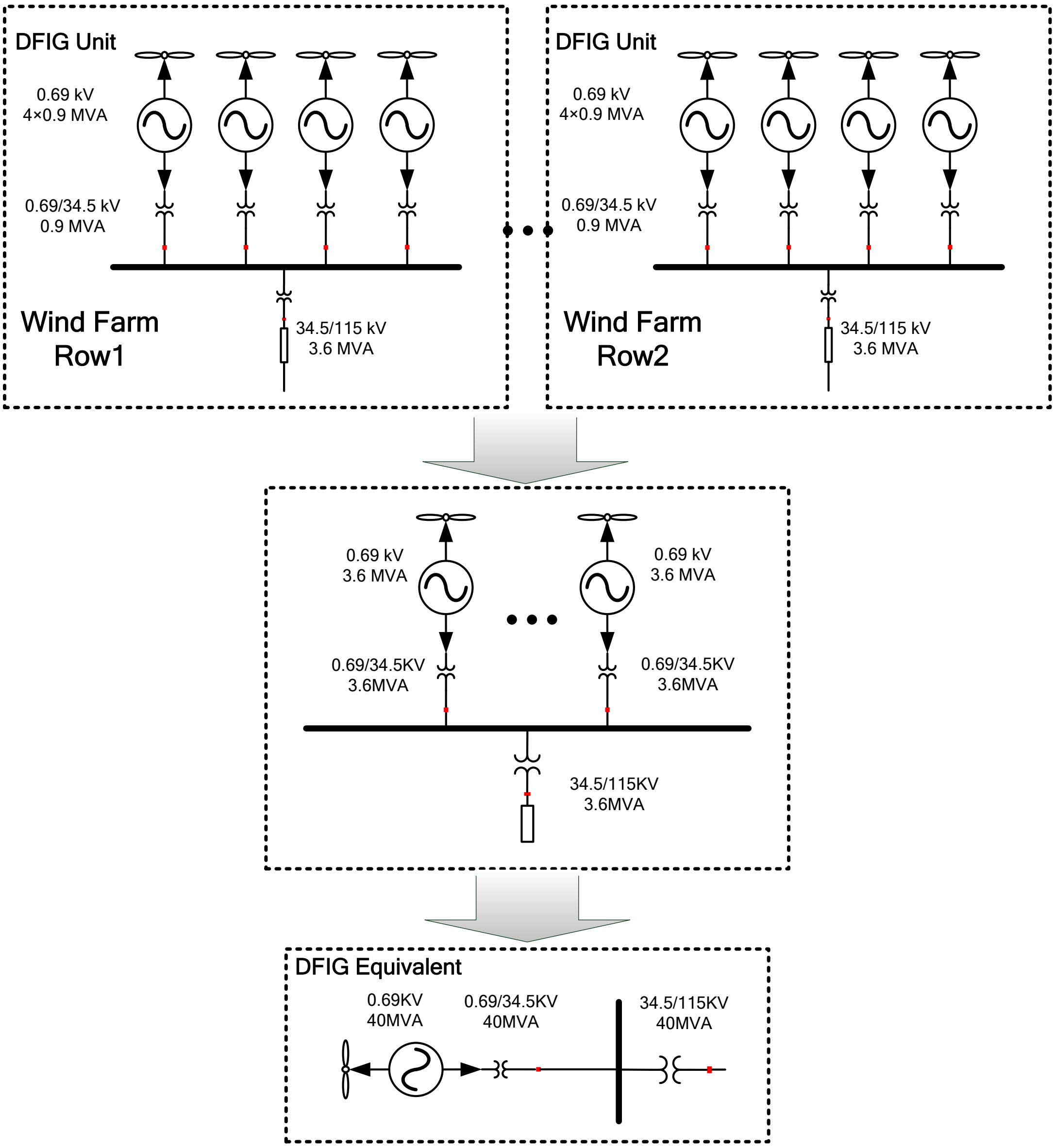

Figure 4.1 Wind farm configuration and aggregation

The penetration level is increased to:

$$\frac{80\,\mathrm{MW}}{602.1\,\mathrm{MW}}\times 100\% = 13.29\% \quad \cdots\cdots\cdots\cdots\cdots\cdots\cdots\cdots\cdots\cdots (4\text{-}2)$$

The system diagram in PSSE is shown in Figure 4.2. The OWFs are injected into the system through selected interface buses Dunes (D) and in Winyah Bay (W).

Switching operation and faults are placed in the system, and the results are compared with those of a comparable system supplied by conventional generation.

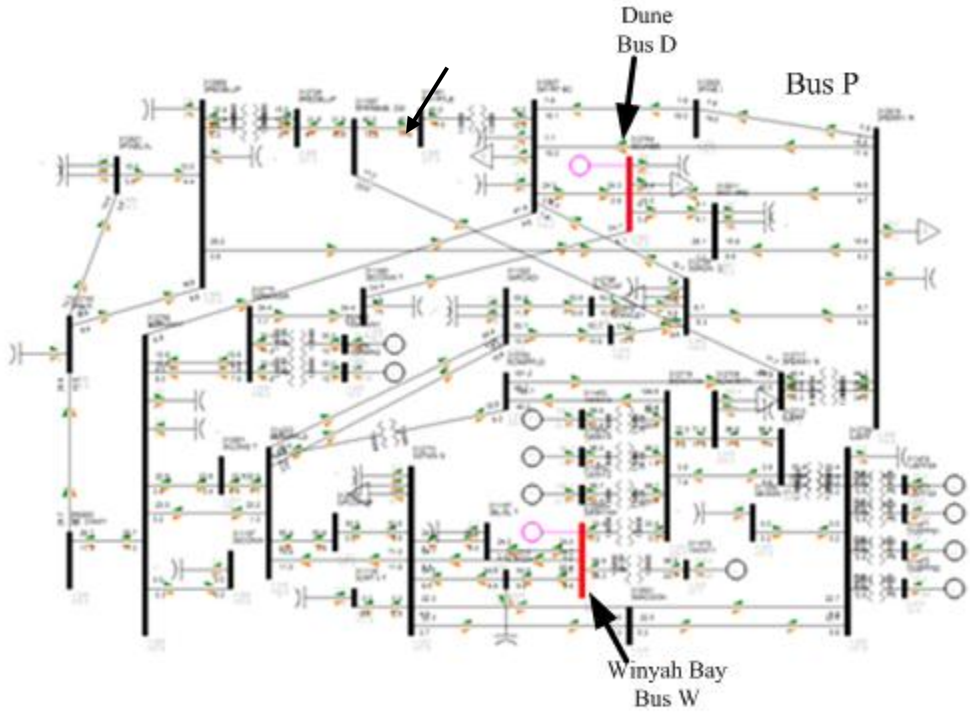

Figure 4.2 Intentional islanded zone

4.2 Computer Modeling Procedure

4.2.1 South Carolina Reduced System

Usually the system data are given as PSSE sav files or raw files, both of which need to be translated into PSCAD before connecting the OWFs. After reducing the systems in PSSE based on the different operation modes, the network data are translated into PSCAD by ETRAN as shown in Figure 4.3. The 40MW equivalent OWF model is connected at the selected interface bus of the system.

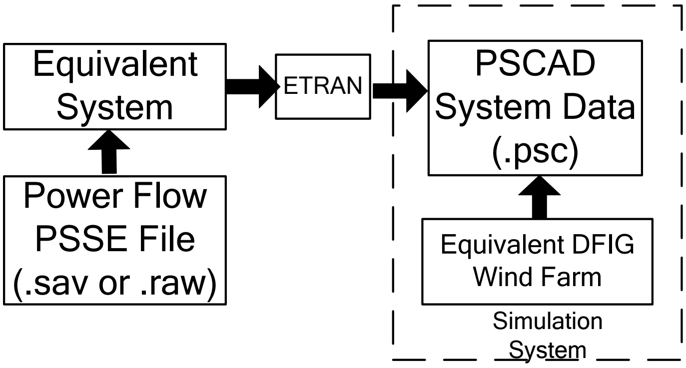

Figure 4.3 System modeling in PSCAD

Based on the system modeled in PSCAD, the switching scenarios, capacitor bank switching and three-phase fault analysis, are carried out to simulate various operations in the system with offshore wind farms. Since the system to be reduced is too far away to affect the frequency performance of the highlighted small scale OWF-surrounded system, for the purpose of this case, non-frequency dependent network equivalents are used. After selecting a specific zone, the original system is modeled as an equivalent one in PSSE according to the interface requirements.

4.2.2 Equivalent PSCAD Model Imported From PSSE

Case 0: The original data are in PSSE31 Format. Using the 2007 series SERC LTSG power flow model of the 2013 summer peak data which includes 50988 buses, 6009 power plants, and machines 7072 machines without wind machines included.

Case 1: The four areas include CPLE, CPLW, Duke, SCE&G, and Santee Cooper; a voltage level above 110kV; a generator above 100MW retained from the equivalent system; a retain area boundary bus; retain control buses;

Case 2: Six interface buses in Zone 342 and 1375; a voltage level above 110kV; a generator above 100MW retained from the equivalent system; retained area boundary buses; retain control buses.

The cases data are listed in Table 4.3

Table 4.3 Equivalent cases summaries

	Bus Number	**Plant Number**	**Fixed Shunts**	**Loads**	**Branches**	**Transformer**
Case 0	50988	6008	3306	31078	67195	19475
Case 1	684	185	203	565	1942	229
Case 2	165	123	101	114	1129	61

As shown in Figure 4.4, Etran bridges the gap between the phasor-based load flow and the stability simulation tools and electromagnetic transient (EMT) tools. It solves the steady state phasor equations and uses this information to initialize a PSCAD/EMTDC circuit as well as to form network equivalents to reduce the network so that it is suitable for transient analysis.

Figure 4.4 Data imported from PSSE to PSCAD

The steady state solution in PSCAD/EMTDC is based on the solution of instantaneous differential equations, whereas the solution in PSS/E or load flow programs is based on phasor-based complex variable calculations at the fundamental frequency. The load flow information is used by ETRAN to initialize the circuit in PSCAD/EMTDC.

4.2.3 South Carolina Intentional Islanded Power System

The procedure for modeling the intentional islanded zone in PSCAD is listed below:

Step 1 Determine the system to be islanded. For this research, this system is the east zone of the SC power system;

Step 2 Determine the power flow at the tie lines and the connection buses in the zone into which the OWFs are injected. The power flow on the tie line between the zones is listed in Figure 4.5;

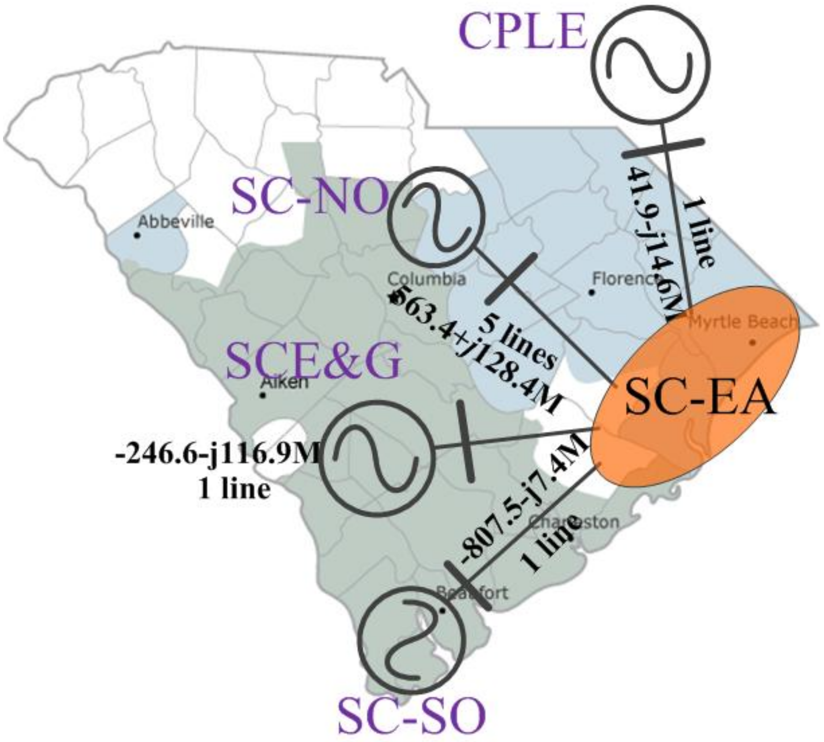

Figure 4.5 Intentional islanded zone and tie lines

Step 3 Use the interface bus voltage as the voltage source and the power flow at tie line as the equivalent generator output capacity as shown in Figure 4.6.

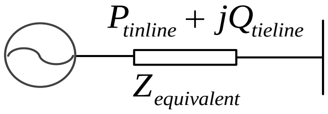

Figure 4.6 Equivalent for the rest system

Now the impedance can be calculated using Equation (3),

$$Z_{tieline} = \frac{V_{tieline}^2}{(P_{tieline} + jQ_{tieline})^*} \quad \cdots\cdots\cdots\cdots\cdots\cdots\cdots\cdots\cdots\cdots\cdots\cdots\cdots\cdots\cdots (4\text{-}3)$$

Step 4 The system outside the SC east zone power system is an equivalent as voltage resource and impedance as shown in Figure 4.7;

Step 5 Keep the generator above a 200MW run as the minimum output and reduce the same amount of load;

Step 6 Run PSSE until the power flow converges;

Step 7 Load the converted PSSE raw file in ETRAN; then convert the PSSE file into a PSCAD file for the electromagnetic transient study; and

Step 8 After the system is converted into PSCAD, the OWFs equivalent model can be connected to the interface bus, and the simulation cases applied to investigate the switching transient impact.

4.3 Case Simulation

This section analyses the simulation results from the reduced South Carolina power system and the corresponding intentional islanded power system modeled with connections of the offshore wind farm equivalent system. Switching operations including capacitor bank switching, three-phase fault application and its clearance, and the disconnection of the wind farm from the system will be analyzed and the results are discussed.

4.3.1 Capacitor Bank Switching and the Three-Phase Fault

Capacitor bank switching frequently occurs in power systems for voltage regulation and power factor improvement. In the first case, the 30MW capacitor bank located at the OWFs neighboring bus P is switched on at *t*=0.2 sec. The transient voltage waveform at the wind farm interface bus D obtained as seen in Figure 4.7 indicate that the switching has little impact on the OWF bus.

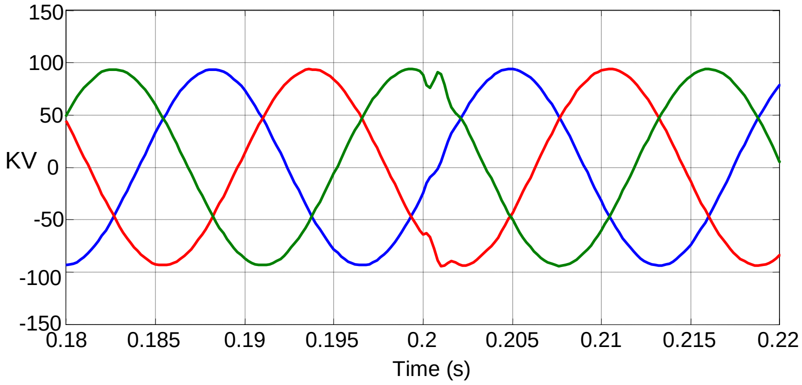

Figure 4.7 Voltage wave of the capacitor switching

Assume that at *t*=0.2 sec the three-phase fault occurs at bus P and lasts for 0.05s before it is cleared itself. The voltage transient at the wind farm interface bus is shown in Figure 4.8. The voltage deceases by 40% during the fault and the transient recovery voltage overshoots by 20%.

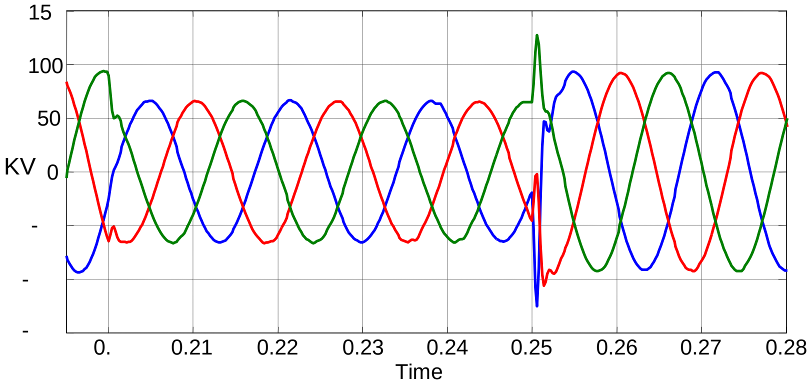

Figure 4.8 Voltage wave of three-phase fault

4.3.2 Offshore Wind Farm Disconnection

The wind farm is disconnected from the system when the wind is blowing too strongly. This section analyzes the simulation conducted to investigate the transient caused by the disconnection of the OWF from the SC power system. It is assumed that the wind farm at Dune (bus D) would be disconnected at *t*=0.2 sec. The voltage transient at the wind farm interface bus is illustrated in Figure 4.9.

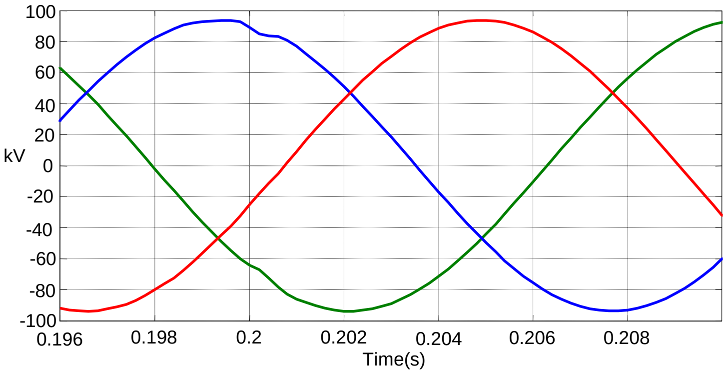

Figure 4.9 Voltage wave of OWF disconnection

As shown in Figure 4.9, due to the low penetration, the disconnection of the OWF has a negligible effect on the South Carolina equivalent system.

For the islanded system surrounding a small region of the OWFs, a 30MW capacitor bank located at the OWFs neighboring bus P as shown in Figure 4.2 is switched on at *t*=0.2 sec. The transient current waveform for the capacitor bank obtained is shown in Figure 4.10. The blue plot represents the system supplied by the same amount of conventional generation at the OWFs interface bus, and the red plot, the DFIG equivalent wind farm supplied system. As seen from Figure 4.10, both transients die out within a half cycle. However, a harmonic is present in the capacitor bank inrush current in the system supplied by the OWFs during steady state.

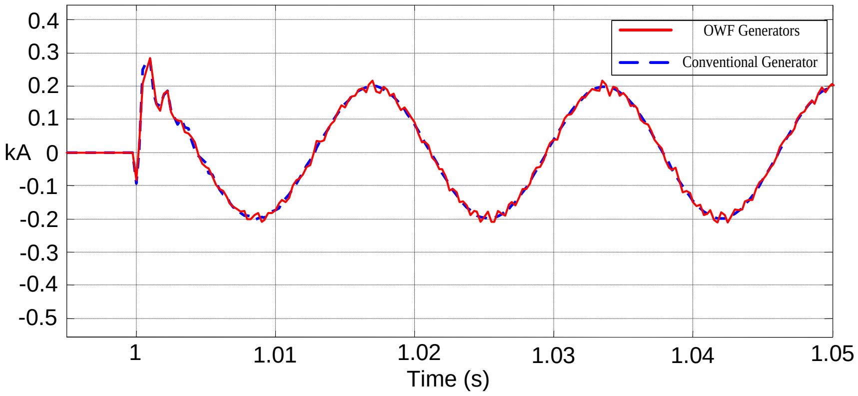

Figure 4.10 Capacitor bank inrush current at bus P

The frequency analysis for the capacitor bank current is given in Figure 4.11. The main harmonic component is the 19th order and the amount is approximately 3% in comparison with the fundamental frequency component. As seen in Figure 4.11, the system supplied by the OWFs has more frequency components than the system supplied by conventional generator during the capacitor switching transient.

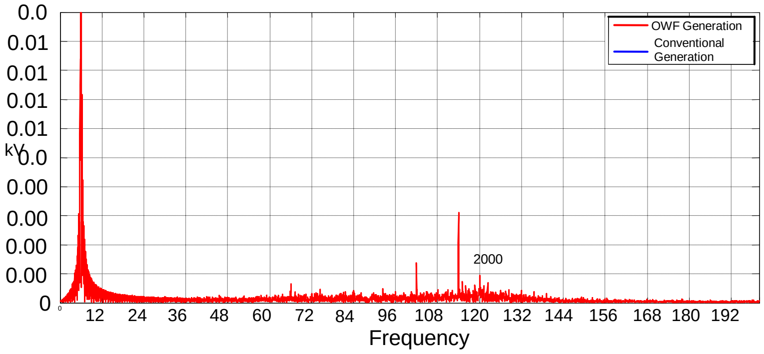

Figure 4.11 Frequency analysis of the capacitor inrush current at bus P

4.3.3 Three-Phase Fault and its Clearance in the Intentional Islanded System

A three-phase fault occurs at bus P at *t*=0.6 sec, lasting for 0.05 sec before it clears itself. Figure 4.12 and Figure 4.13 show the transient recovery voltage of the wind farm interface bus when the fault is cleared.

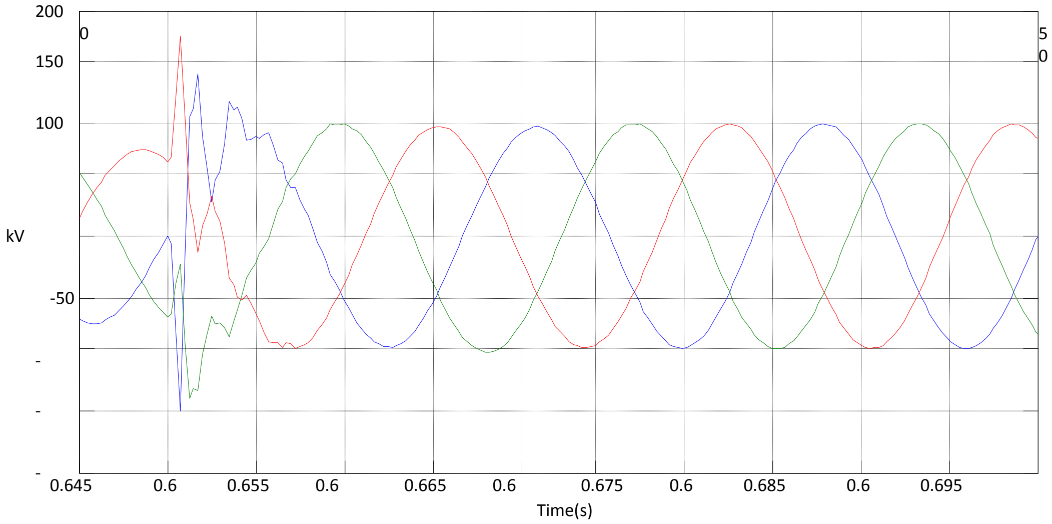

Figure 4.12 Transient recovery voltage of the OWFs supplied system

Figure 4.12 shows the system supplied by the OWFs, and Figure 4.13 for the system with the same amount of conventional generation at the OWFs interface bus. Both transient die out within one cycle. However, the system supplied by conventional generators exhibits a worse transient than the OWFs supplied system with greater overvoltage and a longer transient period.

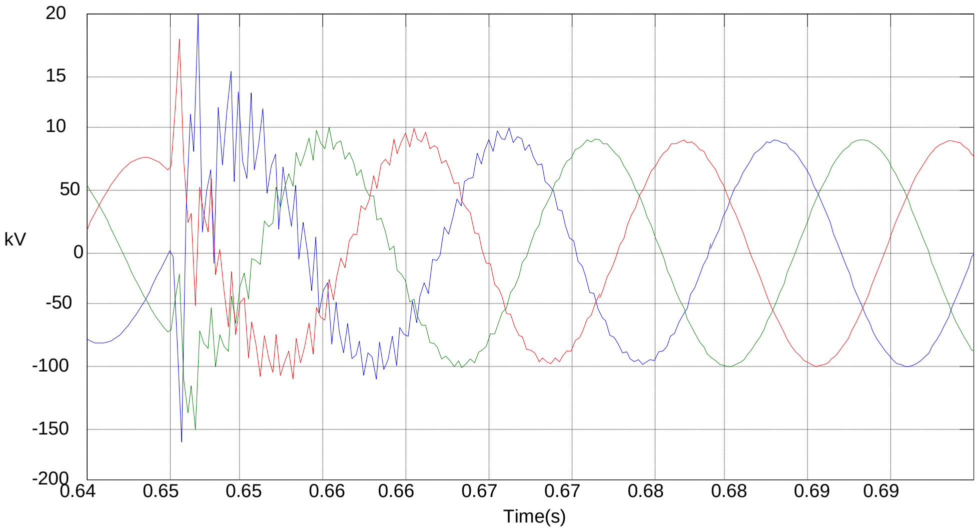

Figure 4.13 Transient recovery voltage of the conventional generator system

For the frequency analysis shown in Figure 4.14, the system supplied with conventional generator exhibits a higher frequency component other than the system supplied by the OWFs because the DFIG grid side converter contributes to the system transient voltage.

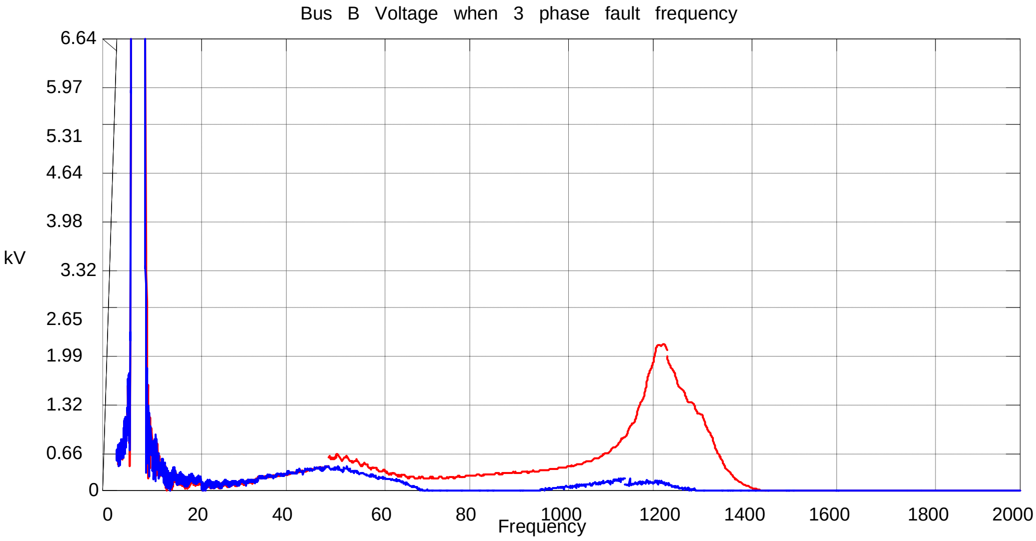

Figure 4.14 Frequency analysis of the transient recovery voltage

4.4 Conclusions and Future Work

Based on the study reported in this chapter, it can be concluded that:

1. For the South Carolina power system with surrounding area as equivalent systems, 80MW offshore wind farm does not affect system switching transient significantly because of small capacity.

2. The steady state analysis of the islanded system indicates that the DFIG wind farm inject the 19th harmonic into the system.

3. During the transient period (within 1 cycle) for the light load with the minimum generation and the intended islanding system, the doubly fed induction generators based offshore wind farms exhibit less transient compared to the regular generators.

4. For future work, the wind farm capacity should be increased by another 1GW, and the corresponding studies conducted to determine the effect of this increase.

.

CHAPTER FIVE

FREQUENCY DOMAIN ANALYSIS OF THE IMPACT OF THE OFFSHORE WIND FARM SWITCHING TRANSIENT

5.1 Introduction

For the transient analysis of large systems with wind farms integrated using a digital simulator, the detailed data about the system has to be available before the simulation. While the time domain simulation can provide the switching transient impact of the offshore wind farm on the system by modeling it in such software as PSCAD or EMPT, in some case when data from the entire system are not available, an equivalent system model has to be built or as an alternative, the appropriate system equivalent models have to be provided. However, for practical engineering projects studying the impact of the wind farm transient impact on the system, it’s difficult to acquire the detailed system data and build the entire system in transient software for the analysis. Even if the information is ready, after building the system for the simulation, PSCAD or EMTP may not be able to obtain results because of the simulation time. Thus, system side equivalent models for transient analysis have to be developed to represent the performance of specific aspects of the system. However, these equivalent systems are also based on the detailed system data.

In order to address this problem, a frequency domain impedance matrix based offshore wind farm transient study is presented in this chapter. The goal of this method is to find a mathematic process for determining how DFIG-based offshore wind farm affects system switching transient. Frequency domain impedance modeling for the DFIG is critical for this research. Unlike the studies conducted in time domain simulation, a frequency domain impedance model is developed for Type 3 wind farm in DQ reference frame by transforming the machine control at DQ reference. The converter and control are also included in the impedance model. The nonlinear system is linearized by modeling the machine and control at DQ reference frequency. Decoupled at the rotor and stator side at the same time, quantities are difficult to be control separately so it is not easy to derive the explicit expression for impedance model. The feed forward decoupled controllers are implemented both at the grid side converter control and the machine side converter control. The DFIG transfer function is derived after applying the two controllers. The equivalent frequency domain matrix for the DFIG is tested both under the steady state and transient scenarios with the results being compared with the same scenarios in PSCAD.

Researches focusing on the modeling of the impedance model for the DFIG are applied in papers [61][62][63] for Sub-synchronous Resonance (SSR), the induction machine impedance model being derived in the *dq-axis*. However, the control and PWM are not derived but rather expressed in equivalent circuits. In the paper [64], the small signal method is applied to derive the impedance matrix of the DFIG.

The first part of this chapter discusses the derivation of the DFIG model in the frequency domain. It is divided into two parts since DFIG has two PWM converters, one at the grid side and one at the rotor side. After the derivation, both parts of the impedance matrix are combined as the steady state and transient response of the frequency domain DFIG model and are verified with the PSCAD results. Conclusions are given based on the simulation results.

In this part of the dissertation, the following notations are used in the equations for the stator and rotor circuits:

V_{as},V_{bs},V_{cs}	instantaneous stator phase to neutral voltages
i_{as},i_{bs},i_{cs}	instantaneous stator current in phase a,b,c
V_{ar},V_{br},V_{cr}	instantaneous rotor phase to neutral voltages
i_{ar},i_{br},i_{cr}	instantaneous rotor current in phase a, b, c
R_r, R_s	rotor winding resistance and armature resistance per phase
λ_{sa}, λ_{sb}, λ_{sc}	stator winding flux
λ_{ra}, λ_{rb}, λ_{rc}	rotor winding flux
L_{AA}, L_{BB}, L_{CC}	self-inductance of stator windings
L_{AB}, L_{BA}, L_{BC}, L_{CB}, L_{AC}, L_{CA}	mutual inductance between stator windings
L_{aa}, L_{bb}, L_{cc}	self-inductance of rotor windings
L_{ab}, L_{ab}, L_{bc}, L_{cb}, L_{ac}, L_{ca}	mutual inductance between rotor windings
L_{Aa}, L_{Ab}, L_{Ac}, L_{Ba}, L_{Bc}, L_{Bc} ,L_{Ca}, L_{Cb}, L_{Cc}	mutual inductance between rotor and stator windings
p	differential operator d/dt

5.2 The Approach

A frequency domain DFIG impedance model is imperative in order to apply the frequency domain analysis for determining the switching transient impact on the system. The goal of this approach is to determine the relationship between the output voltages of DFIG V_{abc} and the current from grid converter I_{sabc} and the current from the machine side I_{gabc} as shown in Figure 5.1.

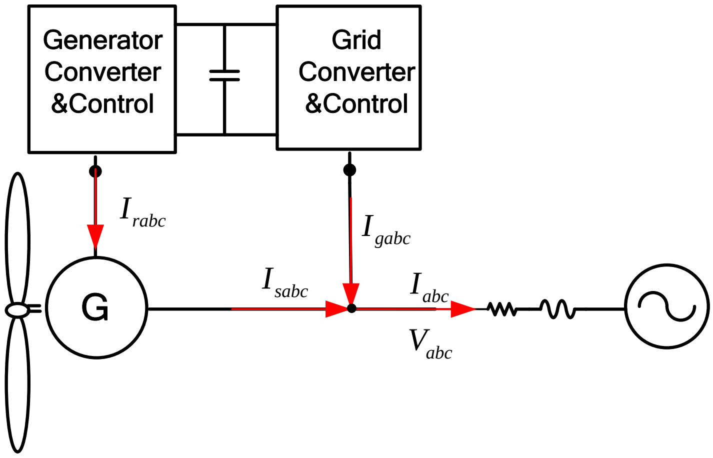

Figure 5.1 Grid side converter and machine side converter

After the derivation of the two impedances at grid side filter Z_{sabc} and machine side Z_{gabc}, the total equivalence impedance of the DFIG can be calculated. After the transfer from the *dq0-axis* to the *abc-axis* using Park transformation, the three-phase impedance matrix for the DFIG is connected to the infinite system bus. For the model verification, the same capacity DFIG in the PSCAD model is tested as shown in Figure 5.2. The fault is placed at a specified time to test the transient response of both models; these results are given in the last section of this chapter.

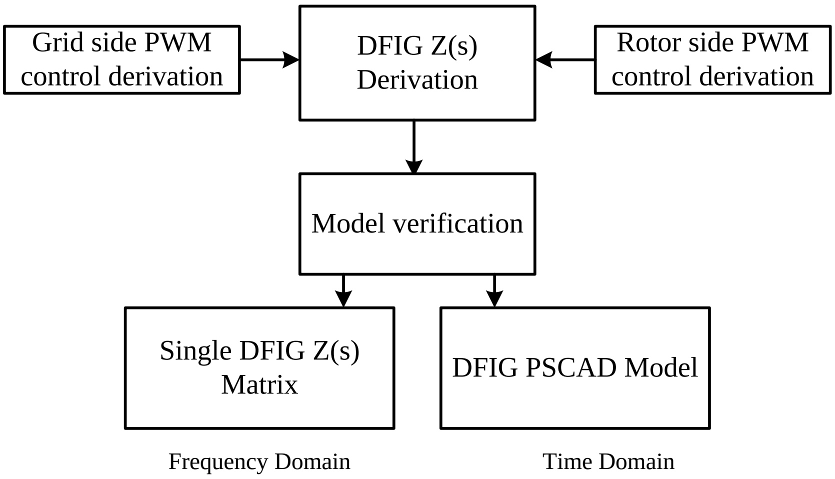

Figure 5.2 Algorithm of Z_{bus} derivation

5.3 The Derivation of the Induction Generator

This section explains the Doubly Fed Induction Generator (DFIG) frequency domain impedance derivation. During electromagnetic transient, it is assumed that the rotor speed remains constant. The rotor and stator windings are identical sinusoidal distributed windings, displaced by resistance R_s and R_r. The positive direction of the magnetic axis of each winding is shown in Figure 5.3, and the equivalent circuit for the rotor and stator winding are shown in Figure 5.4.

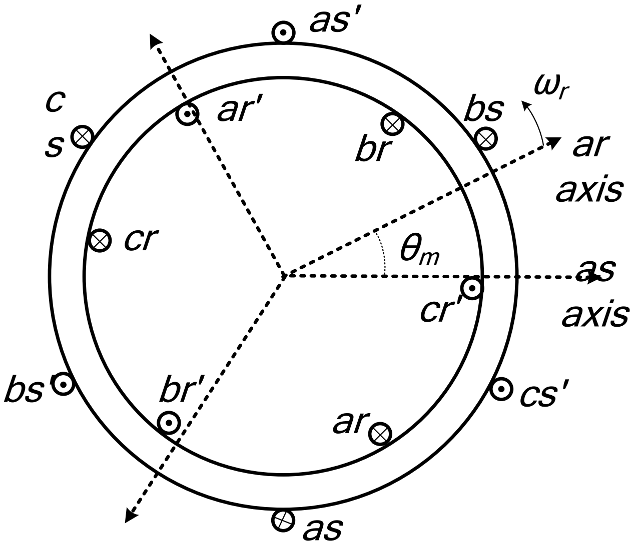

Figure 5.3 Machine windings

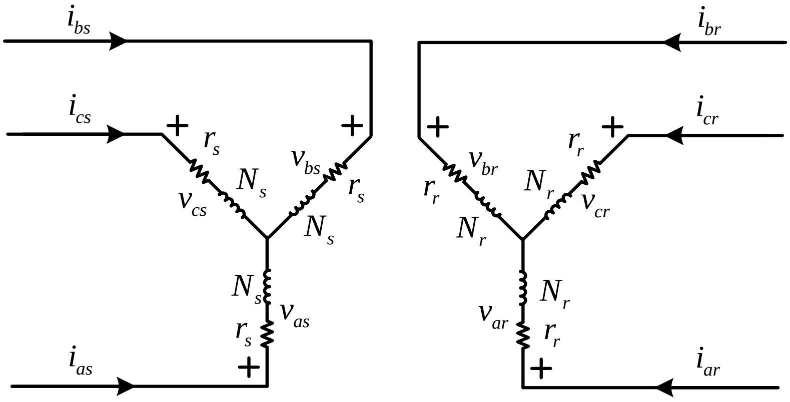

Figure 5.4 Equivalent circuits for rotor and stator winding

5.3.1 Machine Park Transformation

The voltage at the three-phase stator and rotor winding in the induction machine on the *abc* axis is expressed in Equation (5-1) below, and the relationship of the flux linkage in different windings, in Equation (5-2).

$$\begin{bmatrix} V_{as} \\ V_{bs} \\ V_{cs} \\ V_{ar} \\ V_{br} \\ V_{cr} \end{bmatrix} = \begin{bmatrix} R_s & 0 & 0 & 0 & 0 & 0 \\ 0 & R_s & 0 & 0 & 0 & 0 \\ 0 & 0 & R_s & 0 & 0 & 0 \\ 0 & 0 & 0 & R_r & 0 & 0 \\ 0 & 0 & 0 & 0 & R_r & 0 \\ 0 & 0 & 0 & 0 & 0 & R_r \end{bmatrix} \begin{bmatrix} i_{as} \\ i_{bs} \\ i_{cs} \\ i_{ar} \\ i_{br} \\ i_{cr} \end{bmatrix} + \frac{d}{dt} \begin{bmatrix} \lambda_{sa} \\ \lambda_{sb} \\ \lambda_{sc} \\ \lambda_{ra} \\ \lambda_{rb} \\ \lambda_{rc} \end{bmatrix} \cdots\cdots\cdots\cdots (5\text{-}1)$$

The flux linkage in different winding at any instant is given by,

$$\begin{bmatrix} \lambda_{sa} \\ \lambda_{sb} \\ \lambda_{sc} \\ \lambda_{ra} \\ \lambda_{rb} \\ \lambda_{rc} \end{bmatrix} = \begin{bmatrix} L_{AA} & L_{AB} & L_{AC} & L_{Aa} & L_{Ab} & L_{Ac} \\ L_{BA} & L_{BB} & L_{BC} & L_{Ba} & L_{Bb} & L_{Bc} \\ L_{CA} & L_{CB} & L_{CC} & L_{Ca} & L_{Cb} & L_{Cc} \\ L_{aA} & L_{aB} & L_{aC} & L_{aa} & L_{ab} & L_{ac} \\ L_{bA} & L_{bB} & L_{bC} & L_{ba} & L_{bb} & L_{bc} \\ L_{cA} & L_{cB} & L_{cC} & L_{ca} & L_{cb} & L_{cc} \end{bmatrix} \begin{bmatrix} i_{as} \\ i_{bs} \\ i_{cs} \\ i_{ar} \\ i_{br} \\ i_{cr} \end{bmatrix} \cdots\cdots\cdots\cdots (5\text{-}2)$$

It is assumed that all rotor quarantines are transformed to stator side based on the winding ratio according in the Equations (5-3). To simplify the expression of notation, in the rest of this dissertation, the variables at the rotor side are all assumed to have been transferred to the stator side.

$$\begin{cases} V_r' = \dfrac{N_s}{N_r} V_r \\ I_r' = \dfrac{N_r}{N_s} I_r \\ R_r' = \dfrac{N_s^2}{N_r^2} R_r \end{cases} \cdots\cdots\cdots\cdots\cdots\cdots (5\text{-}3)$$

For the matrix format, the voltage and flux equations of the induction machine expressed as both $\mathbf{r}_\mathbf{s}$ and $\mathbf{r}_\mathbf{r}$ are diagonal matrices; the inductance matrix can be expressed as seen in Equations (5-4) to (5-10).

$$\begin{cases} \mathbf{v}_{abcs} = \mathbf{r}_s \mathbf{i}_{abcs} + p\boldsymbol{\lambda}_{abcs} \\ \mathbf{v}_{abcr} = \mathbf{r}_r \mathbf{i}_{abcr} + p\boldsymbol{\lambda}_{abcr} \end{cases} \tag{5-4}$$

$$\begin{cases} \boldsymbol{\lambda}_{abcs} = \mathbf{L}_s \mathbf{i}_{abcs} + \mathbf{L}_{sr} \mathbf{i}_{abcr} \\ \boldsymbol{\lambda}_{abcr} = \left(\mathbf{L}_{sr}\right)^T \mathbf{i}_{abcs} + \mathbf{L}_r \mathbf{i}_{abcr} \end{cases} \tag{5-5}$$

$$\mathbf{L}_s = \begin{bmatrix} L_{ls} + L_{ms} & -\frac{1}{2}L_{ms} & -\frac{1}{2}L_{ms} \\ -\frac{1}{2}L_{ms} & L_{ls} + L_{ms} & -\frac{1}{2}L_{ms} \\ -\frac{1}{2}L_{ms} & -\frac{1}{2}L_{ms} & L_{ls} + L_{ms} \end{bmatrix} \tag{5-6}$$

$$\mathbf{L}_r = \begin{bmatrix} L_{lr} + L_{mr} & -\frac{1}{2}L_{mr} & -\frac{1}{2}L_{mr} \\ -\frac{1}{2}L_{mr} & L_{lr} + L_{mr} & -\frac{1}{2}L_{mr} \\ -\frac{1}{2}L_{mr} & -\frac{1}{2}L_{mr} & L_{lr} + L_{mr} \end{bmatrix} \tag{5-7}$$

$$\mathbf{L}_{sr} = L_{ms} \begin{bmatrix} \cos\theta_r & \cos\left(\theta_r + \frac{2\pi}{3}\right) & \cos\left(\theta_r - \frac{2\pi}{3}\right) \\ \cos\left(\theta_r - \frac{2\pi}{3}\right) & \cos\left(\theta_r\right) & \cos\left(\theta_r + \frac{2\pi}{3}\right) \\ \cos\left(\theta_r + \frac{2\pi}{3}\right) & \cos\left(\theta_r - \frac{2\pi}{3}\right) & \cos\left(\theta_r\right) \end{bmatrix} \tag{5-8}$$

$$\mathbf{L}_{rs} = L_{ms} \begin{bmatrix} \cos\theta_r & \cos\left(\theta_r - \frac{2\pi}{3}\right) & \cos\left(\theta_r + \frac{2\pi}{3}\right) \\ \cos\left(\theta_r + \frac{2\pi}{3}\right) & \cos\left(\theta_r\right) & \cos\left(\theta_r - \frac{2\pi}{3}\right) \\ \cos\left(\theta_r - \frac{2\pi}{3}\right) & \cos\left(\theta_r + \frac{2\pi}{3}\right) & \cos\left(\theta_r\right) \end{bmatrix} = \mathbf{L}_{sr}^T \tag{5-9}$$

where the mural reluctance is expressed as,

$$\begin{cases} L_{AA} = L_{BB} = L_{CC} = L_{ms} + L_{ls} \\ L_{aa} = L_{bb} = L_{cc} = L_{mr} + L_{lr} \\ L_{ms} = L_{mr} \\ L_{AB} = L_{BC} = L_{CA} = L_{ms} \cos\left(\dfrac{2\pi}{3}\right) = -\dfrac{1}{2} L_{ms} \\ L_{ab} = L_{bc} = L_{ca} = L_{mr} \cos\left(\dfrac{2\pi}{3}\right) = -\dfrac{1}{2} L_{mr} \\ L_{Aa} = L_{aA} = L_{Bb} = L_{bB} = L_{Cc} = L_{cC} = L_{ms} \cos\left(\theta_r\right) \\ L_{Ab} = L_{bA} = L_{Bc} = L_{cB} = L_{Ca} = L_{aC} = L_{ms} \cos\left(\theta_r + \dfrac{2\pi}{3}\right) \\ L_{Ac} = L_{cA} = L_{Ba} = L_{aB} = L_{Cb} = L_{bC} = L_{ms} \cos\left(\theta_r - \dfrac{2\pi}{3}\right) \end{cases} \cdots\cdots\cdots\cdots(5\text{-}10)$$

The transformation of both the rotor variables and stator variables from the *abc* axis to the *dq0* axis is shown in the equations below. It is assumed that the *dq0* axis rotates at synchronous speed.

$$\begin{bmatrix} i_q \\ i_d \\ i_0 \end{bmatrix} = \frac{2}{3} \begin{bmatrix} \cos\theta & \cos\left(\theta - \dfrac{2\pi}{3}\right) & \cos\left(\theta + \dfrac{2\pi}{3}\right) \\ \sin\theta & \sin\left(\theta - \dfrac{2\pi}{3}\right) & \sin\left(\theta + \dfrac{2\pi}{3}\right) \\ \dfrac{1}{2} & \dfrac{1}{2} & \dfrac{1}{2} \end{bmatrix} \begin{bmatrix} i_a \\ i_b \\ i_c \end{bmatrix} \cdots\cdots\cdots\cdots(5\text{-}11)$$

$$\mathbf{K}_s = \frac{2}{3} \begin{bmatrix} \cos\theta & \cos\left(\theta - \dfrac{2\pi}{3}\right) & \cos\left(\theta + \dfrac{2\pi}{3}\right) \\ \sin\theta & \sin\left(\theta - \dfrac{2\pi}{3}\right) & \sin\left(\theta + \dfrac{2\pi}{3}\right) \\ \dfrac{1}{2} & \dfrac{1}{2} & \dfrac{1}{2} \end{bmatrix} \cdots\cdots\cdots\cdots(5\text{-}12)$$

$$\mathbf{K}_r = \frac{2}{3} \begin{bmatrix} \cos\theta_r & \cos\left(\theta_r - \dfrac{2\pi}{3}\right) & \cos\left(\theta_r - \dfrac{2\pi}{3}\right) \\ \sin\theta_r & \sin\left(\theta_r - \dfrac{2\pi}{3}\right) & \sin\left(\theta_r - \dfrac{2\pi}{3}\right) \\ \dfrac{1}{2} & \dfrac{1}{2} & \dfrac{1}{2} \end{bmatrix} \cdots\cdots\cdots\cdots(5\text{-}13)$$

The stator magnetic torque position can be found using Equation (5-14), and the rotor position, from Equation (5-15).

$$\theta = \int_0^t \omega d\gamma + \theta(0) \quad \cdots\cdots (5\text{-}14)$$

$$\theta_r = \int_0^t \underbrace{(\omega - \omega_r)}_{\omega_{slip}} d\gamma + \underbrace{\theta(0) - \theta_r(0)}_{\beta(0)} \quad \cdots\cdots (5\text{-}15)$$

where,

ω is the synchronous speed;

θ is the stator position;

$\theta(0)$ is the stator magnetic initial position;

ω_r is the rotor speed;

θ_r is the rotor position;

$\theta_r(0)$ is the stator and rotor initial position;

$\omega - \omega_r = \omega_{slip}$ is the rotor slip;

The inverse Park transformation matrix is given by,

$$\begin{bmatrix} i_a \\ i_b \\ i_c \end{bmatrix} = \begin{bmatrix} \cos\theta & \sin\theta & 1 \\ \cos\left(\theta - \frac{2\pi}{3}\right) & \sin\left(\theta - \frac{2\pi}{3}\right) & 1 \\ \cos\left(\theta + \frac{2\pi}{3}\right) & \sin\left(\theta + \frac{2\pi}{3}\right) & 1 \end{bmatrix} \begin{bmatrix} i_q \\ i_d \\ i_0 \end{bmatrix} \quad \cdots\cdots (5\text{-}16)$$

$$\mathbf{K}_s^{-1}=\begin{bmatrix}\cos\theta & \sin\theta & 1\\ \cos\left(\theta-\frac{2\pi}{3}\right) & \sin\left(\theta-\frac{2\pi}{3}\right) & 1\\ \cos\left(\theta+\frac{2\pi}{3}\right) & \sin\left(\theta+\frac{2\pi}{3}\right) & 1\end{bmatrix}\cdots\cdots(5\text{-}17)$$

$$\mathbf{K}_r^{-1}=\begin{bmatrix}\cos\beta & \sin\beta & 1\\ \cos\left(\beta-\frac{2\pi}{3}\right) & \sin\left(\beta-\frac{2\pi}{3}\right) & 1\\ \cos\left(\beta+\frac{2\pi}{3}\right) & \sin\left(\beta+\frac{2\pi}{3}\right) & 1\end{bmatrix}\cdots\cdots(5\text{-}18)$$

After multiplying the Park transformation matrix K_s and K_r with three-phases flux linkage and the voltage both at the rotor and stator side, they are transformed from the *abc* axis to *dq0* components. The derivations can be expressed in matrix expressions as shown in Equation (5-19) to (5-25).

$$\begin{bmatrix}\mathbf{V}_{abcs}\\ \mathbf{V}_{abcr}\end{bmatrix}=\begin{bmatrix}\mathbf{R_s} & \mathbf{0}\\ \mathbf{0} & \mathbf{R_r}\end{bmatrix}\begin{bmatrix}\mathbf{i}_{abcs}\\ \mathbf{i}_{abcr}\end{bmatrix}+\begin{bmatrix}p\boldsymbol{\lambda}_{abcs}\\ p\boldsymbol{\lambda}_{abcr}\end{bmatrix}\cdots\cdots(5\text{-}19)$$

$$\begin{bmatrix}\mathbf{V}_{qd0s}\\ \mathbf{V}_{qdor}\end{bmatrix}=\begin{bmatrix}\mathbf{K}_s\mathbf{R}_s\mathbf{K}_s^{-1} & \mathbf{0}\\ \mathbf{0} & \mathbf{K}_r\mathbf{R}_r\mathbf{K}_r^{-1}\end{bmatrix}\begin{bmatrix}\mathbf{i}_{qd0s}\\ \mathbf{i}_{qd0r}\end{bmatrix}+\begin{bmatrix}\mathbf{K}_s\, p\boldsymbol{\lambda}_{abcs}\\ \mathbf{K}_r\, p\boldsymbol{\lambda}_{abcr}\end{bmatrix}\cdots\cdots(5\text{-}20)$$

$$\begin{bmatrix}\mathbf{V}_{qd0s}\\ \mathbf{V}_{qdor}\end{bmatrix}=\begin{bmatrix}\mathbf{R}_s & \mathbf{0}\\ \mathbf{0} & \mathbf{R}_r\end{bmatrix}\begin{bmatrix}\mathbf{i}_{qd0s}\\ \mathbf{i}_{qd0r}\end{bmatrix}+\begin{bmatrix}\mathbf{K}_s\, p\left(\mathbf{K}_s^{-1}\boldsymbol{\lambda}_{dq0s}\right)\\ \mathbf{K}_r\, p\left(\mathbf{K}_r^{-1}\boldsymbol{\lambda}_{dq0r}\right)\end{bmatrix}\cdots\cdots(5\text{-}21)$$

$$\begin{bmatrix}\mathbf{V}_{qd0s}\\ \mathbf{V}_{qdor}\end{bmatrix}=\begin{bmatrix}\mathbf{R}_s & \mathbf{0}\\ \mathbf{0} & \mathbf{R}_r\end{bmatrix}\begin{bmatrix}\mathbf{i}_{qd0s}\\ \mathbf{i}_{qd0r}\end{bmatrix}+\begin{bmatrix}p\boldsymbol{\lambda}_{qd0s}\\ p\boldsymbol{\lambda}_{qd0r}\end{bmatrix}+\begin{bmatrix}\mathbf{K}_s\, p\mathbf{K}_s^{-1}\boldsymbol{\lambda}_{qd0s}\\ \mathbf{K}_r\, p\mathbf{K}_r^{-1}\boldsymbol{\lambda}_{qd0r}\end{bmatrix}\cdots\cdots(5\text{-}22)$$

$$\mathbf{K}_s p\mathbf{K}_s^{-1} = \begin{bmatrix} 0 & -\omega & 0 \\ \omega & 0 & 0 \\ 0 & 0 & 0 \end{bmatrix} \cdots\cdots(5\text{-}23)$$

$$\mathbf{K}_r p\mathbf{K}_r^{-1} = \begin{bmatrix} 0 & -(\omega-\omega_m) & 0 \\ \omega-\omega_m & 0 & 0 \\ 0 & 0 & 0 \end{bmatrix} \cdots\cdots(5\text{-}24)$$

Thus, the expression of the voltage on the *dq0* axis is,

$$\begin{cases} V_{ds} = R_s i_{ds} + p\lambda_{ds} - \omega\lambda_{qs} \\ V_{qs} = R_s i_{qs} + p\lambda_{qs} + \omega\lambda_{ds} \\ V_{dr} = R_r i_{dr} + p\lambda_{dr} - \omega_{slip}\lambda_{qr} \\ V_{qr} = R_s i_{qr} + p\lambda_{qr} + \omega_{slip}\lambda_{dr} \end{cases} \cdots\cdots(5\text{-}25)$$

Equations (5-25) represent the voltage equation expressed by the flux linkage.

$$\frac{3}{2}L_m = L_M \cdots\cdots(5\text{-}26)$$

$$\begin{bmatrix} \boldsymbol{\lambda}_{qd0s} \\ \boldsymbol{\lambda}_{qd0r} \end{bmatrix} = \begin{bmatrix} \mathbf{K}_s & 0 \\ 0 & \mathbf{K}_r \end{bmatrix} \begin{bmatrix} \boldsymbol{\lambda}_{abcs} \\ \boldsymbol{\lambda}_{abcr} \end{bmatrix} \cdots\cdots(5\text{-}27)$$

$$\begin{bmatrix} \boldsymbol{\lambda}_{abcs} \\ \boldsymbol{\lambda}_{abcr} \end{bmatrix} = \begin{bmatrix} \mathbf{L}_s & \mathbf{L}_{sr} \\ \mathbf{L}_{rs} & \mathbf{L}_r \end{bmatrix} \begin{bmatrix} \mathbf{i}_{abcs} \\ \mathbf{i}_{abcr} \end{bmatrix} \cdots\cdots(5\text{-}28)$$

$$\begin{bmatrix} \mathbf{i}_{abcs} \\ \mathbf{i}_{abcr} \end{bmatrix} = \begin{bmatrix} \mathbf{K}_s^{-1} & 0 \\ 0 & \mathbf{K}_r^{-1} \end{bmatrix} \begin{bmatrix} \mathbf{i}_{qd0s} \\ \mathbf{i}_{qd0r} \end{bmatrix} \cdots\cdots(5\text{-}29)$$

$$\begin{bmatrix} \boldsymbol{\lambda}_{abcs} \\ \boldsymbol{\lambda}_{abcr} \end{bmatrix} = \begin{bmatrix} \mathbf{L}_s & \mathbf{L}_{sr} \\ \mathbf{L}_{rs} & \mathbf{L}_r \end{bmatrix} \begin{bmatrix} \mathbf{K}_s^{-1} & 0 \\ 0 & \mathbf{K}_r^{-1} \end{bmatrix} \begin{bmatrix} \mathbf{i}_{qd0s} \\ \mathbf{i}_{qd0r} \end{bmatrix} \cdots\cdots(5\text{-}30)$$

$$\begin{bmatrix} \boldsymbol{\lambda}_{qd0s} \\ \boldsymbol{\lambda}_{qd0r} \end{bmatrix} = \begin{bmatrix} \mathbf{K}_s & 0 \\ 0 & \mathbf{K}_r \end{bmatrix} \begin{bmatrix} \mathbf{L}_s & \mathbf{L}_{sr} \\ \mathbf{L}_{rs} & \mathbf{L}_r \end{bmatrix} \begin{bmatrix} \mathbf{K}_s^{-1} & 0 \\ 0 & \mathbf{K}_r^{-1} \end{bmatrix} \begin{bmatrix} \mathbf{i}_{qd0s} \\ \mathbf{i}_{qd0r} \end{bmatrix} \cdots\cdots(5\text{-}31)$$

$$\begin{bmatrix}\boldsymbol{\lambda}_{qd0s}\\ \boldsymbol{\lambda}_{qd0r}\end{bmatrix}=\begin{bmatrix}\mathbf{K}_s\mathbf{L}_s\mathbf{K}_s^{-1} & \mathbf{K}_s\mathbf{L}_{sr}\mathbf{K}_r^{-1}\\ \mathbf{K}_r\mathbf{L}_{rs}\mathbf{K}_s^{-1} & \mathbf{K}_r\mathbf{L}_r\mathbf{K}_r^{-1}\end{bmatrix}\begin{bmatrix}\mathbf{i}_{qd0s}\\ \mathbf{i}_{qd0r}\end{bmatrix}\quad\cdots\cdots\cdots\cdots\cdots\cdots\tag{5-32}$$

$$\begin{bmatrix}\lambda_{qs}\\ \lambda_{ds}\\ \lambda_{0s}\\ \lambda_{qr}\\ \lambda_{dr}\\ \lambda_{0r}\end{bmatrix}=\begin{bmatrix}L_{ls}+L_M & 0 & 0 & L_M & 0 & 0\\ 0 & L_{ls}+L_M & 0 & 0 & L_M & 0\\ 0 & 0 & L_{ls} & 0 & 0 & 0\\ L_M & 0 & 0 & L_{lr}+L_M & 0 & 0\\ 0 & L_M & 0 & 0 & L_{lr}+L_M & 0\\ 0 & 0 & 0 & 0 & 0 & L_{lr}\end{bmatrix}\begin{bmatrix}i_{qs}\\ i_{ds}\\ i_{0s}\\ i_{qr}\\ i_{dr}\\ i_{0r}\end{bmatrix}\tag{5-33}$$

$$\mathbf{K}_s\mathbf{L}_s\mathbf{K}_s^{-1}=\begin{bmatrix}L_{ls}+L_M & 0 & 0\\ 0 & L_{ls}+L_M & 0\\ 0 & 0 & L_{ls}\end{bmatrix}\equiv\mathbf{L}_{sqd0}\quad\cdots\cdots\cdots\cdots\cdots\tag{5-34}$$

$$\mathbf{K}_s\mathbf{L}_{sr}\mathbf{K}_r^{-1}=\mathbf{K}_r\mathbf{L}_{rs}\mathbf{K}_s^{-1}=\begin{bmatrix}L_M & 0 & 0\\ 0 & L_M & 0\\ 0 & 0 & 0\end{bmatrix}\equiv\mathbf{L}_{mqd0}\quad\cdots\cdots\cdots\cdots\tag{5-35}$$

$$\mathbf{K}_r\mathbf{L}_r\mathbf{K}_r^{-1}=\begin{bmatrix}L_{lr}+L_M & 0 & 0\\ 0 & L_{lr}+L_M & 0\\ 0 & 0 & L_{lr}\end{bmatrix}\equiv\mathbf{L}_{rqd0}\quad\cdots\cdots\cdots\cdots\cdots\tag{5-36}$$

$$\begin{bmatrix}\mathbf{V}_{qd0s}\\ \mathbf{V}_{qdor}\end{bmatrix}=\begin{bmatrix}\mathbf{R}_s & \mathbf{0}\\ \mathbf{0} & \mathbf{R}_r\end{bmatrix}\begin{bmatrix}\mathbf{i}_{qd0s}\\ \mathbf{i}_{qd0r}\end{bmatrix}+\begin{bmatrix}p\boldsymbol{\lambda}_{qd0s}\\ p\boldsymbol{\lambda}_{qd0r}\end{bmatrix}+\begin{bmatrix}\mathbf{K}_s\,p\mathbf{K}_s^{-1}\boldsymbol{\lambda}_{qd0s}\\ \mathbf{K}_r\,p\mathbf{K}_r^{-1}\boldsymbol{\lambda}_{qd0r}\end{bmatrix}\quad\cdots\cdots\tag{5-37}$$

$$\begin{bmatrix}\mathbf{V}_{qd0s}\\ \mathbf{V}_{qdor}\end{bmatrix}=\begin{bmatrix}\mathbf{R}_s & \mathbf{0}\\ \mathbf{0} & \mathbf{R}_r\end{bmatrix}\begin{bmatrix}\mathbf{i}_{qd0s}\\ \mathbf{i}_{qd0r}\end{bmatrix}+\begin{bmatrix}\mathbf{L}_{sqd0} & \mathbf{L}_{mqd0}\\ \mathbf{L}_{mqd0} & \mathbf{L}_{rqd0}\end{bmatrix}\begin{bmatrix}p\mathbf{i}_{qd0s}\\ p\mathbf{i}_{qd0r}\end{bmatrix}+\begin{bmatrix}\mathbf{K}_s\,p\mathbf{K}_s^{-1}\boldsymbol{\lambda}_{qd0s}\\ \mathbf{K}_r\,p\mathbf{K}_r^{-1}\boldsymbol{\lambda}_{qd0r}\end{bmatrix}\quad\cdots\tag{5-38}$$

After substituting the flux in the voltage equation with the current, it is derived that,

$$\begin{bmatrix} V_{ds} \\ V_{qs} \\ V_{0s} \\ V_{dr} \\ V_{qr} \\ V_{0r} \end{bmatrix} = \begin{bmatrix} R_s & -\omega L_s & 0 & 0 & -\omega L_M & 0 \\ \omega L_s & R_s & 0 & \omega L_M & 0 & 0 \\ 0 & 0 & R_s & 0 & 0 & 0 \\ 0 & -\omega_{slip} L_M & 0 & R_r & -\omega_{slip} L_r & 0 \\ \omega_{slip} L_M & 0 & 0 & \omega_{slip} L_r & R_r & 0 \\ 0 & 0 & 0 & 0 & 0 & R_r \end{bmatrix} \begin{bmatrix} i_{ds} \\ i_{qs} \\ i_{0s} \\ i_{dr} \\ i_{qr} \\ i_{0r} \end{bmatrix} + \begin{bmatrix} L_s & 0 & 0 & L_M & 0 & 0 \\ 0 & L_s & 0 & 0 & L_M & 0 \\ 0 & 0 & L_{ls} & 0 & 0 & 0 \\ L_M & 0 & 0 & L_r & 0 & 0 \\ 0 & L_M & 0 & 0 & L_r & 0 \\ 0 & 0 & 0 & 0 & 0 & L_{lr} \end{bmatrix} \begin{bmatrix} pi_{ds} \\ pi_{qs} \\ pi_{os} \\ pi_{dr} \\ pi_{qr} \\ pi_{or} \end{bmatrix} \cdots\cdots (5\text{-}39)$$

where the L_s is defined as $L_{ls} + L_M$ and L_r is defined as $L_{lr} + L_M$.

Under balanced conditions, i_0 is zero, indicating no flux is produced. The zero sequence components, which are inherent to the *dq0* model, are independent from the others and do not participate in the electromagnetic power production.

$$V_{0s} = R_s i_{0s} + p\lambda_{0s} \cdots\cdots (5\text{-}40)$$

$$V_{0r} = R_r i_{0r} + p\lambda_{0r} \cdots\cdots (5\text{-}41)$$

$$\lambda_{0r} = L_{lr} i_{0r} \cdots\cdots (5\text{-}42)$$

$$\lambda_{0s} = L_{ls} i_{0s} \cdots\cdots (5\text{-}43)$$

5.3.2 The Stator Flux Oriented Reference Frame

Aligning the *d*-axis along the stator flux vector position derives a decoupled control between the electrical torque and the rotor excitation current [65]139[66] .The stator flux angle is calculated from

$$\lambda_{\alpha s} = \int (V_{\alpha s} - R_s i_{\alpha s}) dt \cdots\cdots (5\text{-}44)$$

$$\lambda_{\beta s} = \int (V_{\beta s} - R_s i_{\beta s}) dt \cdots\cdots (5\text{-}45)$$

$$\theta_s = \tan^{-1} \frac{\lambda_{\beta s}}{\lambda_{\alpha s}} \cdots\cdots (5\text{-}46)$$

$$T_{em} = \frac{3}{2}P\left(\lambda_{ds}i_{qs} - \lambda_{qs}i_{ds}\right) = \frac{3}{2}P\left(\lambda_{qr}i_{dr} - \lambda_{dr}i_{qr}\right) \cdots\cdots\cdots\cdots\cdots\cdots\cdots\cdots (5\text{-}47)$$

$$Q_s = \frac{3}{2}P(V_{ds}i_{qs} - V_{qs}i_{ds}) \cdots\cdots\cdots\cdots\cdots\cdots\cdots\cdots\cdots\cdots\cdots\cdots\cdots\cdots (5\text{-}48)$$

θ_s represents the stator-flux vector position. In this way the electromagnetic torque T_{em} can be directly controlled by the rotor *q-axis* current i_{qr}. The stator reactive power Q_s can be directly controlled by the rotor direct-axis current i_{dr}. In this way, the Torque and reactive power are decoupled.

$$\lambda_s = \lambda_{ds} = L_M i_{ms} = L_s i_{ds} + L_M i_{dr} \Rightarrow i_{ds} = \frac{1}{L_s}\left(L_M i_{ms} - L_M i_{dr}\right) \cdots\cdots\cdots (5\text{-}49)$$

$$\lambda_{qs} = L_s i_{qs} + L_M i_{qr} = 0 \Rightarrow i_{qs} = -\frac{L_M}{L_s} i_{qr} \cdots\cdots\cdots\cdots\cdots\cdots\cdots\cdots\cdots\cdots (5\text{-}50)$$

$$\lambda_{dr} = (i_{ds} + i_{dr}) = \frac{L_M}{L_s}\left(L_M i_{ms} - L_M i_{dr}\right) + L_r i_{dr} \cdots\cdots\cdots\cdots\cdots\cdots\cdots\cdots\cdots\cdots\cdots (5\text{-}51)$$

$$\lambda_{qr} = L_M i_{qs} + L_r i_{qr} = -\frac{L_M^2}{L_s} i_{qr} + L_r i_{qr} \cdots\cdots\cdots\cdots\cdots\cdots\cdots\cdots\cdots\cdots\cdots\cdots\cdots (5\text{-}52)$$

Since the stator is connected to the grid and the influence of the stator resistance is small, the stator magnetizing current i_{ms} can be considered constant. Under stator-flux orientation reference, the voltage and the torque at the *dq* axis can be written as below, where *P* represents the number of poles.

$$\begin{cases} V_{ds} = R_s i_{ds} \\ V_{qs} = R_s i_{qs} + \omega\left(L_s i_{ds} + L_M i_{dr}\right) \\ V_{dr} = R_r i_{dr} + p\left(L_r - \dfrac{L_M^2}{L_s}\right) i_{dr} - \omega_{slip}\left(L_r - \dfrac{L_M^2}{L_s}\right) i_{qr} \\ V_{qr} = R_r i_{qr} + p\left(L_r - \dfrac{L_M^2}{L_s}\right) i_{qr} + \omega_{slip}\dfrac{L_M^2}{L_s} i_{ms} + \omega_{slip}\left(L_r - \dfrac{L_M^2}{L_s}\right) i_{dr} \end{cases} \cdots\cdots\cdots\cdots\cdots\cdots (5\text{-}53)$$

$$\begin{bmatrix} V_{ds} \\ V_{qs} \\ V_{dr} \\ V_{qr} \end{bmatrix} = \begin{bmatrix} R_s & 0 & 0 & 0 \\ \omega L_s & R_s & \omega L_M & 0 \\ 0 & 0 & R_r & -\sigma\omega_{slip} L_r \\ 0 & 0 & \sigma\omega_{slip} L_r & R_r \end{bmatrix} \begin{bmatrix} i_{ds} \\ i_{qs} \\ i_{dr} \\ i_{qr} \end{bmatrix} + \begin{bmatrix} 0 & 0 & 0 & 0 \\ 0 & 0 & 0 & 0 \\ 0 & 0 & \sigma L_r & 0 \\ 0 & 0 & 0 & \sigma L_r \end{bmatrix} \begin{bmatrix} pi_{ds} \\ pi_{qs} \\ pi_{dr} \\ pi_{qr} \end{bmatrix} + \begin{bmatrix} 0 \\ 0 \\ 0 \\ \omega_{slip} L_M i_{ms} \end{bmatrix} \cdots(5\text{-}54)$$

$$T_e = -\frac{3P}{2} L_m i_{ms} i_{qr} \cdots\cdots(5\text{-}55)$$

$$\omega_{slip} = \omega - \omega_r \cdots\cdots(5\text{-}56)$$

$$\sigma = 1 - \frac{L_M^2}{L_s L_r} \cdots\cdots(5\text{-}57)$$

For stator side quantities,

$$\begin{bmatrix} V_{ds} \\ V_{qs} \end{bmatrix} = \begin{bmatrix} R_s & 0 \\ \omega L_s & R_s \end{bmatrix} \begin{bmatrix} i_{ds} \\ i_{qs} \end{bmatrix} + \begin{bmatrix} 0 & 0 \\ \omega L_M & 0 \end{bmatrix} \begin{bmatrix} i_{dr} \\ i_{qr} \end{bmatrix} \cdots\cdots(5\text{-}58)$$

$$\mathbf{A} = \begin{bmatrix} R_s & 0 \\ \omega L_s & R_s \end{bmatrix} \cdots\cdots(5\text{-}59)$$

$$\mathbf{B} = \begin{bmatrix} 0 & 0 \\ \omega L_M & 0 \end{bmatrix} \cdots\cdots(5\text{-}60)$$

$$\begin{bmatrix} V_{ds} \\ V_{qs} \end{bmatrix} = \mathbf{A} \begin{bmatrix} i_{ds} \\ i_{qs} \end{bmatrix} + \mathbf{B} \begin{bmatrix} i_{dr} \\ i_{qr} \end{bmatrix} \cdots\cdots(5\text{-}61)$$

For rotor side quantities,

$$\begin{bmatrix} V_{dr} \\ V_{qr} \end{bmatrix} = \begin{bmatrix} R_r + pL_r & -\omega_{slip}\sigma L_r \\ \omega_{slip}\sigma L_r & R_r + p\sigma L_r \end{bmatrix} \begin{bmatrix} i_{dr} \\ i_{qr} \end{bmatrix} + \begin{bmatrix} 0 \\ \omega_{slip} L_M i_{ms} \end{bmatrix} \cdots\cdots(5\text{-}62)$$

$$\mathbf{C} = \begin{bmatrix} R_r + pL_r & -\omega_{slip}\sigma L_r \\ \omega_{slip} L_r & R_r + p\sigma L_r \end{bmatrix} \cdots\cdots(5\text{-}63)$$

$$\mathbf{D} = \begin{bmatrix} 0 \\ \omega_{slip} L_m i_{ms} \end{bmatrix} \cdots\cdots(5\text{-}64)$$

$$\begin{bmatrix} V_{dr} \\ V_{qr} \end{bmatrix} = \mathbf{C} \begin{bmatrix} i_{dr} \\ i_{qr} \end{bmatrix} + \mathbf{D} \quad \cdots\cdots(5\text{-}65)$$

Based on the derivation above, the system block diagram can be illustrated in the Figure 5.5.

V'_{dr} and V'_{qr} are defined based on the equations below.

$$V'_{dr} = R_r i_{dr} + L_r \frac{di_{dr}}{dt} \quad \cdots\cdots(5\text{-}66)$$

$$V'_{qr} = R_r i_{qr} + \sigma L_r \frac{di_{qr}}{dt} \quad \cdots\cdots(5\text{-}67)$$

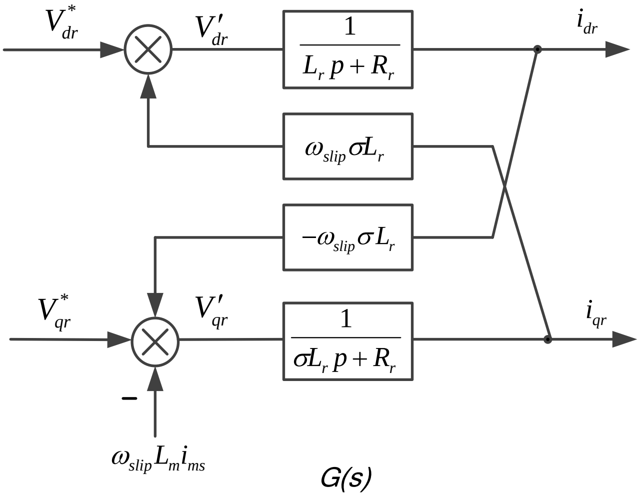

Figure 5.5 The doubly fed induction generator block diagram

The errors of i_{dr} and i_{qr} are tuned by the *PI* controller and sent to V'_{dr} and V'_{qr} respectively. To ensure accurate tracking of these currents, compensation terms are added to V_{dr} and V_{qr} to obtain the reference voltages V^*_{dr} and V^*_{qr} based on the equation below.

$$V_{dr}^{*} = R_r i_{dr} + \sigma L_r \frac{di_{dr}}{dt} - \omega_{slip} \sigma L_r i_{qr} \quad \cdots\cdots (5\text{-}68)$$

$$V_{qr}^{*} = R_r i_{qr} + \sigma L_r \frac{di_{qr}}{dt} + \omega_{slip} \left(L_m i_{ms} + \sigma L_r i_{dr} \right) \quad \cdots\cdots (5\text{-}69)$$

5.3.3 Feed Forward Decouple Control

Figure 5.5 shows that the rotor D axis and Q axis voltage are coupled with the currents at the axis. Voltage equations express the existing coupling relation between two axis current components. The current loop uses two PI regulators in the rotation frame in these approaches. This structure is illustrated in the figure below.

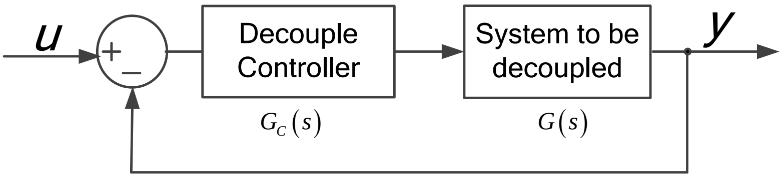

Figure 5.6 Feed forward decoupled controller

Figure 5.7 is the diagram of the entire system including the feed forward controller.

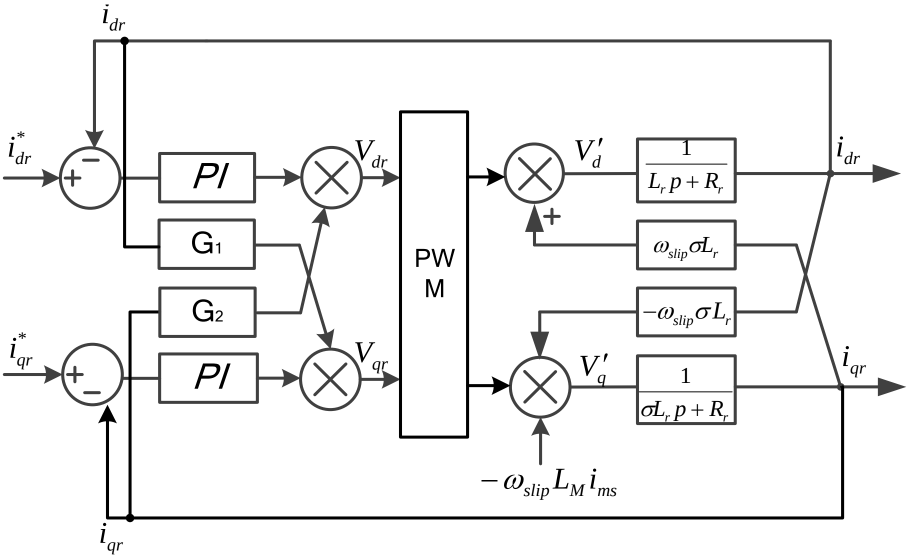

Figure 5.7 DFIG with feed forward decoupled controller

Based on the block diagram, the transfer function can be derived with PWM being expressed in a delay transfer function $\frac{1}{T_s p+1}$ with T_s as the switching frequency.

$$\begin{cases} \left(R_r+\sigma L_r p\right) i_{dr}-\omega_{slip} \sigma L_r i_{qr}=\dfrac{(K_{ipd}+\frac{K_{ild}}{p})(i_{dr}^*-i_{dr})+G_2 i_{qr}}{T_s p+1} \\ \left(R_r+\sigma L_r p\right) i_{qr}+\omega_{slip}(L_M i_{ms}+\sigma L_r i_{dr})=\dfrac{(K_{ipq}+\frac{K_{ilq}}{p})(i_{qr}^*-i_{qr})+G_1 i_{dr}}{T_s p+1} \end{cases} \cdots\cdots\cdots\cdots(5\text{-}70)$$

Specify that,

$$\begin{cases} PI_d=K_{pd}+\dfrac{K_{id}}{p} \\ PI_q=K_{pq}+\dfrac{K_{iq}}{p} \end{cases} \cdots\cdots\cdots\cdots(5\text{-}71)$$

It can be observed that the G_1 and G_2 can be expressed as

$$\begin{cases} G_1=\omega_{slip} \sigma L_r\left(T_s p+1\right) \\ G_2=-\omega_{slip} \sigma L_r\left(T_s p+1\right) \end{cases} \cdots\cdots\cdots\cdots(5\text{-}72)$$

Thus, the feed forward decoupling control is represented as

$$\begin{cases} V_{dr}^*=(K_{ipd}+\dfrac{K_{ild}}{p})(i_{dr}^*-i_{dr})-\omega_{slip} \sigma L_r\left(T_s p+1\right) i_{qr} \\ V_{qr}^*=(K_{ipq}+\dfrac{K_{ilq}}{p})(i_{qr}^*-i_{qr})+\omega_{slip} \sigma L_r\left(T_s p+1\right) i_{dr} \end{cases} \cdots\cdots\cdots\cdots(5\text{-}73)$$

The structure of the feed forward decoupling control can be diagramed as seen in Figure 5.8.

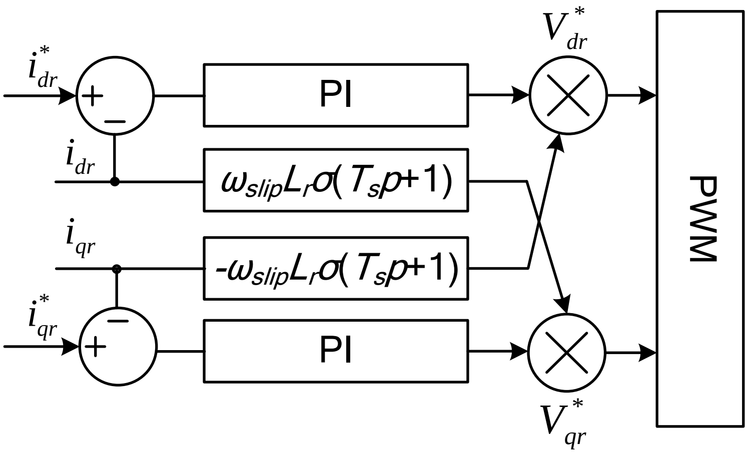

Figure 5.8 Feed forward decouple controller

$$\begin{cases} i_{dr} = \dfrac{PI_d i^*_{dr}}{(R_r + L_r p)(T_s p + 1) + PI_d} \\ i_{qr} = \dfrac{PI_q i^*_{qr} - \omega_{slip} L_M i_{ms}(T_s p + 1)}{(R_r + L_r p)(T_s p + 1) + PI_q} \end{cases} \cdots\cdots\cdots\cdots\cdots\cdots\cdots\cdots\cdots\cdots\cdots\cdots (5\text{-}74)$$

Substituting the rotor current expression into the stator side, the relationship between the voltage and the stator current for the machine and its PWM can be derived using the equations below.

$$\begin{bmatrix} V_{ds} \\ V_{qs} \end{bmatrix} = \begin{bmatrix} R_s & 0 \\ \omega L_s & R_s \end{bmatrix} \begin{bmatrix} i_{ds} \\ i_{qs} \end{bmatrix} + \begin{bmatrix} 0 & 0 \\ \omega L_m & 0 \end{bmatrix} \begin{bmatrix} i_{dr} \\ i_{qr} \end{bmatrix} \cdots\cdots\cdots\cdots\cdots\cdots\cdots\cdots\cdots\cdots (5\text{-}75)$$

$$\begin{bmatrix} V_{ds} \\ V_{qs} \end{bmatrix} = \begin{bmatrix} R_s & 0 \\ \omega L_s & R_s \end{bmatrix} \begin{bmatrix} i_{ds} \\ i_{qs} \end{bmatrix} + \begin{bmatrix} 0 & 0 \\ \omega L_m & 0 \end{bmatrix} \begin{bmatrix} \dfrac{PI_d i^*_{dr}}{(R_r + L_r p)(T_s p + 1) + PI_d} \\ \dfrac{PI_q i^*_{qr} - \omega_{slip} L_M i_{Ms}(T_s p + 1)}{(R_r + L_r p)(T_s p + 1) + PI_q} \end{bmatrix} (5\text{-}76)$$

$$\begin{bmatrix} V_{ds} \\ V_{qs} \end{bmatrix} = \begin{bmatrix} R_s & 0 \\ \omega L_s & R_s \end{bmatrix} \begin{bmatrix} i_{ds} \\ i_{qs} \end{bmatrix} + \begin{bmatrix} 0 \\ \dfrac{\omega L_m PI_d i^*_{dr}}{(R_r + L_r p)(T_s p + 1) + PI_d} \end{bmatrix} \cdots\cdots\cdots\cdots (5\text{-}77)$$

The h_{qr} is defined in the equation below.

$$
\begin{aligned}
h_{qr} &= \frac{\omega L_m PI_d i^*_{dr}}{\left(R_r + L_r p\right)\left(T_s p + 1\right) + PI_d} \\
&= \frac{\omega L_m i^*_{dr} \dfrac{K_{pd} p + K_{id}}{p}}{\left(R_r + L_r p\right)\left(T_s p + 1\right) + \dfrac{K_{pd} p + K_{id}}{p}} \\
&= \frac{\omega L_m i^*_{dr} \left(K_{pd} p + K_{id}\right)}{p\left(R_r + L_r p\right)\left(T_s p + 1\right) + \left(K_{pd} p + K_{id}\right)} \\
&= \frac{\omega L_m i^*_{dr} K_{pd} p + \omega L_m i^*_{dr} K_{id}}{L_r T_s p^3 + \left(R_r T_s + L_r\right) p^2 + \left(R_r + K_{pd}\right) p + K_{id}}
\end{aligned}
\qquad \cdots\cdots\cdots\cdots\cdots\cdots\text{(5-78)}
$$

After applying the feed forward control, the stator voltage and the current relationship of the machine with its PWM control is expressed in the equation below. The impedance model for the machine and its converter control is expressed in the Equation (5-79).

$$
\begin{bmatrix} V_{ds} \\ V_{qs} \end{bmatrix} = \begin{bmatrix} R_s & 0 \\ \omega L_s & R_s \end{bmatrix} \begin{bmatrix} i_{ds} \\ i_{qs} \end{bmatrix} + \begin{bmatrix} 0 \\ h_{qr} \end{bmatrix} \qquad \cdots\cdots\cdots\cdots\cdots\cdots\cdots\cdots\cdots\cdots\cdots\cdots\text{(5-79)}
$$

5.3.4 Grid Side PWM Converter and Control

The grid side converter for the DFIG generator is shown in Figure 5.9. Its purpose is to keep the DC-link voltage constant regardless of the magnitude and direction of the rotor power [65]. Vector-control with a reference frame oriented along the stator voltage vector position is used under the assumption that $V_s=V_{ds}$ and that the P_l and Q_l flowing through the generator-side converter are decoupled. The PWM converter is current regulated, with the *d-axis* current component I_{dl} used to regulate the DC-link voltage (*E*) and the *q-axis* current component I_{ql} used to regulate the reactive power Q_l.

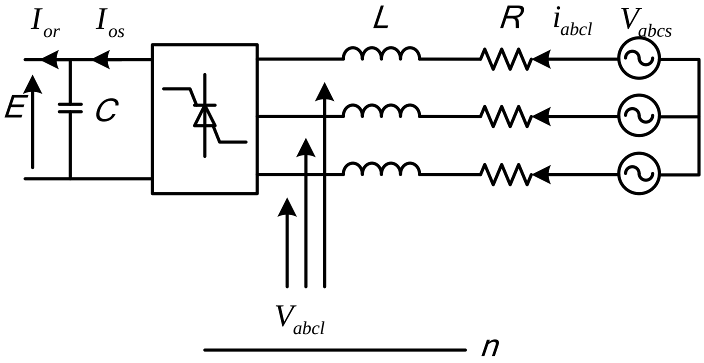

Figure 5.9 DFIG grid side converter

The DFIG grid side converter and the filter are modeled using the equation below.

$$\begin{bmatrix} V_{as} \\ V_{bs} \\ V_{cs} \end{bmatrix} = R \begin{bmatrix} i_{al} \\ i_{bl} \\ i_{cl} \end{bmatrix} + L\frac{d}{dt}\begin{bmatrix} i_{al} \\ i_{bl} \\ i_{cl} \end{bmatrix} + \begin{bmatrix} V_{al} \\ V_{bl} \\ V_{cl} \end{bmatrix} \quad \cdots\cdots\cdots\cdots\cdots\cdots\cdots\cdots\cdots\cdots\cdots\cdots\text{(5-80)}$$

where

L and *R* are the filter inductance and resistance respectively;

V_{as}, V_{bs}, V_{cs} are the output voltage of the DFIG;

i_{al}, i_{bl}, i_{cl}, are the current flowing through the filter;

V_{al}, V_{bl}, V_{cl} are the voltage input for PWM controller;

Using these transformations and aligning the *d*-axis of the reference frame along the stator-voltage V_{ds} position, the voltage relationship with current is expressed below:

$$\begin{cases} V_{ds} = Ri_{dl} + L\dfrac{di_{dl}}{dt} - \omega_e Li_q + V_{dl} \\ V_{qs} = Ri_{ql} + L\dfrac{di_{ql}}{dt} + \omega_e Li_d + V_{ql} \end{cases} \quad \cdots\cdots\cdots\cdots\cdots\cdots\cdots\cdots\cdots\cdots\cdots\cdots\text{(5-81)}$$

The active power and reactive power are expressed in the equation below. By aligning the *d-axis* of the reference frame along the stator-voltage V_{ds} position, the active power and reactive power can be decoupled and controlled separately.

$$P_l = \frac{3}{2}(V_{ds}i_{dl} + V_{qs}i_{ql}) \quad \cdots\cdots (5\text{-}82)$$

$$Q_l = \frac{3}{2}(V_{ds}i_{ql} - V_{qs}i_{dl}) \quad \cdots\cdots (5\text{-}83)$$

By defining the V'_d and V'_q as seen in the equation below, the grid side converter and its system diagram can be illustrated in the Figure 5.10 [67][68][69].

$$\begin{cases} V'_d = Ri_{dl} + L\dfrac{di_{dl}}{dt} \\ V'_q = Ri_{ql} + L\dfrac{di_{ql}}{dt} \end{cases} \quad \cdots\cdots (5\text{-}84)$$

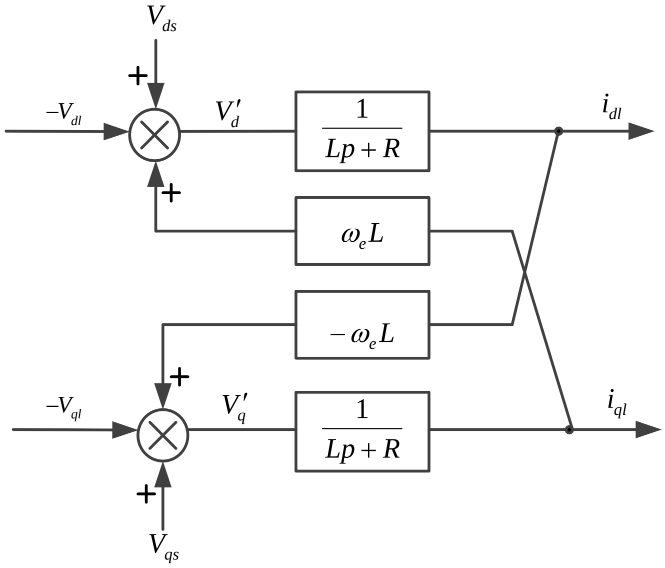

Figure 5.10 DFIG grid side converter block diagram

As this diagram shows, the d-axis and q-axis quantities are coupled. The equations below derive the structure with decoupled control as illustrated below in Figure 5.11.

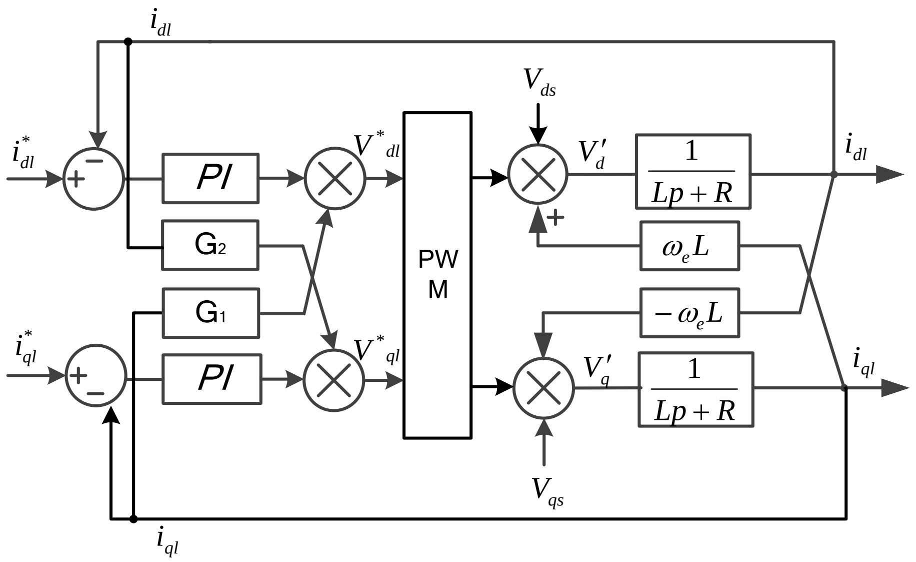

Figure 5.11 Decoupled control scheme for the grid side converter

$$\begin{cases} (R+Lp)i_{dl} - \omega_e L i_{ql} - V_{ds} = -\left[(K_{ipd} + \frac{K_{ild}}{p})(i_{dl}^* - i_{dl}) + G_1 i_{ql} \right] \times \frac{1}{T_s p + 1} \\ (R+Lp)i_{ql} + \omega_e L i_{ql} - V_{qs} = -\left[(K_{ipq} + \frac{K_{ilq}}{p})(i_{ql}^* - i_{ql}) + G_2 i_{dl} \right] \times \frac{1}{T_s p + 1} \end{cases} \quad \cdots\cdots\cdots\cdots\cdots\cdots (5\text{-}85)$$

The equation below defines the PI control.

$$\begin{cases} PI_{dl} = K_{pdl} + \frac{K_{idl}}{p} \\ PI_{ql} = K_{pql} + \frac{K_{iql}}{p} \end{cases} \quad \cdots\cdots\cdots\cdots\cdots\cdots\cdots\cdots\cdots\cdots\cdots\cdots\cdots\cdots\cdots\cdots (5\text{-}86)$$

So the decoupled factor can be derived that as shown below.

$$\begin{cases} G_1 = \omega_e L (T_s p + 1) \\ G_2 = -\omega_e L (T_s p + 1) \end{cases} \quad \cdots\cdots\cdots\cdots\cdots\cdots\cdots\cdots\cdots\cdots\cdots\cdots\cdots\cdots\cdots (5\text{-}87)$$

The feed forward decoupled controller is shown in Figure 5.12.

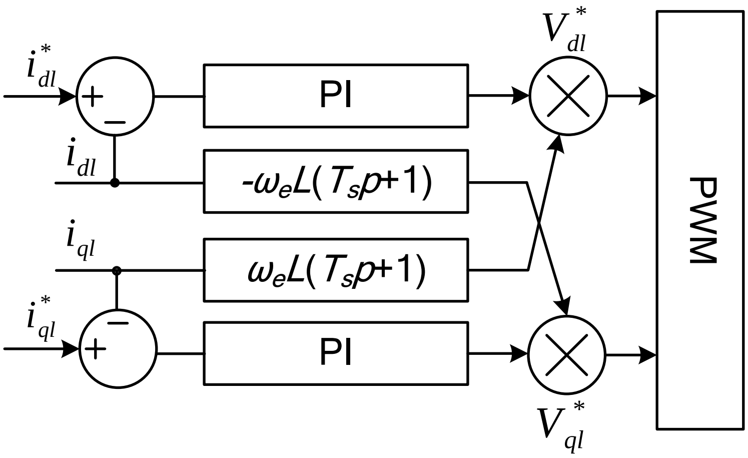

Figure 5.12 Decoupled control

The final transfer function after the decoupling of the feed forward decoupled control is,

$$\begin{cases} V_{ds} = \dfrac{\left[(R+Lp)(T_s p+1)-PI_{dl}\right]}{(T_s p+1)} i_{dl} + \dfrac{PI_{dl}}{(T_s p+1)} i_{dl}^* \\ V_{qs} = \dfrac{\left[(R+Lp)(T_s p+1)-PI_{ql}\right]}{(T_s p+1)} i_{ql} + \dfrac{PI_{ql}}{(T_s p+1)} i_{ql}^* \end{cases} \cdots\cdots\cdots\cdots\cdots\cdots\cdots\cdots\cdots\cdots\cdots (5\text{-}88)$$

The impedance for the grid side converter control and filter of the DFIG can be expressed in matrix format using Equation (5-89).

$$\begin{bmatrix} V_{ds} \\ V_{qs} \end{bmatrix} = \overbrace{\begin{bmatrix} \dfrac{(R+Lp)(T_s p+1)-PI_{dl}}{(T_s p+1)} & 0 \\ 0 & \dfrac{(R+Lp)(T_s p+1)-PI_{ql}}{(T_s p+1)} \end{bmatrix}}^{Z_{\text{Grid Converter}}} \begin{bmatrix} i_{dl} \\ i_{ql} \end{bmatrix} + \overbrace{\begin{bmatrix} \dfrac{PI_{dl}}{(T_s p+1)} i_{dl}^* \\ \dfrac{PI_{ql}}{(T_s p+1)} i_{ql}^* \end{bmatrix}}^{V_{\text{Grid Resource}}} \cdots\cdots\cdots\cdots (5\text{-}89)$$

5.3.5 Combination of the Two Parts

The impedance matrixes for the grid side and the machine side have been derived from Equation (5-79) and Equation (5-89), respectively. However, those two quantities are in reference frames that are oriented different oriented. The machine and the rotor PWM control are aligned with the stator flux oriented reference, while the grid side filter and its PWM control are aligning to the system voltage d-axis reference frame. Before combining, the two impedances have to be converted to the same reference frame through an angle shift. As can be seen from Figure 5.13, the impedance at the grid side converter aligns to *d-axis*, and the impedance at machine side is aligned with the stator flux reference with an angle difference of θ_s. As defined in (5-46), the stator flux angle can be derived from the integral of the stator voltage reduced by the stator resistance.

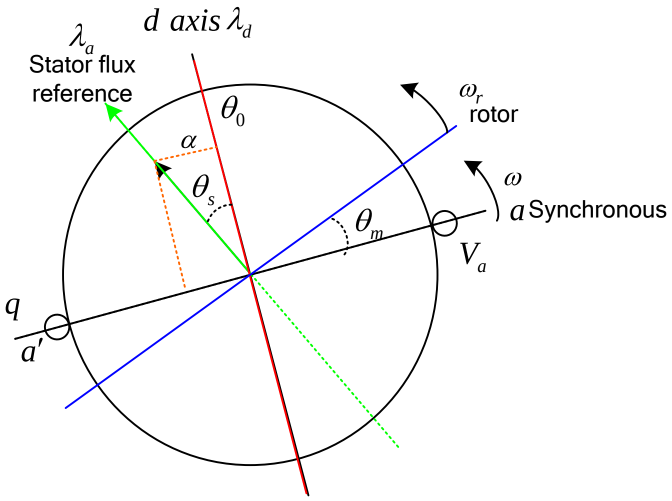

Figure 5.13 Angle difference between stator and grid converter reference

As shown in Figure 5.13, the λ_d is the grid voltage d reference frame, and the λ_a is the stator flux reference frame; the reference frame angle difference is α. Thus, by shifting angle α, the machine side impedance at the stator flux reference is changed to the stator voltage reference using the derivation steps below.

$$\begin{bmatrix} V_{ds1} \\ V_{qs1} \end{bmatrix} = \begin{bmatrix} R_s & 0 \\ \omega L_s & R_s \end{bmatrix} \begin{bmatrix} i_{ds1} \\ i_{qs1} \end{bmatrix} + \begin{bmatrix} 0 \\ h_{qr} \end{bmatrix} \quad \cdots\cdots (5\text{-}90)$$

$$\begin{bmatrix} V_{ds2} \\ V_{qs2} \end{bmatrix} = \begin{bmatrix} \cos\alpha & \sin\alpha \\ -\sin\alpha & \cos\alpha \end{bmatrix} \begin{bmatrix} V_{ds1} \\ V_{qs1} \end{bmatrix} \cdots\cdots (5\text{-}91)$$

$$\begin{bmatrix} V_{ds1} \\ V_{qs1} \end{bmatrix} = \begin{bmatrix} \cos\alpha & -\sin\alpha \\ \sin\alpha & \cos\alpha \end{bmatrix} \begin{bmatrix} V_{ds2} \\ V_{qs2} \end{bmatrix} \cdots\cdots (5\text{-}92)$$

$$\begin{bmatrix} i_{ds2} \\ i_{qs2} \end{bmatrix} = \begin{bmatrix} \cos\alpha & \sin\alpha \\ -\sin\alpha & \cos\alpha \end{bmatrix} \begin{bmatrix} i_{ds1} \\ i_{qs1} \end{bmatrix} \cdots\cdots (5\text{-}93)$$

$$\begin{bmatrix} i_{ds1} \\ i_{qs1} \end{bmatrix} = \begin{bmatrix} \cos\alpha & -\sin\alpha \\ \sin\alpha & \cos\alpha \end{bmatrix} \begin{bmatrix} i_{ds2} \\ i_{qs2} \end{bmatrix} \cdots\cdots (5\text{-}94)$$

Based on these changes, the voltage at the stator flux reference frame can be transformed to the voltage reference frame using Equation (5-95).

$$\begin{bmatrix} V_{ds2} \\ V_{qs2} \end{bmatrix} = \begin{bmatrix} \cos\alpha & \sin\alpha \\ -\sin\alpha & \cos\alpha \end{bmatrix} \begin{bmatrix} R_s & 0 \\ \omega L_s & R_s \end{bmatrix} \begin{bmatrix} \cos\alpha & -\sin\alpha \\ \sin\alpha & \cos\alpha \end{bmatrix} \begin{bmatrix} i_{ds2} \\ i_{qs2} \end{bmatrix} + \begin{bmatrix} \cos\alpha & \sin\alpha \\ -\sin\alpha & \cos\alpha \end{bmatrix} \begin{bmatrix} 0 \\ h_{qr} \end{bmatrix} \cdots\cdots (5\text{-}95)$$

$$\begin{bmatrix} V_{ds} \\ V_{qs} \end{bmatrix} = \begin{bmatrix} R_s + \omega L_s \sin\alpha\cos\alpha & -\omega L_s \sin\alpha^2 \\ \omega L_s \cos\alpha^2 & R_s - \omega L_s \sin\alpha\cos\alpha \end{bmatrix} \begin{bmatrix} i_{d\text{machine}} \\ i_{q\text{machine}} \end{bmatrix} + \begin{bmatrix} h_{qr}\sin\alpha \\ h_{qr}\cos\alpha \end{bmatrix} \cdots\cdots (5\text{-}96)$$

The machine side impedance value is expressed as,

$$\mathbf{Z}_{\text{steady state}} = \begin{bmatrix} R_s + \omega L_s \sin\alpha\cos\alpha & -\omega L_s \sin\alpha^2 \\ \omega L_s \cos\alpha^2 & R_s - \omega L_s \sin\alpha\cos\alpha \end{bmatrix} \cdots\cdots (5\text{-}97)$$

The dependent resource is listed in equation (5-98). This component is the transient response for the system, and the transient frequency is determined by h_{qr}, which is primarily affected by the decoupled controller parameters.

$$\begin{bmatrix} V_{machined} \\ V_{machineq} \end{bmatrix} = \begin{bmatrix} h_{qr}\sin\alpha \\ h_{qr}\cos\alpha \end{bmatrix} \cdots\cdots (5\text{-}98)$$

The impedance at the grid side converter shown in Equation (5-99) also includes two parts, the impedance and the dependent resource.

$$\begin{bmatrix} V_{ds} \\ V_{qs} \end{bmatrix} = \begin{bmatrix} \dfrac{(R+Lp)(T_s p+1) - PI_{dl}}{(T_s p+1)} & 0 \\ 0 & \dfrac{(R+Lp)(T_s p+1) - PI_{ql}}{(T_s p+1)} \end{bmatrix} \begin{bmatrix} i_{d\text{Grid}} \\ i_{q\text{Grid}} \end{bmatrix} + \begin{bmatrix} \dfrac{PI_{dl}}{(T_s p+1)} i_{dl}^{*} \\ \dfrac{PI_{ql}}{(T_s p+1)} i_{ql}^{*} \end{bmatrix} \cdots\cdots\cdots (5\text{-}99)$$

$$\begin{bmatrix} V_{ds} \\ V_{qs} \end{bmatrix} = \begin{bmatrix} d_{dl}^{-1} & 0 \\ 0 & d_{ql}^{-1} \end{bmatrix} \begin{bmatrix} i_{d\text{Grid}} \\ i_{q\text{Grid}} \end{bmatrix} + \begin{bmatrix} h_{dl} \\ h_{ql} \end{bmatrix} \cdots\cdots\cdots\cdots\cdots\cdots\cdots\cdots\cdots\cdots\cdots (5\text{-}100)$$

Figure 5.14 illustrates the configuration of the DFIG impedances. The machine and its converter impedance are connected in parallel with the grid side converter and its control. The machine side impedance includes the steady state value as well as the transient component. In addition to the impedance, both models have dependent resources which add transient frequency components to the system.

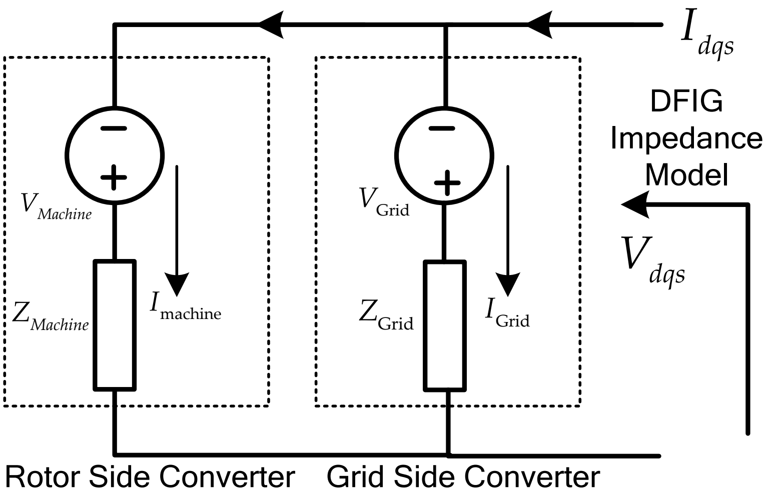

Figure 5.14 Configuration of the two parts impedance for DFIG

$$\begin{bmatrix} i_{d\text{machine}} \\ i_{q\text{machine}} \end{bmatrix} = \begin{bmatrix} Y_{11} & Y_{12} \\ Y_{21} & Y_{22} \end{bmatrix} \begin{bmatrix} V_{ds} \\ V_{qs} \end{bmatrix} - \begin{bmatrix} Y_{11} & Y_{12} \\ Y_{21} & Y_{22} \end{bmatrix} \begin{bmatrix} h_{qr}\sin\alpha \\ h_{qr}\cos\alpha \end{bmatrix} \cdots\cdots\cdots\cdots\cdots\cdots (5\text{-}101)$$

Equation (5-101) can be separated into two segments, the first being the steady state response and the second, and the transient response. The derivation below is used to obtain the paralleled impedance for the DFIG.

$$Y_{\text{steady state}} = Z_{\text{steady state}}^{-1} = \begin{bmatrix} \dfrac{R_s - \omega L_s \cos\alpha \sin\alpha}{R_s^2} & \dfrac{-\omega L_s \sin\alpha \sin\alpha}{R_s^2} \\ \dfrac{-\omega L_s \cos\alpha \cos\alpha}{R_s^2} & \dfrac{R_s + \omega L_s \cos\alpha \sin\alpha}{R_s^2} \end{bmatrix} = \begin{bmatrix} Y_{11} & Y_{12} \\ Y_{21} & Y_{22} \end{bmatrix} \cdots\cdots(5\text{-}102)$$

$$\begin{bmatrix} i_{d\text{Grid}} \\ i_{q\text{Grid}} \end{bmatrix} = \begin{bmatrix} \dfrac{T_s p + 1}{(R + Lp)(T_s p + 1) - PI_{dl}} & 0 \\ 0 & \dfrac{T_s p + 1}{(R + Lp)(T_s p + 1) - PI_{ql}} \end{bmatrix} \left(\begin{bmatrix} V_{ds} \\ V_{qs} \end{bmatrix} - \begin{bmatrix} \dfrac{PI_{dl}}{T_s p + 1} i_{dl}^{*} \\ \dfrac{PI_{ql}}{T_s p + 1} i_{ql}^{*} \end{bmatrix} \right) \cdots\cdots(5\text{-}103)$$

$$\begin{bmatrix} i_{d\,\text{Grid}} \\ i_{q\,\text{Grid}} \end{bmatrix} = \begin{bmatrix} d_{dl} & 0 \\ 0 & d_{ql} \end{bmatrix} \begin{bmatrix} V_{ds} \\ V_{qs} \end{bmatrix} - \begin{bmatrix} d_{dl} h_{dl} \\ d_{ql} h_{ql} \end{bmatrix} \cdots\cdots(5\text{-}104)$$

The equations below are used to combine the two parts of the transient response.

$$\begin{bmatrix} i_{d\text{machine}} \\ i_{q\text{machine}} \end{bmatrix} = \begin{bmatrix} Y_{11} & Y_{12} \\ Y_{21} & Y_{22} \end{bmatrix} \begin{bmatrix} V_{ds} \\ V_{qs} \end{bmatrix} - \begin{bmatrix} Y_{11} & Y_{12} \\ Y_{21} & Y_{22} \end{bmatrix} \begin{bmatrix} h_{qr} \sin\alpha \\ h_{qr} \cos\alpha \end{bmatrix} \cdots\cdots(5\text{-}105)$$

$$\begin{bmatrix} i_{d\,\text{Grid}} \\ i_{q\,\text{Grid}} \end{bmatrix} = \begin{bmatrix} d_{dl} & 0 \\ 0 & d_{ql} \end{bmatrix} \begin{bmatrix} V_{ds} \\ V_{qs} \end{bmatrix} - \begin{bmatrix} d_{dl} h_{dl} \\ d_{ql} h_{ql} \end{bmatrix} \cdots\cdots(5\text{-}106)$$

$$d_{dl} = \frac{(T_s p + 1)}{(R + Lp)(T_s p + 1) + PI_{dl}} = \frac{T_s p^2 + p}{L T_s p^3 + (R T_s + L) p^2 + (R + K_{pdl}) p + K_{idl}} \cdots\cdots(5\text{-}107)$$

$$d_{dl}{}^{-1} = \frac{(R + Lp)(T_s p + 1) + PI_{dl}}{(T_s p + 1)} = \frac{L T_s p^3 + (R T_s + L) p^2 + (R + K_{pdl}) p + K_{idl}}{T_s p^2 + p} \cdots\cdots(5\text{-}108)$$

$$h_{dl} = \frac{PI_{dl}}{(T_s p + 1)} i^{*}{}_{dl} = \frac{K_{pdl} + \dfrac{K_{idl}}{p}}{T_s p + 1} i^{*}{}_{dl} = \frac{K_{pdl} p + K_{idl}}{T_s p^2 + p} i^{*}{}_{dl} \cdots\cdots(5\text{-}109)$$

$$d_{ql} = \frac{\left(T_s p + 1\right)}{\left(R + Lp\right)\left(T_s p + 1\right) - PI_{ql}} \tag{5-110}$$

$$d_{ql}{}^{-1} = \frac{\left(R + Lp\right)\left(T_s p + 1\right) - PI_{ql}}{\left(T_s p + 1\right)} \tag{5-111}$$

$$h_{ql} = \frac{PI_{ql}}{\left(T_s p + 1\right)} i^*{}_{ql} = \frac{K_{pql} + \frac{K_{iql}}{p}}{\left(T_s p + 1\right)} i^*{}_{ql} = \frac{K_{pql} p + K_{iql}}{T_s p^2 + p} i^*{}_{ql} \tag{5-112}$$

$$\lim_{t \to \infty} d_{dl} = 0 \tag{5-113}$$

$$\lim_{t \to \infty} d_{dl}^{-1} = K_{idl} \tag{5-114}$$

$$\lim_{t \to \infty} h_{dl} = K_{idl} i_{dl}^* \tag{5-115}$$

$$\lim_{t \to \infty} d_{ql} = 0 \tag{5-116}$$

$$\lim_{t \to \infty} d_{ql} = K_{iql} \tag{5-117}$$

$$\lim_{t \to \infty} h_{dl} = K_{idl} i^*{}_{ql} \tag{5-118}$$

The DFIG output current resource can be derived by adding the machine side converter and the grid side converter.

$$\begin{aligned}\begin{bmatrix} V_{ds2} \\ V_{qs2} \end{bmatrix} &= \begin{bmatrix} d_{dl} + Y_{11} & Y_{12} \\ Y_{21} & d_{ql} + Y_{22} \end{bmatrix}^{-1} \begin{bmatrix} i_{ds} \\ i_{qs} \end{bmatrix} + \\ &\begin{bmatrix} d_{dl} + Y_{11} & Y_{12} \\ Y_{21} & d_{ql} + Y_{22} \end{bmatrix}^{-1} \left(\begin{bmatrix} d_{dl} h_{dl} \\ d_{ql} h_{ql} \end{bmatrix} + \begin{bmatrix} Y_{11} & Y_{12} \\ Y_{21} & Y_{22} \end{bmatrix} \begin{bmatrix} h_{dr} \sin\alpha \\ h_{qr} \cos\alpha \end{bmatrix} \right)\end{aligned} \tag{5-119}$$

In summary, the impedance for the DFIG consists of two components seen in Figure 5.15.

$$Z(s)=\begin{bmatrix} Z_{11} & Z_{12} \\ Z_{21} & Z_{22} \end{bmatrix}=\begin{bmatrix} d_{dl}+Y_{11} & Y_{12} \\ Y_{21} & d_{ql}+Y_{22} \end{bmatrix}^{-1} \cdots\cdots\cdots\cdots (5\text{-}120)$$

$$V(s)=\begin{bmatrix} d_{dl}+Y_{11} & Y_{12} \\ Y_{21} & d_{ql}+Y_{22} \end{bmatrix}^{-1}\left(\begin{bmatrix} d_{dl}h_{dl} \\ d_{ql}h_{ql} \end{bmatrix}+\begin{bmatrix} Y_{11} & Y_{12} \\ Y_{21} & Y_{22} \end{bmatrix}\begin{bmatrix} h_{qr}\sin\alpha \\ h_{qr}\cos\alpha \end{bmatrix}\right) \cdots (5\text{-}121)$$

$$I(s)=\begin{bmatrix} d_{dl}h_{dl} \\ d_{ql}h_{ql} \end{bmatrix}+\begin{bmatrix} Y_{11} & Y_{12} \\ Y_{21} & Y_{22} \end{bmatrix}\begin{bmatrix} h_{qr}\sin\alpha \\ h_{qr}\cos\alpha \end{bmatrix} \cdots\cdots\cdots\cdots (5\text{-}122)$$

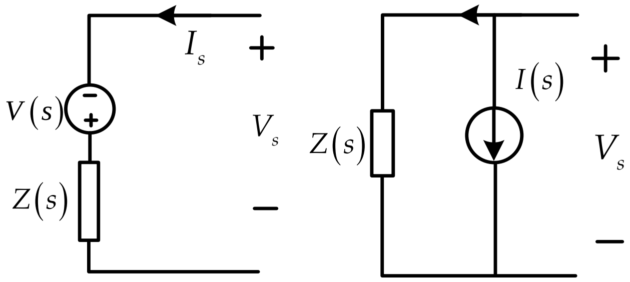

Figure 5.15 Equivalent impedance of DFIG model

Adding zero components into the matrix assumption that zero axis components are,

$$d_{0l}=0 \cdots\cdots\cdots\cdots\cdots\cdots (5\text{-}123)$$

$$Z_{q0}=Z_{0q}=0, Z_{d0}=Z_{0d}=0, \text{ and } Z_{00}=0 \cdots\cdots\cdots\cdots (5\text{-}124)$$

$$Z_s=\underbrace{\begin{bmatrix} Z_{11} & Z_{12} & Z_{13} \\ Z_{21} & Z_{22} & Z_{23} \\ Z_{31} & Z_{32} & Z_{33} \end{bmatrix}}_{Z_{steady}(s)}+\underbrace{\begin{bmatrix} d_{dl}^{-1} & 0 & 0 \\ 0 & d_{ql}^{-1} & 0 \\ 0 & 0 & d_{0l}^{-1} \end{bmatrix}}_{Z_{transient}(s)}=\begin{bmatrix} z_{11}(s) & z_{12}(s) & 0 \\ z_{12}(s) & z_{22}(s) & 0 \\ 0 & 0 & z_{33}(s) \end{bmatrix} \cdots (5\text{-}125)$$

The impedance can be transferred to the time domain using the Laplace transform, and it can be changed to *012* sequences by multiplying by A.

$$Z_{dq}(t)=L^{-1}\left[Z_{dq}(s)\right]=\begin{bmatrix} z_{11}(t) & z_{12}(t) & 0 \\ z_{21}(t) & z_{22}(t) & 0 \\ 0 & 0 & z_{33}(t) \end{bmatrix} \cdots\cdots\cdots\cdots (5\text{-}126)$$

$$i_{dq0}=K_s i_{abc} \cdots\cdots\cdots\cdots (5\text{-}127)$$

$$i_{abc}=K_s^{-1} i_{dq0} \cdots\cdots\cdots\cdots (5\text{-}128)$$

$$I_{abc}=AI_{012} \cdots\cdots\cdots\cdots (5\text{-}129)$$

$$I_{012}=A^{-1}I_{abc} \cdots\cdots\cdots\cdots (5\text{-}130)$$

$$A=\begin{bmatrix} 1 & 1 & 1 \\ 1 & a^2 & a \\ 1 & a & a^2 \end{bmatrix} \cdots\cdots\cdots\cdots (5\text{-}131)$$

$$\begin{bmatrix} V_a \\ V_b \\ V_c \end{bmatrix}=K^{-1}Z_sK\begin{bmatrix} i_a \\ i_b \\ i_c \end{bmatrix}+K^{-1}V(s) \cdots\cdots\cdots\cdots (5\text{-}132)$$

$$\begin{bmatrix} V_a^0 \\ V_a^1 \\ V_a^2 \end{bmatrix}=A^{-1}K^{-1}Z_sKA\begin{bmatrix} I_a^0 \\ I_a^1 \\ I_a^2 \end{bmatrix}+A^{-1}K^{-1}V(s) \cdots\cdots\cdots\cdots (5\text{-}133)$$

The impedance matrix for the DFIG is expressed in Equation (5-134),

$$Z_{012}=A^{-1}K^{-1}Z_sKA \cdots\cdots\cdots\cdots (5\text{-}134)$$

5.4 The Simulation Results of the Z_{bus} Matrix

The results from the DFIG Z_{bus} matrix model are compared with the PSCAD results using the same capacity and control scheme. Figure 5.16 shows the steady state results for the two models, the red curve representing the PSCAD results and blue curve, the impedance matrix results. As this figure shows, the two results have some frequency but a small angle difference. These differences may be caused by neglecting the stator resistance when calculating the stator flux angle. The impedance results are smoother because the PWM block handled as the ideal switcher.

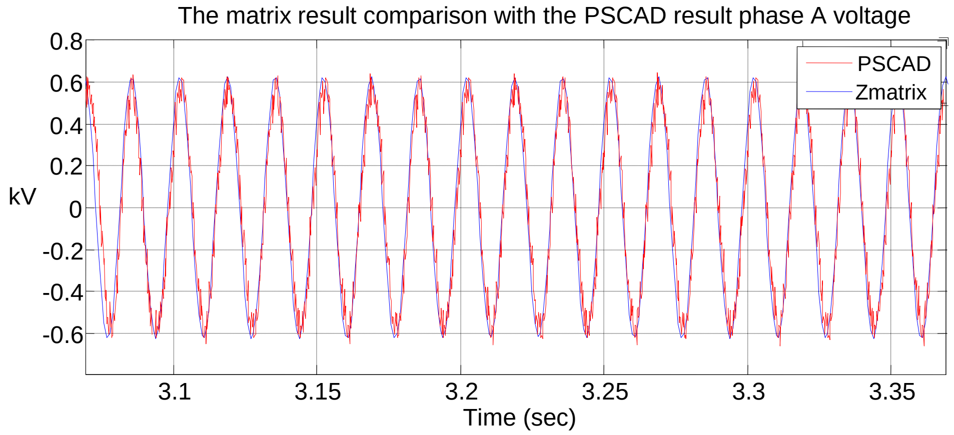

Figure 5.16 Steady state results for two models

Assume that a fault is place at *t*=3 sec lasts for 0.05 sec. The red curve represents the time domain numerical results, while the blue curve is the frequency domain impedance results. The PSCAD result exhibits more distortion because in the frequency impedance derivation, the PWM is applied as ideal switcher. The comparison of the d axis stator current comparison with PSCAD result can be seen in Figure 5.17, and the comparison of the q axis stator current comparison with PSCAD result can be seen in Figure 5.18.

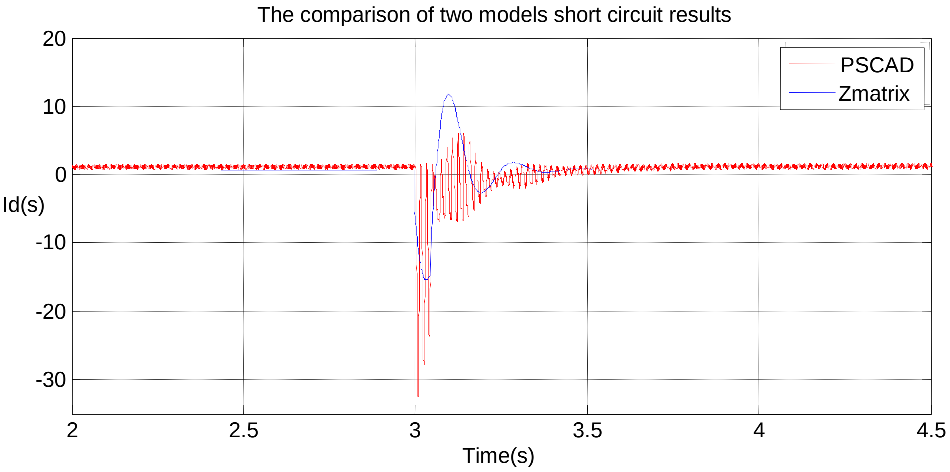

Figure 5.17 Comparison of two models short circuit results

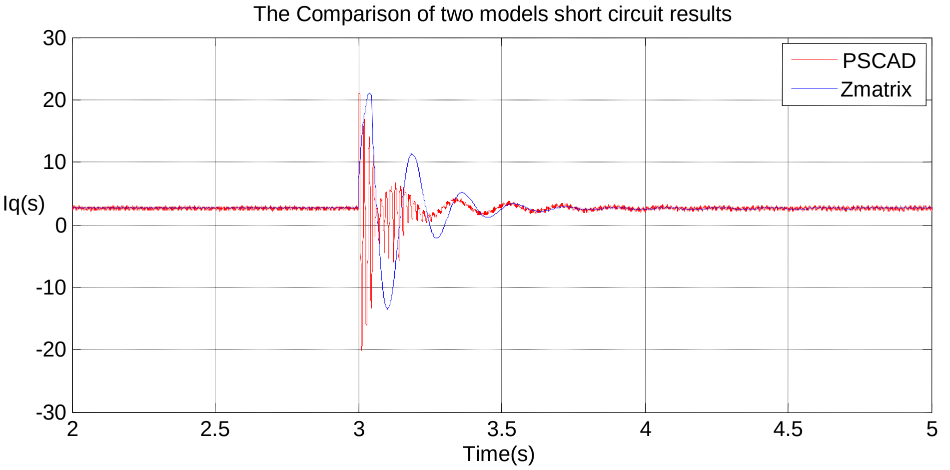

Figure 5.18 Comparison of two models short circuit results

5.5 The Conclusions and Extended Idea

The frequency domain Z_{bus} matrix is another method for studying the DFIG transient interaction with the system. The DFIG frequency impedance model was derived in this chapter. In order to obtain the decoupled explicit expression of the relationship between V_{abc} and I_{abc} of the DFIG, the feed forward decoupled control is applied at both the grid side converter and the machine side converter. The combination of the two parts impedance has to be in the same reference frame.

The derived Z_{bus} matrix can be used to calculate the transient of specific bus in the system. In order to do investigate the transient of specific bus in power system, the frequency impedance of the specific bus is necessary rather than the detailed system information. It is the purpose to derive the frequency impedance for DFIG. This method not only less time-consuming than the PSCAD simulation but also is more convenient.

CHAPTER SIX

ECONOMIC EVALUATION AND DESIGN CONSIDERATION OF HVAC AND HVDC OFFSHORE WIND FARM

6.1 Introduction

The wind power industry has experienced a dramatic growth over the last ten years. The department of Energy projects that by 2030 wind energy is expected to reach 330GW worldwide, with 54GW of it generated by offshore farms [39][70][71]. As Figure 6.1 shows, the total installation capacity of offshore wind energy will reach approximately 12GW worldwide by 2014.

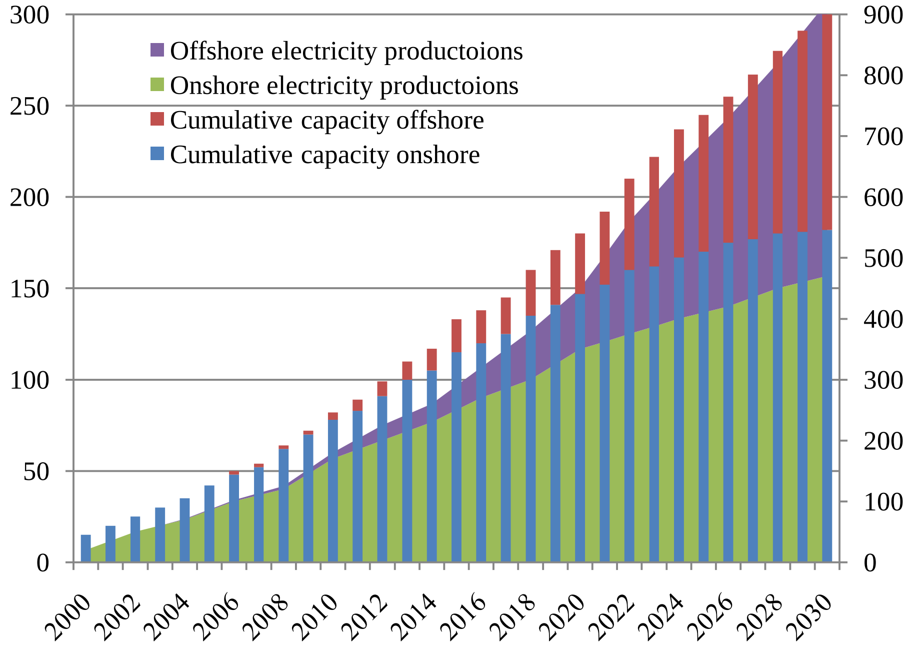

Figure 6.1 EWEA data for wind energy production and capacity

The offshore wind industry is increasingly extending its project capacity as well as its distance from the onshore. The largest operating offshore wind farm in the world today is London Array (Phase I) in the United Kingdom, its capacity reaching 630MW[72][73]. In 2011 the average distance of offshore wind farms in the world was approximately 24km. For the projects currently under construction, the average is 33km [74].

Table 6.1 shows the offshore wind turbine depth and the distance impact on turbine cost.

Table 6.1 Impact of depth and distance on cost

Water depth (m)	Distance from shore (km)							
	0-10	10-20	20-30	30-40	40-50	50-100	100-200	>200
10-20	1.00	1.02	1.04	1.07	1.09	1.18	1.41	1.60
20-30	1.07	1.09	1.11	1.14	1.16	1.26	1.50	1.71
30-40	1.24	1.26	1.29	1.32	1.34	1.46	1.74	1.98
40-50	1.40	1.43	1.46	1.49	1.52	1.65	1.97	2.23

Similar for onshore wind farms, wind turbines usually account for half of the total cost in offshore wind farms, while the electrical connection system, wind farm maintenance, commission, and operation are more expensive than for on onshore wind farm. As the offshore wind projects reach further into the ocean, their cost increases based on the depth and the distance from shore. Concerns about both the ability and the length of time to pay for those projects need to be considered before the planning stage begins. Figure 6.2 compares the costs for both offshore and onshore wind farms in Europe.

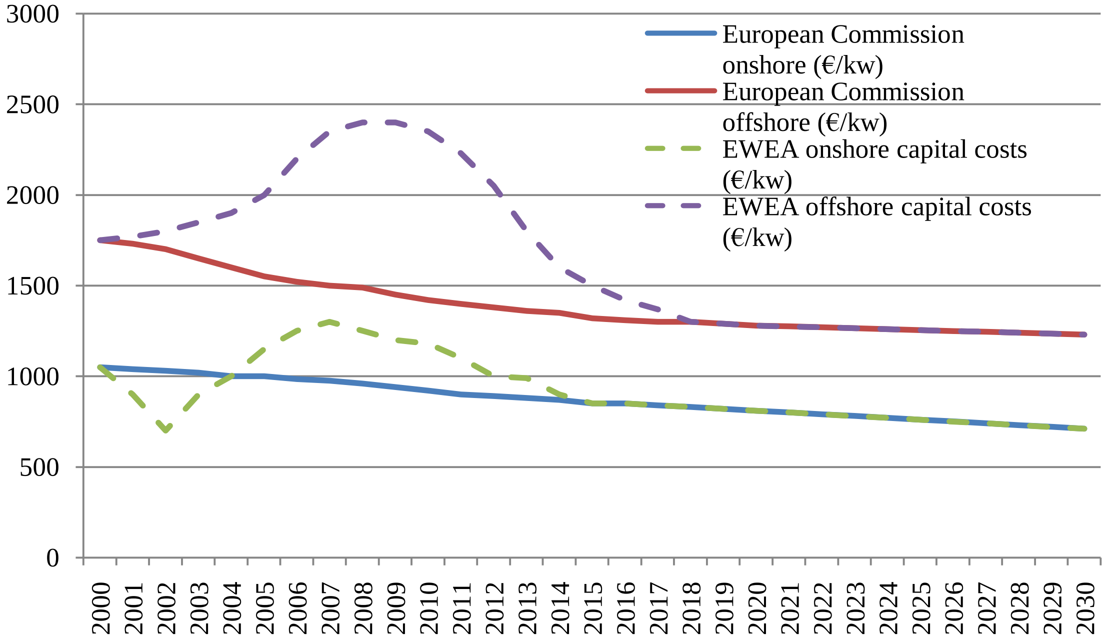

Figure 6.2 Offshore wind and onshore wind cost (EWEA data)

In Table 6.2 lists the capacity and the costs for various offshore wind farms

Table 6.2 Offshore wind farm and its cost

Project	**Capacity(MW)**	**Year Online**	**MEuro**	**M$**
Barrow	90	2006	37	59.22
Robin Rigg	180	2009	59	95.22
Gunfleet Sands	173	2010	46	75.24
Thanet	300	2010	189	306.72
Ormonde	150	2011	87	141.12
Greater Gabbard	504	2011	344	557.82
Walney1	151	2011	99	161.28
Walney2	216	2011	104	169.38
Sheringhan Shoal	317	2012	187	303.12

Large offshore wind farms requires a reliable and economic transmission system to deliver energy to the load center [75][76][77]. The transmission systems currently available for bulk energy are either high voltage alternating current (HVAC) transmission or high voltage direct current (HVDC) transmission [77] [78], with of the majority being the former. The primary advantage of the HVAC system is its reliability because of the maturity of the technology. However, its limitation is the three-phase submarine cable. For a wind farm installation capacity of 500 MW, a suitable HVAC submarine cable with 115KV voltage must consist of two three-phase submarine cables. That would cause loss and need reactive power compensators. The main expense of HVDC transmission system lies in the converter equipment at each end. Its benefits include reduced losses because the transmission voltage may step up as high as 500kV, reducing the size of the submarine cable needed. In addition, the cost of an HVDC system can be adjusted for a distance from the shore longer than 50-60kM. Several studies have compared the cost of the HVAC and HVDC transmission systems in relation to wind farm installation capacities and distance to the shore. It is important to investigate the cost and the energy losses for offshore wind farms using different technologies. Based on an engineering approach, the cost of the offshore wind farm includes the equipment capital, the installation, operation and maintenance, and the decommissioning cost.

The cost of an offshore wind farm can be classified into two categories: the wind farm facility investment and the capitalized cost of expected constrain energy due to maintenance [79][80][81]. The first is composed of the cost of the wind turbines, the undersea cable network, and the offshore substation with such relative equipment as transformer, reactive compensators and switchgears as well as the cost of an onshore substation and reactive compensation. The optimal designs for wind farm transmission systems are based on the economics of offshore wind farm installation as well as the connection impact on the system.

In this chapter the costs of offshore wind farms with HVAC and HVDC transmission systems will be evaluated and compared with various electrical transmission systems including HVAC, HVDC (Line Commuter Converter) LCC, and HVDC VSC. In addition, the technical performance of HVAC and HVDC VSC during steady state performance will be compared as well. Data are from existing offshore wind projects in Europe, industry reports, and government websites. Assumptions are made based on projects of the same size.

6.2 Configurations of Offshore Wind Farms Transmission Systems

6.2.1 Plan A Directly Connected Configuration

In the beginning stages of the offshore wind industry, wind farms were directly connected to an onshore system [82][83]. Usually, this configuration was applied if the wind farm was not large. After the wind energy is generated from the wind turbines in the windmill, the voltage is improved to a middle level such as 34.5kV. Middle voltage submarine cables are then used to deliver this energy to an onshore distribution system. This is an economical method for delivering wind energy to the system. However, the implementation of such systems has decreased recently due to the high loss, the constraint of the energy losses and the distance from the shore [84][85][86]. Figure 6.3 shows the direct connection of an offshore wind farm to the onshore substation without an offshore platform.

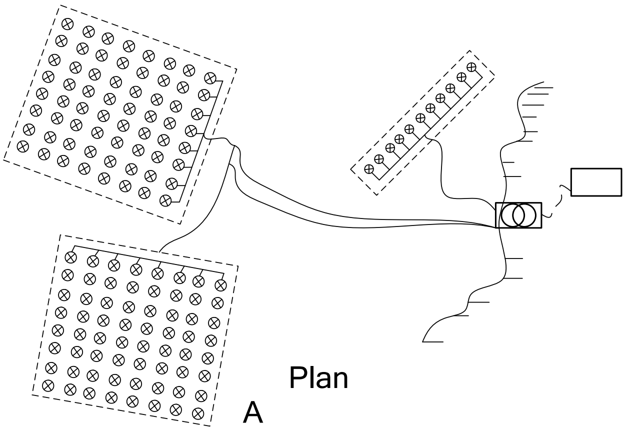

Figure 6.3 Direct connection of an offshore wind farm

6.2.2 Plan B the HVAC Transmission System

Figure 6.4 shows the basic configuration of an HVAC system for offshore wind farms. The type of HVAC transmission system steps up the output voltage at the wind turbine terminal from 0.69kV to medium voltage, typically in the range of 30kV-36kV, in an offshore wind mill. Wind turbines are connected by an inter array of submarine cables (XPLE cables) [87][88][89]. Before the wind energy is transferred to the onshore substation, an offshore substation is implemented to increase the voltage level while at the same time to decreasing the energy loss through the transmission. A high voltage AC transmission level is usually in the range of 115kV to 400kV. FACTS compensation units like the SVC or TCR are placed both onshore and offshore at each end of the submarine cables. The onshore substation may need to be upgraded if the grid interface substation does not have enough transformer capacity.

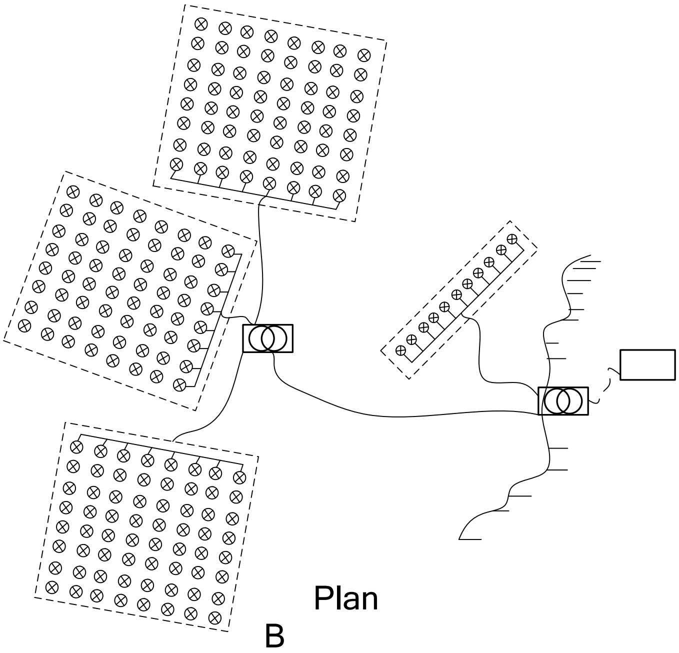

Figure 6.4 HVAC transmission systems for an offshore wind farm

The high voltage level ranges from 115kV to 230kV in the existing offshore wind projects. It is assumed for the research reported here that the distance from the offshore wind farm to the shore is 45km, and the wind farm capacity is 500MVA. For a wind farm of this size, a reactive compensator is critical for the HVAC transmission system. The critical distance is achieved when half of the reactive current produced by the cable reaches nominal current at the receiving end of one cable [39]. Recently, research focusing on maximizing the transmission distance for HVAC system has been conducted, but the implementation of those solutions is impractical. One solution involves using more than three phases, but it will increases the cost of the submarine cables [76][77]. According to Brakelmann in [45], the cable loss per length can be calculated as

$$P=\left(P_{\max}-P_D\right)\left(\frac{1}{I_N}\right)^2 v_\theta+P_D \quad \cdots\cdots (6\text{-}1)$$

where,

P_{max} is the nominal total cable loss;
P_D is the dielectric loss per core;
I is the load current;
I_N is the nominal current;
v_θ is the temperature correction coefficient calculated from:

$$v_\theta=\frac{c_\alpha}{c_\alpha+\alpha_T\Delta\theta_{\max}\left[1-\left(\frac{I}{I_N}\right)^2\right]} \quad \cdots\cdots (6\text{-}2)$$

where,

α_T is the temperature coefficient of the conductor resistivity [1/^{o}K];
c_α is the constant, i.e. c_α=1- α_T(20^{o}C-θ_{amb});
$\Delta\theta_{max}$ is the maximal temperature rise, i.e.75^{o}C;

A method for calculating the loss of cable and transformer is,

$$T_{loss}=n_T\left(\frac{A_w\cdot P_W^M}{V\cdot pf}\right)^2 R_T \quad \cdots\cdots (6\text{-}3)$$

$$C_{loss}=n_c\left(\frac{A_w\cdot P_W^M}{V\cdot pf}\right)^2 R_c \quad \cdots\cdots (6\text{-}4)$$

The offshore wind farm transmission systems online in the world today implement HVAC transmission system [90]. However, HVAC transmission system has submarine cable reactive power limitation and the submarine cable is more expensive if the voltage level is higher. This makes this scheme particularly important to minimize the cost of connecting offshore wind farms to the grid.

6.2.3 Plan C the HVDC Transmission System

The HVDC is the new solution- for long-distance electric transmission onshore, potentially applicable for large scale offshore wind farms far from the coastal line. HVDC Line Commutated Converters (LCC) has been implemented for power transmission on land for years. However, they have never been used in offshore wind power transmission. Power electronics with turn-on capabilities (thyristors) require a strong network voltage, which most of the offshore wind farms lack [76][77]. However, this issue can be solved by using an auxiliary voltage source. AC and DC filters are required by HVDC LCC system for harmonics, and STATCOMs or capacitor banks in the converters are required for voltage support. Based on the equipment required, the offshore converter station needs a large area in the ocean, increasing the cost of the project. The cost of HVDC LCC system can be calculated using the equation below based on the Brakelmann theory [76][77].

$$P_{cable} = P'_{L\max} \cdot \left(\frac{I}{I_N} \right)^2 \cdot v_\theta \quad \cdots\cdots (6\text{-}5)$$

$$P'_{L\max} = R_0 \cdot c_m \cdot I_N^2 \cdot I_{cable} \quad \cdots\cdots (6\text{-}6)$$

$$c_m = 1 + \alpha_{20} \left(\Delta\theta_{L\max} + \theta_{amb} - 20^o C \right) \quad \cdots\cdots (6\text{-}7)$$

$$c_\alpha = 1 - \alpha_T \left(20^o C - \theta_{amb} \right) \quad \cdots\cdots (6\text{-}8)$$

$$v_\theta = \frac{c_\alpha}{c_\alpha + \alpha_T \Delta\theta_{L\max} \cdot \left[1 - \left(\frac{I}{I_N} \right)^2 \right]} \quad \cdots\cdots (6\text{-}9)$$

where,

R_0	represents the DC resistance of the conductor at 20℃ per unit length,
α_{20}	represents the constant mass temperature coefficient at 20℃;
P_{Lmax}	represents the lost power in the cable at its maximum operating temperature;
$\Delta\theta_{L\max}$	represents the maximum operating temperature of the insulator; it is set to 55℃
I	represents the current flowing into the cable;
I_N	represents the nominal current of the cable;
I_{cable}	represents the length of the cable.

A HVDC-VSC interconnected offshore wind farm is shown in Figure 6.5. This system consists of a rectifier converter station, an inverter converter station and two submarine DC cables. Both converters can absorb or deliver reactive power to the AC grid. Unlike the HVDC LCC system, this one provides independent control of the reactive and active power as well as voltage and frequency stability to the system. The high frequency switching reduces the number of harmonics in the system without the use of a filter. Thus, the offshore converter station is smaller than the one for the HVDC LCC system. The advantages of HVDC VSC make it an attractive solution for offshore wind energy transmission system. The loss calculations can be found in [76][77]. The losses from the two converter are assumed to be the same.

$$P_1 = (1 - x_s) P_{in} \quad \cdots\cdots \text{(6-10)}$$

$$P_C = P_1 - P_2 = R \cdot I^2 = R \cdot \left(\frac{P_1}{V_C} \right)^2 \quad \cdots\cdots \text{(6-11)}$$

$$P_{out} = (1 - x_s) P_2 \quad \cdots\cdots \text{(6-12)}$$

$$\frac{R}{V_C^2}\left(1-x_s\right)^3 P_{in}^2-\left(1-x_s\right)^2 P_{in}+P_{out}=0 \cdots\cdots\cdots\cdots\cdots\cdots\cdots\cdots\cdots\cdots \text{(6-13)}$$

where,

x_s is the percent loss;

P_{in} is the input power into the rectifier station;

P_1 is the output power from the rectifier station;

P_2 is the input power into the inverter station;

P_{out} is the output power from the inverter station;

V_c is the rated voltage of the cable;

I is the current flowing in the cable.

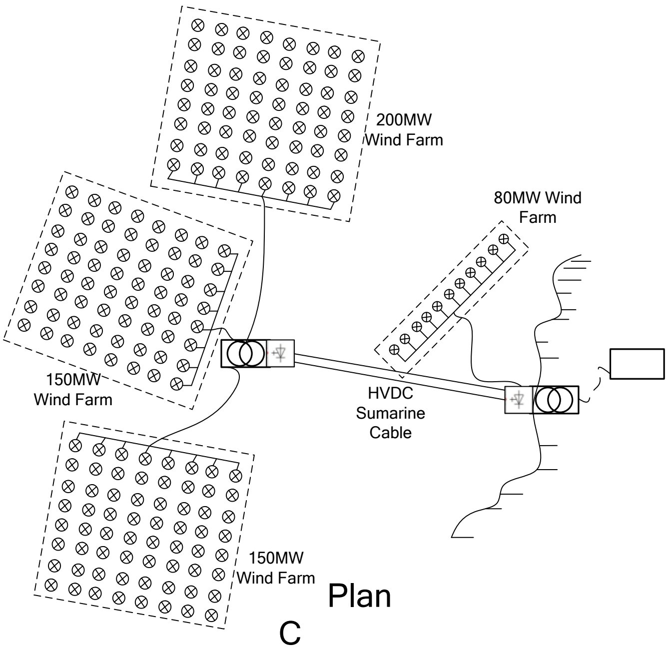

Figure 6.5 Shows the HVDC wind energy transmission scheme

Given the specific project parameters such as the installation capacity of the wind farm, the distance to the shore, the type of transmission system selected, and the design of the substation, the optimized offshore wind farm system configuration can be designed based on an economic evaluation as well as an electrical stimulation[76] .

$$C_{invest} = \frac{r\left(1+r\right)^{N} \cdot N}{\left(1+r\right)^{N} - 1} \cdot Invest \quad \cdots\cdots(6\text{-}14)$$

The annual installment for the loan in dollars can be calculated using

$$R = \frac{r\left(1+r\right)^{N}}{\left(1+r\right)^{N} - 1} \cdot Invest \quad \cdots\cdots(6\text{-}15)$$

where,

C_{invest}	is the total investment paid off in dollars,
R	is the interest rate,
N	is the life time of the project in years,
$Invest$	is the investment paid today in dollars.

$$E_D = P_{outAVG} \cdot \left(1 - \frac{L}{100}\right) \cdot T \cdot \left(1 - \frac{U_n}{100}\right) \quad \cdots\cdots(6\text{-}16)$$

where,

E_D	is the amount of energy delivered in kWh,
P_{outAVG}	is the average output power from the wind farm (kW)
L	is the average power losses in the transmission system,
T	is the operational time of the wind farm under one year in hours.
Un	is the unavailability parameters defined by

$$U_n = \frac{E_{NT}}{E_T} \quad \cdots\cdots(6\text{-}17)$$

where,

E_{NT}	is the energy not transmitted
E_T	is the energy that could have been transmitted.

6.3 Offshore Wind Energy System Components and Costs

This section presents the cost breakdown of the offshore wind farm related to the electrical equipment, including a comparison with several European offshore wind farms of the same size. The material cost comprises one third of the total expenditure for the project. The capital expenditure of the offshore wind project is divided into the following three categories [99]:

1. Labor costs, which comprise more than one third of the total cost of the project expenditure;

2. Materials, which include the wind turbine, the balance system, and the transmission system;

3. Others cost including taxes and insurance equaling up to one third of the total cost.

6.3.1 Offshore Wind Turbine Foundation Cost

Figure 6.6 illustrates the components of a wind turbine, including the nacelle, blades, gearbox, generator, and other parts. Typically, the offshore wind turbines installed today range from 1MW to 5MW, with larger capacity wind turbines under development. For the South Carolina offshore wind farm project, a 3.6MW GE DFIG offshore wind turbine is assumed to be used. Table 6.3 lists the estimated cost for each component of the wind turbine based on the European market with the realization it will vary with time.

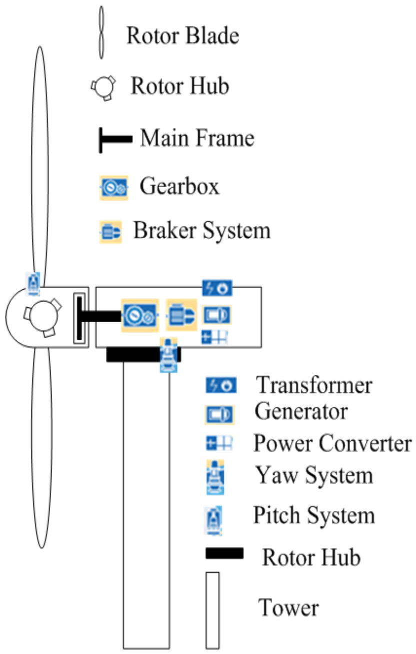

Figure 6.6 Wind turbine components

Table 6.3 Wind turbine components and their price

Component	% of Cost	M$/MW	M$/3.6MW
Nacelle	2%	0.036	0.1296
Blades	20%	0.432	1.5552
Gearbox	15%	0.324	1.1664
Generator	4%	0.090	0.3240
Controller	10%	0.216	0.7776
Rotor Hub	5%	0.108	0.3888
Transformer	4%	0.090	0.3240
Tower	25%	0.540	1.9440
Others	15%	0.324	1.1664
Total	100%	2.160	7.7760

The wind generator support system includes the foundation, the transition piece, and the scour protection. The four types of foundations widely used in offshore wind farms are the Gravity Based Structure (GSB), the monopole, the jacket foundation and the tripod foundation. A brief diagram of each can be found in Figure 6.7. As shown in Figure 6.8, 74% of the offshore wind farms online today use the monopole structure. Thus, this research uses the monopole foundation in its evaluation.

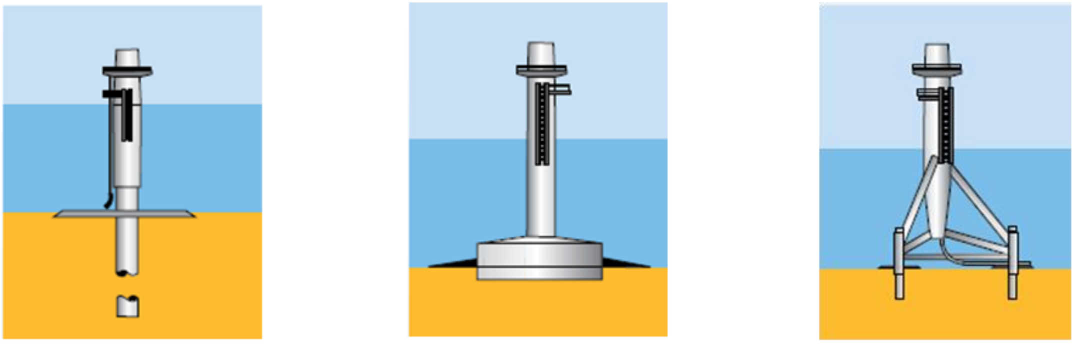

Monopile

Gravity based structure

Space Frame
(Tripod)

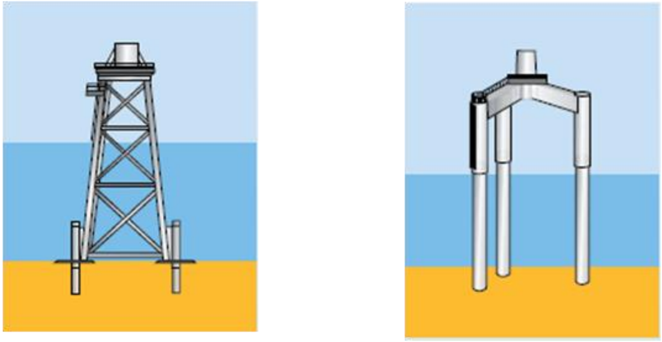

Space Frame
(Jacket)

Space Frame (Tri-pile)

Source: EWEA

Figure 6.7 Different types of foundations used in offshore wind projects

Figure 6.8 lists the cost of various types of foundations based on water depth. For the South Carolina offshore wind project, the second stage will be designed in state water, so the depth is assumed to be approximately 30-39 meters.

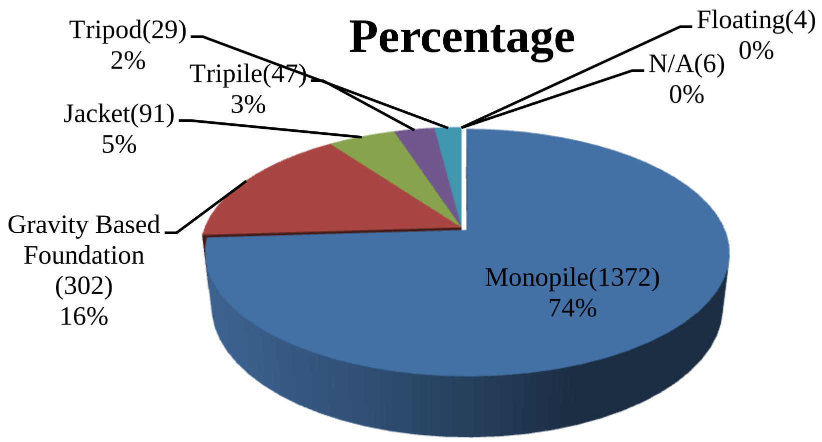

Figure 6.8 Offshore wind farm foundations (EWEA)

The installation fee has to be considered in the wind turbine cost. As can it can be seen in Table 6.5, for each offshore wind turbine of 3.6MW, the installation cost is approximately 2.3328M$.

Based on the prices listed in the Table 6.4, the cost of a wind turbine for an offshore wind farm with 500MW capacity (139 wind turbines) can be calculated. The cost for each, which includes the equipment and installation equals 7.776+4.6656+2.3328=14.7744M$, meaning139 wind turbines cost 1.1911×0.58= 0.698B$=698M$.

Table 6.4 Cost of different types of foundations

Depth(Meter)	**GBS(M$)**	**Monopile(M$)**	**Jacket(M$)**	**Tripod(M$)**
0-19	1.7496	2.7864	2.3328	3.4992
20-29	2.4624	3.4992	2.916	4.6656
30-39	4.1472	**4.6656**	4.4064	5.2488
40+	5.832	5.832	5.832	5.832

Table 6.5 Installation cost for wind turbines

Installation Type	**% of Cost**	**M$/3.6MW**
Turbine Installation	20%	0.4536
Foundation Installation	50%	1.1664
Electrical Installation	30%	0.7128
Total	100%	**2.3328**

6.3.2 Offshore Substation and Converter Station

The offshore substations increase the transmission voltage level, thereby decreasing the transmission loss from the wind farm to the point of common coupling (PCC). Whether the offshore substation is required depends on the size of the wind farm as well as its distance from the shore. The capacity and the optimal number of transformers in an offshore substation need to be investigated in terms of the economic constraint and the system reliability. The Table 6.6 lists some of the offshore wind farms in the world online including their number of offshore substations well as their installation capacity.

Table 6.6 Wind farm projects online today with offshore substations

Country	**Project**	**MW**	**Number of Substations**	**Online**
Denmark	Horns Rev	160	1	2002
Denmark	Nysted	166	1	2003
UK	Barrow	90	1	2006
Sweden	Lillgrund	110	1	2007
Netherlands	Prince Amaila	120	1	2008
Germany	Alpha Ventus	60	1	2009

Country	**Project**	**MW**	**Number of Substations**	**Online**
UK	Gunfleet Sands	172	1	2009
UK	Robin Rigg	180	2	2009
Denmark	Horns Rev	207	1	2009
Germany	Borkum 2 Cluster	n/a	1	2009
		1265	11	

It is assumed that the cost for an HVAC Substation is 0.4176 M$/MW, which includes the costs of the electrical equipment and the structure as well as the installation cost. The detailed price list can be found in Table 6.7. As this table indicates, the cost for a 500MW offshore wind farm with one offshore substation is approximately 208M$.

Table 6.7 Average cost of an HVAC offshore substation

Component	**M$/MW**
Substation Electrical Equipment	0.3492
Substation Structure & Installation	0.0684

The Table 6.8 lists the average costs for an HVDC offshore substation and a converter station, including the HVDC converter devices and the power transformers, as well as the switchgear, etc. The converter requires approximately 85% of the cost of the offshore substation. The cost for an HVDC Substation with VSC equipment is 0.351 M$/MW, and for a 500MW offshore wind farm with an HVDC transmission system, the cost of an offshore substation and converter station as well as the station onshore is approximately 175.5×2=351 M$.

Table 6.8 Average cost of an HVDC offshore substation

Component	% Share	M$/MW
VSC HVDC	85	0.2970
Power Transformers	4	0.0144
Aux. Transformers, Generators & Systems	3	0.0108
HV & LV Switchgear	6	0.0216
Workshop, Accommodation & Fire Protection	2	0.0072

6.3.3 Submarine Cable (HVAC and HVDC)

The submarine cables connect the turbines inside the wind farm as well as the wind farm to the onshore electrical grid. Small array cables with medium voltage, usually 34.5kV, connect the wind turbines in rows or in strings; the length of these cables depends on the configuration and layout of the wind farm. The large array cable with a high voltage of 115kV, which is assumed for the South Carolina offshore wind project, transmits wind energy from the offshore wind farm to the onshore grid at the common collection point. The length of this array cable depends on the distance from offshore wind farm to the onshore substation. Table 6.9 lists these costs based on the European market.

Assume l73km of a small array cable for a 500MV an offshore wind farm is needed, the cost of which is 0.252xl73=156.9456 M$. For the HVAC transmission system, 50km of a large array submarine cable is assumed for the offshore wind farm, costing 0.684×50=34.2M$. The installation cost for these two HVAC submarine cables is 0.18×123=22.14M$ HVDC. It is assumed that the submarine cable for the HVDC transmission system is 50km, and its cost is 0.594×50 = 29.7M$, plus an HVDC installation cost of 0.54×50 = 27M$.

Table 6.9 HVAC and HVDC submarine cable cost

Component	**M$/kM**
Small Array Cable AC(240mm^2)	0.252
Large Array Cable AC(630mm^2)	0.684
AC cable Installation(Average)	0.180
Export Cable(HVDC)(1600mm^2)	0.594
DC cable Installation(Average)	0.540

6.3.4 The Summary of Offshore Wind Farm Capital Costs

This cost analysis suggests that for an offshore wind farm with a capacity of 500MW, the 115KV HVAC transmission system requires two three-phase submarine cables costing more than the ones used in the HVDC transmission system.

Table 6.10 and Table 6.11 summarize the costs for an offshore wind farm based on the prices listed above.

Table 6.10 Summary of offshore wind farm configuration costs

Project (M$)	Submarine Cable	Substation	Cost
HVAC	259.2	208.8	468
HVDC	113.4	451	564.4

Table 6.11 Summary of the offshore wind farm cost breakdown

Offshore Electrical Facility	Cost
AC Substation	168.5k$/MVA
Connection to grid (breaker, switcher)	1000 k$/Bay
Reactive compensation(shunt reactor)	45.37 k$/MVAR
Costs HVDC VSC converter station 150kV	257.84 k$/MVAR
Cable Installation(AC)	354.53 k$/kM
Cable Installation(DC)	322.3 k$/kM
Cable Installation(AC 34.5KV)	171.7 k$/kM[1]
Cable Installation(AC 115KV)	10.67M$/kM[2]
Cable Installation(DC 115KV)	12.13k$/kM[1]

In Table 6.12 below lists the cost breakdown of the Homs Rev offshore wind farm in Denmark and the Nysted offshore wind farm in Germany for comparison.

Table 6.12 Offshore wind farm online capital cost breakdown

Project (M$)	Land Cable		Submarine Cable		Offshore Substation	Reactive Compensation	Total Cost	Project Capacity /MW
	Supply	Installation	Supply	Installation				
Horns Rev	7.119	6.78	11.187	6.554	23.504	2.26	50.85	160
Nysted	3.729	3.616	3.503	3.39	26.442	1.13	42.375	166

6.4 The Steady State and Switching Transient Performance

This section reports the simulation in PSCAD of the steady state performance of two electrical transmission configurations for the 500MW second stage of the SC offshore wind farm project (HVAC and HVDC). The equivalent type three wind turbine-based (Doubly Fed Induction Generator) offshore wind farm are implemented. Both of them are connected to the SC transmission system.

6.4.1 HVDC Connection for Offshore Wind Farm

The 500MW offshore wind farm, which is based on DFIG, is connected to the system onshore through the HVDC transmission system [92]. The output voltage at the wind turbine is 0.69kV before the transformer improves it to the middle voltage level inside the offshore wind farm but after the wind power is transmitted through the HVDC system. In the PSCAD simulation, a PSCAD CIGRE benchmark three-phase full model is used as the HVDC offshore wind farm transmission system. This system configuration is shown in Figure 6.9. The CIGRE HVDC benchmark system is a mono-polar 500kV, 1000MW HVDC link with a 12-pulse converter on both the rectifier and inverter sides [93][94][95][96]. The AC side of the HVDC system consists of a filter and transformers. The filter is used to absorb the harmonics as well as to support the voltage at the converter. The DC side of the converter consists of a smoothing reactor. The HVDC submarine cable is simulated as a T-section. The resulting wind farm output power is shown in Figure 6.10, and the AC and DC side voltage and current results are shown in Figure 6.11.

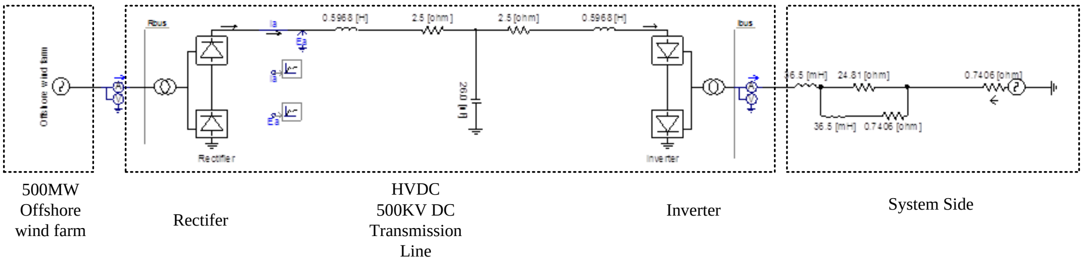

Figure 6.9 HVDC Transmission System

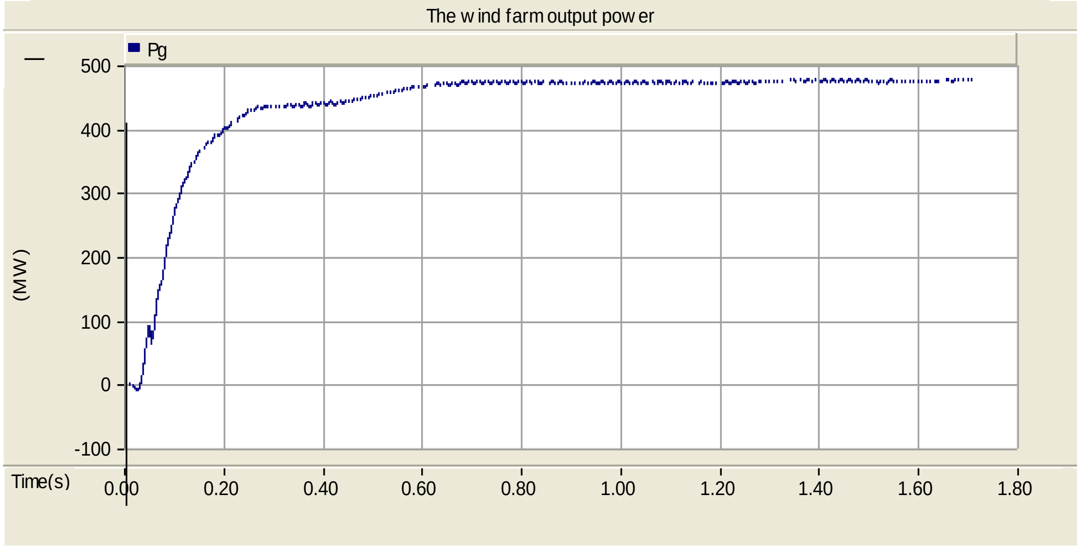

Figure 6.10 Output power of the offshore wind farm with an HVDC system

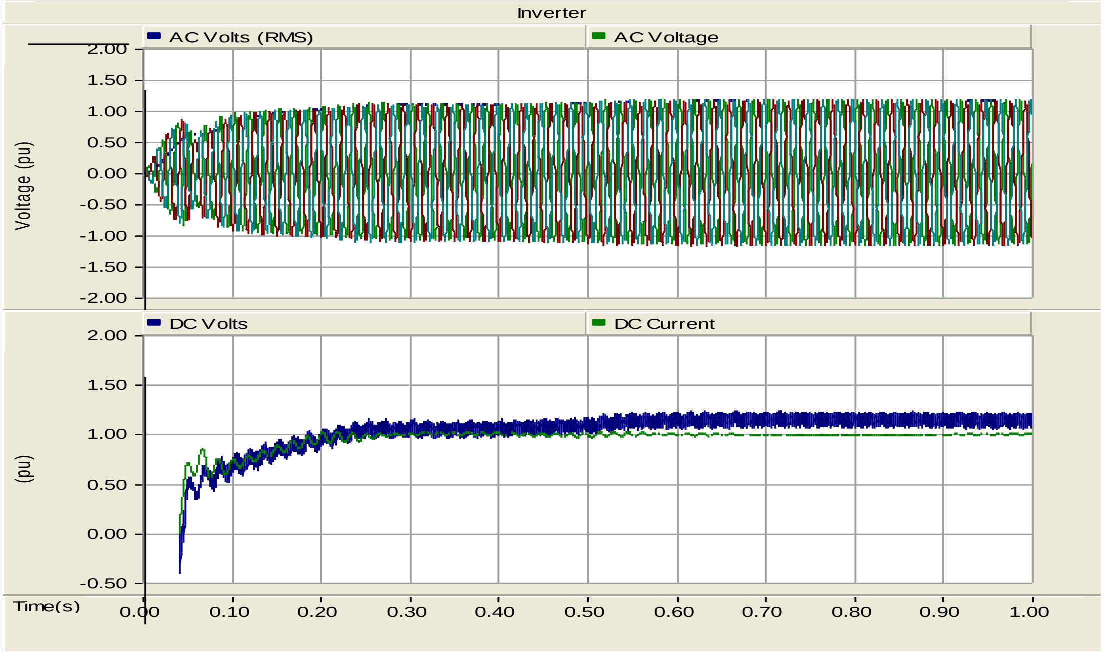

Figure 6.11 AC and DC of inverter in the HVDC transmission system

Since the DFIG cannot support its own voltage, a voltage support device at the rectifier side is required in the simulation. At the receiving end, a VSC, STATCOM or reactive compensator can be placed to support voltage.

6.4.2 HVAC Connection for Offshore Wind Farm

The 500MW offshore wind farm is connected to the South Carolina Thevenin equivalent transmission system through the HVAC transmission system. The offshore substation improves voltage from a 34.5kV to an 115kV transmission level [97][98][99]. Submarine cables deliver the wind energy onshore to an 115kV transmission system. The system configuration is shown in Figure 6.12.

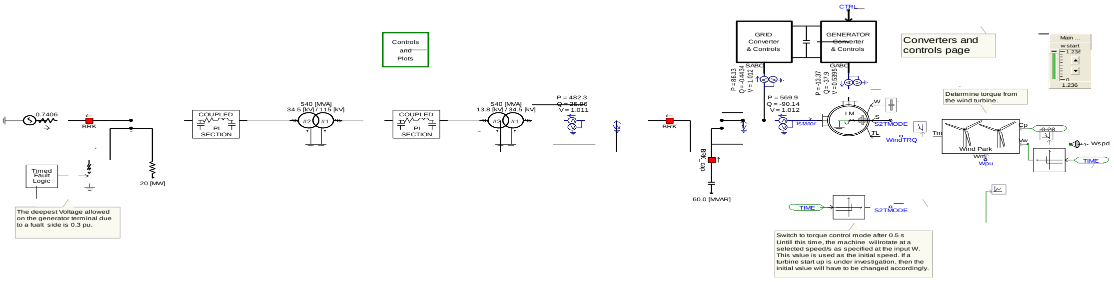

Figure 6.12 HVAC transmission system

Figure 6.13 illustrates the steady sate output power of the offshore wind farm. The DFIG changes from speed control to torque control at *t*=0.5sec.

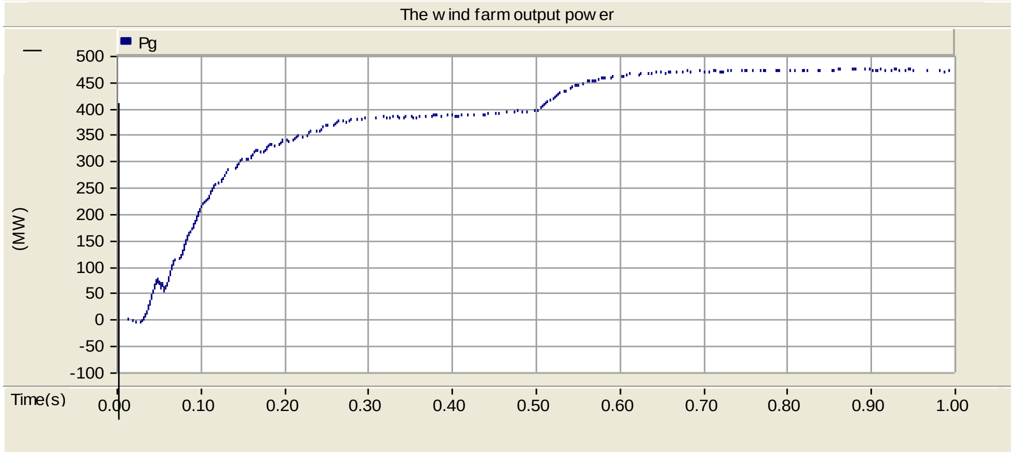

Figure 6.13 Output power of the offshore wind farm with the HVAC system

As Figure 6.14 shows, the output voltage reaches steady state when the 500MW of offshore wind energy is delivered to the onshore transmission system.

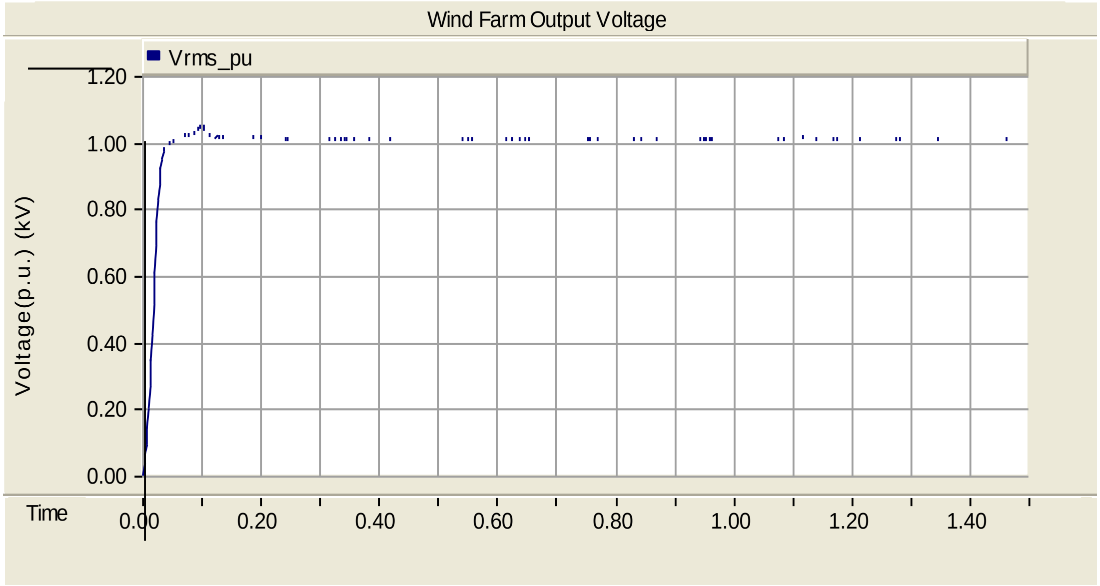

Figure 6.14 Output voltage of offshore wind farm with the HVAC system

6.5 Conclusions and Summary

Table 6.13 presents the conclusions reached based on the analysis presented here for the different configurations for offshore wind farm transmission systems [100][101].

1. The HVAC- based transmission system is a simple connection and a reliable transmission system. Its limitation is the high voltage submarine cable. The maximum available capacity of an HVAC cable is 220MW at I 32kV, 380MW at 220kV, or 800MW at 400kV. Thus, an offshore wind farm with 500MW capacity needs two l1SkV three-phase submarine cables, a substantial expense for an offshore wind project. In addition, because of the cables used in the system, the loss increases dramatically

compared with the HVDC configuration. A reactive compensator with at least six HCAV cables is necessary for this transmission system. Most offshore wind farm online today utilize the HVAC transmission scheme. Based on its properties, the HVAC transmission systems is more efficient for a small offshore wind farm a short distance from the coast.

2. The HVDC LCC-based transmission system is a mature technology for long-distance transmission of bulk energy inland. It can reach +/-500kV DC voltage during transmission. There's no practical offshore wind project implementing this technology for energy transmission on the ocean because this transmission system needs strong system connections to support the voltage on the AC side. In addition, the converter station for the LCC requires a large amount of space for filtering to avoid the harmonics produced by electronic devices. It also needs space for an offshore substation which is expensive to build.

3. The HVDC VSC-based transmission system is the ideal transmission system for a large scale offshore wind farm. There are 350 VSC converter stations installed in the world. But this field is still new as an offshore wind farm application and currently is in the testing stage. The DC voltage can reach up to +/-150kV, and it needs reactive power which can be provided by the VSC in the converter station. However, since this is a new technology, it is approximately 30-40% more expensive than LCC (IGBT is more expensive than thyristor valves, and the cable is more expensive than LCC).

Table 6.13 Summary of the difference configuration

	HVAC	HVDC VSC	HVDC LCC
Capacity	Capacity up to 600MW	Only test projects	Only Inland
kV Level	230kV	+/-135kV	+/-500kV
Substation	Yes	No but announced	Yes
Sub Cost	Transformer Small	Transformer + Converter 30%-40%More expensive then LCC	Transformer + Converter +Lots Filter
Cable #	Two three phases	Two	Two
Reactive Compensator	SVC, FACTS	No	Auxiliary Resource for Black Start
Distance Limitation	Yes	No	No
Cable Loss	High	Low	Low
WF size	Small	Medium	Large
Online	Yes	No	No

The selection of the offshore wind farm transmission configuration has to be investigated in relation to the size and the distance of the windmill from the shore. Not only the economic aspects need to be taken into consideration but also the electrical performance has to be investigated in both the research and development stages.

APPENDICES

APPENDIX A

Table 4 Transformer Parameters for Phase II

Transformer	34.5/115KV	Transformer	34.5/115KV Wind farm transformer
Controlled side	No Tapped	Winding 1 Nominal KV	115
Tap position	159	Winding1 Ratio($p.u.$ KV)	1.0
Auto adjust	Yes	Winding 1 Angle	0
Winding I/O code	Turn ratio	Winding 2 Nominal KV	34.5
Impedance I/O code	$Z_{p.u.}$	Winding2 Ratio($p.u.$ KV)	1
Admittance I/O code	Y $p.u.$	$R_{\max}$	1.5
Specified R	0.00036	Rmind($p.u.$ KV or degree)	0.51
Specified X	0.0167	Vmax($p.u.$ or KV)	1.5
Rate A	316	Vmin($p.u.$ or KV)	0.51
Rate B	409	Load Drop	0
Rate C	420	Impedance	0
Magnetizing G	0	R(table corrected $p.u.$ or watt)	0
Magnetizing B	0	X(table corrected $p.u.$ or watt)	0

APPENDIX B

Table 5 Data for the GE 3.6 MW Wind Turbine

GE 3.6 Wind tubine	value
Qmax	1.74MVAR
Qmin	-1.74 MVAR
Rating capacity	4MW
Pmax	3.6MW
Pmin	0.5MW
Zr	0
Zx	0.302
Power factor	1.0
Rr	0.00607 p.u.
Rs	0.0054 p.u.
Lls	0.1 p.u.
Llr	0.11 p.u.
Lm	4.5 p.u.
Vs	0.69kV

APPENDIX C

Table 6 Transformers Specification

Transformer index	Wind turbine transformer (4.16/34.5 KV)	Wind farm transformer (34.5/115 KV)
Winding MVA	100	100
Winding 1 Nominal KV	34.5	115
Tap position	33	153
Specified R	0	0.0108
Specified X	0.05	0.3304
Rate A	10	50.4
Rate B	10	51.8
Rate C	10	52.2
Impedance	0.5	0

REFERENCES

[1] J.Lewis Blacksburn, “Protective Relaying principals and applications”, 3rd edition, CRC Press, December, 2006.

[2] Allen Greenwood, “Electrical Transient in power systems”, 2nd Edition Wiley-Interscience, 1991.

[3] The World Wind Energy Association, 2012Half Year Report, http://www.wwindea.org/webimages/Half-year_report_2012.pdf, 2012.

[4] Thomas Ackermann, “Wind Power in Power Systems”, 2nd Edition, Wiley, May 21, 2012.

[5] European Wind Energy Association, “Pure Power Wind Energy Scenarios Up to 2030”, http://www.ewea.org/fileadmin/ewea_documents/documents/publications/reports/purepower.pdf, March 2008.

[6] Siegfried Heier and Rachel Waddington, “Grid Integration of Wind Energy Conversion Systems”, 2nd Edition, Wiley, June 5, 2006.

[7] European Wind Energy Association, “Wind in power 2012 European statistics”, http://www.ewea.org/fileadmin/files/library/publications/statistics/Wind_in_power_annual_statistics_2012.pdf, February 2013.

[8] A Joint resolution requiring recommendations from the wind energy production farms feasibility study committee, “South Carolina’s role in offshore wind energy development”, http://www.scsenate.gov/archives/EnergyOffice/WindEnergyProductionFarmsFeasibilityStudyCommitteeFin.pdf, 2008.

[9] CUPERA, “South Carolina Offshore Wind Farm Penetration Impact Report”, Clemson University.

[10] John J. Grangers, William Stevenson Jr., “Power system analysis”, 1st Edition, McGraw-Hill Science/Engineering/Math, January, 1994.

[11] J.Duncan Glover, Mulukutal S.Sarma, “Power System Analysis and Design”, 5th Edition, Cengage Learning, January, 2011.

[12] J.C. Das, “Transients in Electrical Systems Analysis, Recognition, and Mitigation”, 1st Edition, McGraw-Hill Professional, June 2010.

[13] G.T.Heydt, “Computer analysis Methods for Power System”, Macmillan Pub Co, December 1986.

[14] Paul C. Krause, Oleg Wasynczuk, Scott D. Sudhoff, “Analysis of Electric Machinery and Drive Systems”, 2nd Edition, Wiley-IEEE Press, March 2002.

[15] W. Qiao, R. G. Harley, “Grid Connection Requirements and Solutions for DFIG Wind Turbines”, 2008 IEEE Energy 2030 Conference, ENERGY 2008.

[16] Richard L.Burden, J.Douglas Faires, “Numerical analysis”, 9th Edition, Cengage Learning, August, 2010.

[17] EMTDC transient analysis for PSCAD power system simulation

[18] Ivan Arana Arista, “Modeling of switching transients in nested offshore wind farm and a comparison with measurements EMT simulations with Power Factory and PSCAD”, Master of Science Thesis, Electro Centre for Electric Technology (CET) Technical University of Denmark, June 2008

[19] A. Luna, F.K.D.A. Lima, D. Santos, P. Rodríguez, E. H. Watanabe, and S. Arnaltes, “Simplified modeling of a DFIG for transient studies in wind power applications”, IEEE Transactions on Industrial Electronics, Vol.58, No.1, pp.9-20, Jan. 2011.

[20] Abbey Daniel, Samson Geber, “Analysis of transients in wind parks: modeling of system components and experimental verification,” Master of Science Thesis, Chalmers University of, Goteborg, Sweden, 2008.

[21] W. Zhang, Z.N. Wei, G.Q. Sun, “Power flow calculation for power system including offshore wind farm”, International Conference on Sustainable Power Generation and Supply, Nanjing, 6-7 April 2009, pp.1-6.

[22] J.G. Slower, W.L. Kling, “Aggregated modeling of wind parks in power system dynamics simulations”. IEEE Bologna Power Tech Conference, 23-26 June 2003, Vol.3, pp.626–631.

[23] V. Akhmatov, H. Knudsen, “An aggregate model of a grid-connected, large-scale, offshore wind farm for power stability investigations-importance of windmill mechanical system”, Electrical Power and Energy System, Vol.24, 2002, pp.709-717.

[24] Y.B. Yang, X.M. Zha, “Aggregating wind farm with DFIG in power system online analysis,” IEEE 6th International Power Electronics and Motion Control Conference, Wuhan, 17-20 May 2009, pp.2233 – 2237.

[25] R. Pena, J. C. Clare, G. M. Asher, “Doubly fed induction generator using back-to-back PWM converters and its application to variable-speed wind-energy generation” IEE Proceedings Electric Power Applications, Vol.143, Issue 3, pp.529–551, May 1996

[26] A. Miller, E. Muljadi, D.S. Zinger, “A Variable Speed Wind Turbine Power Control”, IEEE Transactions on Energy Conversion, Vol.12, No.2, pp.181-186, Jun 1997.

[27] S. Li, T.A. Haskew, “Analysis of decoupled d-q vector control in DFIG back-to-back PWM Converter”, IEEE Power Engineering Society General Meeting, Tampa, FL, 24-28 June 2007, pp.1-7.

[28] M. Popat, B. Wu, F. Liu, N. Zargari, “Coordinated control of cascaded current-source converter based offshore wind farm”, IEEE Transactions on Sustainable Energy, Vol.3, No.3, pp.557-565, July 2012.

[29] L.M. Fernandez, C.A. Garcia, J.R. Saenz, F. Uredo, “Equivalent models of wind farms by using aggregated wind turbines and equivalent winds”, Energy Conversion and Management, Vol.50, Issue 3, pp.691–704, March 2009.

[30] H. Ergun, D.V. Hertem, R. Belmans, “Transmission System Topology Optimization for Large-Scale Offshore Wind Integration”, IEEE Transactions on Sustainable Energy, vol.3, no.4, pp.908-917, 2012.

[31] Kurt Thomsen, “Offshore Wind A comprehensive Guide to successful Offshore Wind Farm Installation”, 1st Edition, Elsevier, 2011.

[32] J. Yang, J. OReilly, J.E. Fletcher, “Redundancy anaysis of offshore wind farm collection and transmission systems”; International Conference on Sustainable Power Generation and Supply, Nanjing, April 6-7, 2009, pp.1-7.

[33] W.Y. Kang, C.Y. Lee, G.H. Shu, “Taiwan first large-scale offshore wind farm connection-a real project case study”, 2010 IEEE Industry Applications Society Annual Meeting (IAS), Houston, TX, 3-7 Oct. 2010, pp.1-9.

[34] W. Wiechowski, P.B. Eriksen, “Selected Studies on Offshore wind farm Cable connections-Challenges and experience of the Danish TSO”, 2008 IEEE Power and Energy Society General Meeting - Conversion and Delivery of Electrical Energy in the 21st Century, Pittsburgh, PA, 20-24 July 2008, pp.1-8.

[35] P. Sorensen, N.A. Cutululis, A. Vigueras-Rodriguez, L.E. Jensen, J. Hjerrild, M.H. Donovan, H. Madsen, “Power fluctuation from large wind farms”, IEEE Transactions on Power Systems, Vol. 22, No. 3, pp.958-965, Aug.2007.

[36] PSCAD, Manitoba research center “DFIG_2010_11.psc”, https://pscad.com/products/pscad/free_downloads, 2010

[37] P. Sorensen, A.D. Hansen, T. Sorensen, C.S. Nielsen, H.K. Nielsen, L. Christensen, M. ulletved, “Switching transients in wind farm grids”, 2007 European Wind Energy Conference and Exhibition, Milan, Italy, 2007.

[38] C.D. Tsirekis, G.J. Tsekouras, N.D. Hatziargyriou, B.C. Papadias, “Investigation of switching transient effects on power systems including wind farms”, Porto, 10-13 Sep. 2001.

[39] N. B. Negra, J. Todorovic and T. Ackermann, “Loss Evaluation of HVAC and HVDC Transmission Solutions for Large Offshore Wind Farms”, Electric Power Systems Research, Vol.76, No.11, pp.916-927, July 2006.

[40] H. Brakelmann, “Loss Determination for Long Three-Phase High-Voltage Submarine Cables”, European Transactions on Electrical Power, Vol.13, No.3, pp. 193-197, May/June 2003.

[41] US Department of Energy (DOE), US Bureau of Ocean Energy Management, Regulation, and Enforcement (BOEMRE), “A National Offshore Wind Strategy: Creating an Offshore Wind Energy Industry in the United States”, http://www.offshorewindhub.org/resource/518

[42] Predrag Djapic, Goran Strbac “Cost Benefit Methodology for Optimal Design of Offshore Transmission Systems”, http://webarchive.nationalarchives.gov.uk/+/http://www.berr.gov.uk/files/file47242.pdf.

[43] S.A. Herman, “Offshore Wind Farms: Analysis of Transport and Installation Costs”, Energy Research Centre of the Netherlands, 2002.

[44] James F. Manwell, Jon G. McGowan and Anthony L. Rogers, “Wind Energy Explained: Theory, Design and Application”, 2nd Edition, Wiley, February 1, 2010.

[45] Y. Feng, P.J. Tavner, H. Long, and J.W. Bialek, “Review of Early Operation of UK round 1 offshore wind farms”, 2010 IEEE Power and Energy Society General Meeting, July 25-29, 2010, pp.1-8.

[46] IEEE Guide to the Factors to Be Considered in the Planning, Design, and Installation of Submarine Power and Communications Cables

[47] Y.K. Wu, C.Y. Lee, G.H. Shu, “Taiwan’s First Large-Scale Offshore Wind Farm, Connection—A Real Project Case Study With a Comparison of Wind Turbine”, IEEE Transactions on Industry Applications, vol.47, no.3, pp. 1461 – 1469, 2011.

[48] B.C. Ummels, M. Gibescu, E. Pelgrum, W.L. Kling, and A.J. Brand“Impacts of Wind Power on Thermal Generation Unit Commitment and Dispatch”, IEEE Transactions on Energy Conversion, vol.22, no.1, pp. 44-51, 2007.

[49] Y. Tohbai, G.H. Wu, H. Guo, “A basic study on construction and control of offshore wind power generation system”, Transmission & Distribution Conference & Exposition: Asia and Pacific, Seoul, 26-30 Oct. 2009, pp.1-4.

[50] J. Glasdam, C.L. Bak, J. Hjerrild, “Transient studies in large offshore wind farms employing detailed circuit breaker representation”, Electrical Power and Energy System, Vol.5, No.7, pp.2214-2231, 2012.

[51] Ion Bolder, “Variable speed generator”, CRC Press, 2005.

[52] Arieh L.shenkman, “Transient Analysis of Electric Power Circuit Handbook”, Springer, Sep. 2005.

[53] F. Shewarega, I. Erlich, J.L. Rueda, “Impact of Large offshore wind farm on power system transient stability”, IEEE/PES Power Systems Conference and Exposition, Seattle, WA, 15-18 March 2009, pp.1-8.

[54] L. Liljestrand, A. Sannino, H. Breder, S. Thorburn, “Transients in collection grid of large offshore wind parks”, Wind Energy, Vol.11, 2008, pp.45-61.

[55] C.D. Tsirekis, G.J. Tsekouras, N.D. Hatziargyriou, B.C. Papadias, “Investigation of switching transient effects on power systems including wind farms”, 2001 IEEE Power Tech Proceedings, Porto, 10-13 Sep. 2001.

[56] A. Abbaszadeh, S. Lesan, V. Mortezapour, “Transient response of doubly fed induction generator under voltage sag using an accurate model”, 2009 IEEE PES/IAS Conference on Sustainable Alternative Energy, Valencia, 28-30 Sep. 2009, pp.1-6.

[57] C. Han, D.E. Martin, M.R. Lezama, “Transient over-voltage(TOV) and its suppression for a large wind farm utility interconnection”, International Conference on Sustainable Power Generation and Supply, Nanjing, 6-7 April 2009, pp.1-7.

[58] Y. Zhang, D. Xie, Z. Xiang, “Research on the switching transient and disconnecting transients of shunt capacitors in grid connected wind farms”, Third International Conference on Electric Utility Deregulation and Restructuring and Power Technologies, Nanjing, 6-9 April 2008, pp.2459-2464.

[59] I.J. Balaguer, Q. Lei, S. Yang, U. Supatti, and F. Peng, “Control for Grid-Connected and Intentional Islanding Operations of Distributed Power Generation” IEEE Transactions on Industrial electronics, vol.58, No.1, pp.147-157, January 2011

[60] H.M. Dola, B.H. Chowdhury, “Intentional islanding and adaptive load shedding to avoid cascading outages”, IEEE Power Engineering Society General Meeting, 2006.

[61] Z. Miao, “Impedance Model Based SSR Analysis for Type 3 Wind Generator and series-compensated Network”, IEEE Transactions on Energy Conversion, Vol.27, No.4, pp.984-991, Dec. 2012.

[62] C. Zhu, L. Fan, M. Hu, “Modeling and simulation of a DFIG-based wind turbine for SSR”, 2009 North American Power Symposium (NAPS), Starkville, MS, USA, 4-6 Oct. 2009, pp.1-6.

[63] L. Fan, R. Kavasseri, Z.L. Miao; C. Zhu, “Modeling of DFIG-based wind farm for SSR analysis”, IEEE Transactions on Power Delivery, Vol.25, No.4, pp.2073-2082, Oct. 2010.

[64] J. Martinez, P.C. Kjer, R. Teodorescu, “DFIG Turbine Representation for Small signal voltage control studies”, 12th International Conference on Optimization of Electrical and Electronic Equipment (OPTIM), Basov, 20-22 May 2010, pp.31-40.

[65] R. Pena, J.C. Clare, G.M. Asher, “Doubly Fed induction generator using back to back PWM converters and its application to variable speed wind energy generation”, IEE Proceedings Electric Power Applications, Vol.143, No.3, pp.231-241, May 1996.

[66] W. Shi, Q. Jiang, M. Hu, G. Tang, P. Jiang, “Mathematical model and main circuit design of three-phase voltage-source PWM rectifier”, Journal of Southeast University (Natural Science Edition), Vol. 32, No.1, pp.50-55, 2002.

[67] R. Pena-Alzola, M. Liserre, F. Blaabjerg, R. Sebastian, J. Dannehl, F. Fuchs, “Systematic Design of the Lead Lag Network Method for Active Damping in LCL-Filter Based Three Phase Converters”, IEEE Transactions on Industrial Informatics, No.99, pp.1-9, 2013.

[68] O. Wasynczuk, S.D. Sudhoff, T.D. Tran, D.H. Clayton, H.J. Hegner, “A voltage control strategy for current-regulated PWM inverters”, IEEE Transactions on Power Electronics, Vol.11, No.1, pp.7-15, Jan. 1996.

[69] J. Dannehl, F.W. Fuchs, S. Hansen, P.B. Thogersen, “Investigation of active damping approaches for PI-based current control of grid-connected pulse width modulation converters with LCL filters”, IEEE Transactions on Industry Applications, Vol.46, No.4, pp.1509-1517, July-Aug. 2010.

[70] Kurt Thomsen, “Offshore Wind: A Comprehensive Guide to Successful Offshore Wind Farm Installation”, 1st Edition, Elsevier, November, 2011.

[71] Offshore Wind Asessment For Norway, Final Report, 24th March 2010, Douglas Westwood, http://www.nve.no/Global/Energi/Havvind/Vedlegg/Annet/Offshore%20Wind%20Asessment%20For%20Norway%20-%20Final%20Report%20-%20190510%20with%20dc.pdf.

[72] Predrag Djapic and Goran Strbac, “Cost Benefit Methodology for Optimal Design of Offshore Transmission Systems”, http://webarchive.nationalarchives.gov.uk/+/http://www.berr.gov.uk/files/file47242.pdf.

[73] Mark J. Kaiser, Brian F. Snyder, “Offshore Wind Energy Cost Modeling Installation and Decommissioning”, Springer, January 2012.

[74] Paul A. Lynn, “Onshore and Offshore Wind Energy: An Introduction”, 1st Edition, Wiley, December 2011.

[75] Renewable Energy Technologies: COST ANALYSIS SERIES June 2012 Wind Power Issue 5/5 International Renewable Energy Agency IRENA IRENA woRkINg pApER Volume 1: Power Sector

[76] Lazaros P. Lazaridis, “Economic Comparison of HVAC and HVDC Solutions for Large Offshore Wind Farms under Special Consideration of Reliability”, Master’s Thesis, Royal Institute of Technology, Stockholm, 2005.

[77] C. Chou, Y. Wu, G. Han, C. Lee, “Comparative Evaluation of the HVDC and HVAC Links Integrated in a Large Offshore Wind Farm—An Actual Case Study in Taiwan”, IEEE Transactions on Industry Applications, Vol.48, No.5, pp.1639-1648, Sep./Oct. 2012.

[78] European Wind Energy Association, “Deep Water — the next step for offshore wind energy”, http://www.ewea.org/fileadmin/files/library/publications/reports/Deep_Water.pdf, July 2013

[79] Mathew Sathyajith, “Wind Energy: Fundamentals, Resource Analysis and Economics”, HAR/CDR Edition, Springer, January 13, 2006.

[80] Ervin Spahic and Gerd Balzer, “Power fluctuation from a large wind farm”, http://ieeexplore.ieee.org/stamp/stamp.jsp?arnumber=01600551, 2005.

[81] J. Robinson, D. Jovcic, G. Joos, “Analysis and design of an offshore wind farm using a MV DC grid”, IEEE Transactions on Power Delivery, Vol.25, No.4, pp.2164-2173, Oct.2010.

[82] V. Akhmatov, A.H. Nielsen, “A small test model of the transmission grid with a large offshore wind farm for education and research at technical university of Denmark”, IEEE PES Power Systems Conference and Exposition, Atlanta, GA, Oct. 29, 2006, pp. 650-654.

[83] Y.C. Miao, “The impact of large scale offshore wind farm on the power system”, China International Conference on Electricity Distribution (CICED), Nanjing, 13-16 Sep. 2010, pp.1-5.

[84] P. Bresesti, W.L. Kling, R. Vailati, “Transmission expansion issues for offshore wind farm integration in Europe”, IEEE/PES Transmission and Distribution Conference and Exposition, Chicago, IL, April 21-24, 2008, pp.1-7.

[85] P.D. Hopewell, F. Castro-Sayas, D.I. Bailey, “Optimizing the design of offshore wind farm collection networks”, Proceedings of the 41st International Universities Power Engineering Conference, Newcastle upon Tyne, Sep. 6-8, 2006, pp.84-88.

[86] M. Nandigam, S.K. Dhali, “Optimal Design of an offshore wind farm layout”, International Symposium on Power Electronics, Electrical Drives, Automation and Motion, Ischia, June 11-13, 2008, pp.1470-1474.

[87] M. Dicorato, G. Forte, P. Pugliese, M. Trovato, F. Pallotti, “Critical Issues in large offshore wind farm design and operation”, 2009 International Conference on Clean Electrical Power, Capri, June 9-11, 2009, pp.471-478.

[88] W.J. Wilson, M.M. Morcos, “Design of an offshore wind farm on Lake Michigan: part 1”, 38th North American Power Symposium, Carbondale, IL, Sep. 17-19, 2006, pp.597-602.

[89] J. Glasdam, C.L. Bak, J. Hjerrild, “Transient studies in large offshore wind farms employing detailed circuit breaker representation”, Electrical Power and Energy System, Vol.5, No.7, pp.2214-2231, 2012.

[90] M. Johan, de Haan S.W.H, “Short-Circuit Current of Wind Turbines With Doubly Fed Induction Generator”, IEEE Transactions on Energy Conversion, Vol.22, No.1, pp.174-180, March 2007.

[91] A.S. Morched, V. Brandwajn, “Transmission network equivalent for electromagnetic transients studies”, IEEE Transactions on Power Apparatus and Systems, Vol. PAS-102, No.9, pp.2984-2994, Sep. 1983.

[92] H.T. Jadhav, R. Roy, “A Critical Review on the Grid Integration Issues of DFIG based Wind Farms”, 10th International Conference on Environment and Electrical Engineering (EEEIC), Rome, 8-11 May 2011, pp.1-4.

[93] Mukund R. Patel, “Wind and Solar Power Systems Design, Analysis and Operation”, 2nd Edition, CRC Press, July, 2005.

[94] Mark. J. Kaiser and Brian.F.Snyder, “Offshore Wind Energy Cost Modeling, Installation and decommissioning”, Springer, January 2012.

[95] Walter Musial, Bonnie Ram, “Large-Scale Offshore Wind Power in the United States-EXECUTIVE SUMMARY” National Renewable Energy Lab, pp. 1, Sep. 2010.

[96] Walter Musial, Bonnie Ram, “Large-Scale Offshore Wind Power in the United States-ASSESSMENT OF OPPORTUNITIES AND BARRIERS” National Renewable Energy Lab, http://www.nrel.gov/docs/fy10osti/49229.pdf, Sep. 2010.

[97] Global Wind Energy Council, “Global wind statistics 2012”, http://www.gwec.net/wp-content/uploads/2013/02/GWEC-PRstats-2012_english.pdf.

[98] European Wind Energy Association, “Deep Water — the next step for offshore wind energy”, http://www.ewea.org/fileadmin/files/library/publications/reports/Deep_Water.pdf, July 2013

[99] Renewables Advisory Board, “Value Breakdown for the offshore wind sector”, https://www.gov.uk/government/uploads/system/uploads/attachment_data/file/48171/2806-value-breakdown-offshore-wind-sector.pdf, February 2010.

[100] The European offshore wind industry-key trends and statistics 1st half 2013, http://www.ewea.org/fileadmin/files/library/publications/statistics/EWEA_OffshoreStats_July2013.pdf.

[101] Offshore wind farm layout optimization A Dissertation Presented by CHRISTOPHER NEIL ELKINTON Submitted to the Graduate School of the University of Massachusetts Amherst in partial fulfillment of the requirements for the degree of DOCTOR OF PHILOSOPHY September 2007 Mechanical and Industrial Engineering.